Universität Hamburg
DER FORSCHUNG | DER LEHRE | DER BILDUNG

The Ocean Submesoscale: Kinetic Energy Conversion and Adjoint Modelling

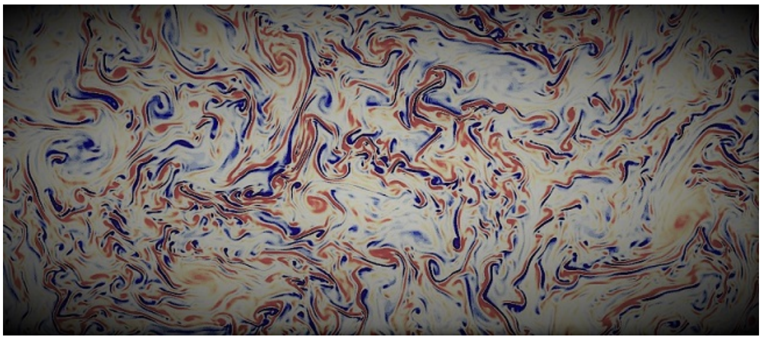

Dissertation
with the aim of achieving a doctoral degree
at the Faculty of Mathematics, Informatics and Natural Sciences
Department of Earth Sciences
at Universität Hamburg

submitted by

Song Li

from Hubei, China

Hamburg

2021

Department of Earth Sciences

Date of Oral Defense: 24 September, 2021

Reviewers: Prof. Dr. Detlef Stammer
Dr. Nuno Serra

Members of the examination commission: Chair Prof. Dr. Detlef Stammer
Depute chair PD Dr. Thomas Pohlmann
Prof. Dr. Eva-Maria Pfeiffer
Dr. Nuno Serra
Dr. Sergiy Vasylkevych

Chair of the Subject Doctoral Committee
Earth System Sciences: Prof. Dr. Dirk Gajewski

Dean of Faculty MIN: Prof. Dr. Heinrich Graener

Abstract

Ocean submesoscale processes have spatial scales of $\mathcal{O}(0.1) - \mathcal{O}(10)$ km in the horizontal, 0.01 to 1 km in the vertical, and temporal scales of hours to days. They are ubiquitous in the global ocean and take the form of fronts, filaments, waves, and coherent vortices, both at the surface and throughout the ocean interior. The ocean submesoscale is created by instabilities due to mesoscale strain fields and strong currents. It serves as a tunnel to extract energy from the larger geostrophic flows and transfer it to dissipation scales. Recent research points out that the ocean submesoscale could directly influence the ocean energy balance or indirectly achieve that through the mesoscale. However, due to the lack of high-resolution observations, it is impossible to resolve the submesoscale in a large enough region to enable meaningful energy balance calculations. Therefore, high-resolution simulations are the only way to study the impact of the ocean submesoscale on the ocean energy balance. In the first part of this thesis, I use a high-resolution (500 m) idealized numerical model to investigate the impact of the ocean submesoscale on kinetic energy conversion. In the second part, I try to constrain the ocean submesoscale in an adjoint-based data assimilation model by using ocean surface information.

Specifically, in the first part of my work, I use the output from an idealized 500-m resolution ocean numerical simulation to study the conversion of kinetic energy in the absence and presence of wind stress forcing. In contrast to the results of the unforced run, kinetic energy increased approximately nine times in the mixed layer and considerably in the pycnocline in the forced run. Eddies and filaments were seen to re-stratify the mixed layer, and wind-induced turbulence at the base of the mixed layer promoted its deepening and therefore dramatically enhanced the exchange between eddy kinetic energy (K_e) and eddy potential energy (P_e). The wind-stress forcing additionally affected the conversion processes between K_e and mean kinetic energy (K_m). The imposed rotating wind also excited inertial and superinertial motions throughout almost the whole water column. Although those motions dominated the transient conversion between P_e and K_e and between K_e and K_m, the time-integrated effect was almost null. In addition, I found an asymmetric character in kinetic energy conversion by eddies. Cyclonic and anticyclonic eddies showed different abilities to contain K_e and P_e and distinct efficiency to convert K_e. The external wind forcing also altered such asymmetry and led to an opposite behaviour regarding the conversion between K_e and P_e, as well as K_e and K_m by cyclonic and anticyclonic eddies.

In the second part of my work, I use an eddy-resolving (500 m) adjoint-based data assimilation model and implement a set of experiments to investigate the possibility of constraining the submesoscale flow (1$\sim$10 km) in the ocean. This study indicates that assimilating sea surface height (SSH) alone allows recovering the three-dimensional submesoscale flow and temperature fields until the base of the mixed layer. However, the submesoscale salinity field can only be retrieved if sea surface salinity (SSS) is additionally assimilated. The predictability of the submesoscale flow was found to be as short as 3∼4 days in my experiments due to the highly non-linear nature of the submesoscale. The success in constraining the ocean submesoscale profoundly relies on the observations' spatial resolution and error level. An extremely large temporal resolution in the observations is, however, not necessary, as some information between each observation may be redundant. Lastly, the sampling requirements of observations were found to increase with increasing submesoscale activity.

The present study advances the knowledge on the impact of the ocean submesoscale on the kinetic energy conversion and highlights the different behaviours cyclonic and anticyclonic eddies and filaments have during the energy conversion. Furthermore, this study proposes that it is necessary to provide spatially high-resolution and accurate observations at the submesoscale when trying to constrain the ocean submesoscale. Although all results are based on highly idealized simulations, they are important steps contributing to understanding the real global ocean submesoscale, in particular using a complex data assimilation system.

Zusammenfassung

Submesoskalige Prozesse im Ozean haben eine räumliche Ausdehnung von $\mathcal{O}(0,1) - \mathcal{O}(10)$ km in der Horizontalen, 0,01 bis 1 km in der Vertikalen und eine zeitliche Ausdehnung von Stunden bis Tagen. Sie sind im globalen Ozean allgegenwärtig und treten in Form von Fronten, Filamenten, Wellen und kohärenten Wirbeln auf, sowohl an der Oberfläche als auch im Inneren des Ozeans. Die Submesoskala des Ozeans entsteht durch Instabilitäten, die auf mesoskalige Spannungsfelder und starke Strömungen zurückzuführen sind, und dient als Tunnel, um Energie aus den größeren geostrophischen Strömungen zu extrahieren und sie auf die Dissipationsskalen zu übertragen. Neuere Forschungen weisen darauf hin, dass die Submesoskala des Ozeans die Energiebilanz des Ozeans direkt oder indirekt über die Mesoskala beeinflussen könnte. Aufgrund des Mangels an hochauflösenden Beobachtungen ist es jedoch unmöglich, die Submesoskala in einer ausreichend großen Region aufzulösen, die eine aussagekräftige Energiebilanzberechnungen ermöglichen würde. Daher sind hochauflösende Simulationen die einzige Möglichkeit, die Auswirkungen der Submesoskala auf die Energiebilanz des Ozeans zu untersuchen. Im ersten Teil dieser Arbeit verwende ich ein hochauflösendes (500 m) idealisiertes numerisches Modell, um die Auswirkungen der Submesoskala des Ozeans auf die kinetische Energieumwandlung zu untersuchen. Im zweiten Teil versuche ich, die Submesoskala des Ozeans in einem adjungiert-basierten Datenassimilationsmodell durch die Verwendung von Informationen über die Ozeanoberfläche einzugrenzen.

Im ersten Teil meiner Arbeit verwende ich die Ergebnisse einer idealisierten numerischen Ozeansimulation mit einer Auflösung von 500 m, um die Umwandlung der kinetischen Energie in Abwesenheit und Anwesenheit von Windschubspannung zu untersuchen. Im Gegensatz zu den Ergebnissen ohne Antrieb durch Windschubspannung stieg die kinetische Energie in der oberen gut durchmischten Schicht etwa um das Neunfache und in der Pyknokline im mit Windschubspannung angetriebenen Lauf erheblich an. Es zeigte sich, dass Wirbel und Filamente die Mischschicht umschichten, und die windinduzierte Turbulenz an der an der Untergrenze der Mischschicht förderte ihre Vertiefung und damit den Austausch zwischen kinetischer Wirbelenergie (K_e) und potenzieller Wirbelenergie (P_e) drastisch. Der Windstressantrieb beeinflusste zusätzlich die Umwandlungsprozesse zwischen K_e und der mittleren kinetischen Energie (K_m). Der auferlegte rotierende Wind regte auch inertiale und superinertiale Bewegungen in fast der gesamten Wassersäule an. Obwohl diese Bewegungen die transiente Umwandlung zwischen P_e und K_e sowie zwischen K_e und K_m dominierten, war der zeitintegrierte Effekt fast null. Darüber hinaus fand ich asymmetrische Eigenschaften in der Umwandlung kinetischer Energie durch Wirbel. Zyklonale und antizyklonale Wirbel zeigten unterschiedliche Fähigkeiten zur Aufnahme von K_e und P_e und eine unterschiedliche Effizienz bei der Umwandlung von K_e. Der äußere Windantrieb veränderte diese Asymmetrie ebenfalls und führte zu einem entgegengesetzten Verhalten bei der Umwandlung zwischen K_e und P_e sowie K_e und K_m durch zyklonale und antizyklonale Wirbel.

Im zweiten Teil meiner Arbeit verwende ich ein wirbelauflösendes (500 m) adjungiert-basiertes Datenassimilationsmodell und führe eine Reihe von Experimenten durch, um die Möglichkeit zu untersuche, Randbedingungen für die submesoskalige Strömung im Ozean zu finden. Diese Studie zeigt, dass die Assimilierung der Meeresoberflächenhöhe (SSH) allein es ermöglicht, die dreidimensionalen submesoskaligen Strömungs- und Temperaturfelder bis zur Basis der gemischten Schicht wiederherzustellen. Das submesoskalige Salinitätsfeld kann jedoch nur ermittelt werden, wenn zusätzlich die Salinität der Meeresoberfläche (SSS) assimiliert wird. Es stellt sicher heraus, dass die Vorhersagbarkeit der submesoskaligen Strömung aufgrund der hochgradig nichtlinearen Natur der Submesoskala nur 3$\sim$4 Tage beträgt. Der Erfolg bei der Eingrenzung der submesoskaligen Ozeanströmung hängt in hohem Maße von der räumlichen Auflösung und dem Fehlerniveau der Beobachtungsdaten ab. Eine extrem hohe zeitliche Auflösung der Beobachtungen ist jedoch nicht erforderlich, da einige Informationen zwischen den einzelnen Beobachtungen überflüssig sein können. Abschließend wurde festgestellt, dass die Anforderung and die Erhebung der Bebobachtungen mit zunehmender submesoskaliger Aktivität steigen.

Die vorliegende Studie erweitert das Wissen über die Auswirkungen der Submesoskala des Ozeans auf die kinetische Energieumwandlung und verdeutlicht das unterschiedliche Verhalten von zyklonalen und antizyklonalen Wirbeln und Filamenten während der Energieumwandlung. Darüber hinaus zeigt diese Studie, dass es notwendig ist, räumlich hochaufgelöste und genaue Beobachtungsdaten auf der Submesoskala bereitzustellen, wenn man versucht, die Submesoskala des Ozeans einzuschränken. Obwohl alle Ergebnisse auf stark idealisierten Simulationen beruhen, sind sie wegbereitend für das Verständnis der realen Submesoskala des globalen Ozeans, insbesondere unter Verwendung eines komplexen Datenassimilationssystems.

Contents

Abstract **i**

Zusammenfassung **iii**

1 Introduction **1**

1.1 Motivation 1

1.2 State of the art 5

1.2.1 The ocean submesoscale 5

1.2.2 Ocean data assimilation 8

1.3 Study objectives 13

1.4 Thesis outline 13

2 Methodology **15**

2.1 The numerical ocean model and setup 15

2.1.1 The forward model 15

2.1.2 Model configuration and spin-up 15

2.1.3 Twin simulations with and without wind forcing 16

2.2 The adjoint model 19

3 Kinetic energy conversion in a wind-forced submesoscale flow **23**

3.1 Introduction 23

3.2 Description of the flow field 24

3.3 Kinetic energy reservoirs and conversion terms 26

3.3.1 Quantifying the Lorenz energy cycle 26

3.3.2 Conversion between p_e and k_e 29

3.3.3 Conversion between k_m and k_e 36

3.4 Asymmetry in kinetic energy conversion by eddies 40

3.4.1 Components separation 40

3.4.2 Eddies and filaments in the unforced run 41

3.4.3 Eddies and filaments in the wind-forced run 42

3.5 Summary and discussion 44

4 Constraining the submesoscale flow in an eddy-resolving adjoint-based data assimilation model 47
4.1 Adjoint model set-up 47
4.1.1 ”truth” state and ”observations” 48
4.1.2 ”First-guess” initial condition 48
4.1.3 Cost function and control variables 50
4.1.4 Error of first-guess and observations 51
4.2 Impact of the assimilation window length 52
4.3 Impact of assimilating additional surface observations 58
4.4 Impact of degrading the observational spatial resolution 61
4.5 Impact of degrading the observational temporal resolution 65
4.6 Impact of degrading the accuracy of observations 65
4.7 Impact of increased submesoscale activity 67
4.8 Summary and discussion 70

5 Conclusions and outlook 73
5.1 Impact of the ocean submesoscale on kinetic energy conversion 73
5.2 Sensitivity of constraining the submesoscale from observations 74
5.3 Outlook 75

Appendices vii
A.1 Formulation of the 4DVAR method vii
A.2 Formulation of the adjoint model ix
A.3 Derivation of the kinetic energy balance equation x

References xxii

Acronyms xxiii

List of Figures xxvii

List of Tables xxix

Acknowledgements xxxi

Chapter 1

Introduction

1.1 Motivation

Ocean submesoscale processes have spatial scales in the range $\mathcal{O}(0.1) - \mathcal{O}(10)$ km in the horizontal and 0.01 to 1 km in the vertical and temporal scales of hours to days. Figure 1.1 shows the approximate space-time distribution of oceanic scales, where the submesoscale processes can be compared to other oceanic processes. Submesoscale flow patterns are ubiquitous in the global ocean from the surface to the interior, taking the form of filaments, fronts, waves, and coherent vortices (McWilliams, 2016). They are the intermediate scales created by mesoscale strain fields and strong currents, serving as a tunnel to extract energy from the larger geostrophic flows and transferring it to small scales for dissipation.

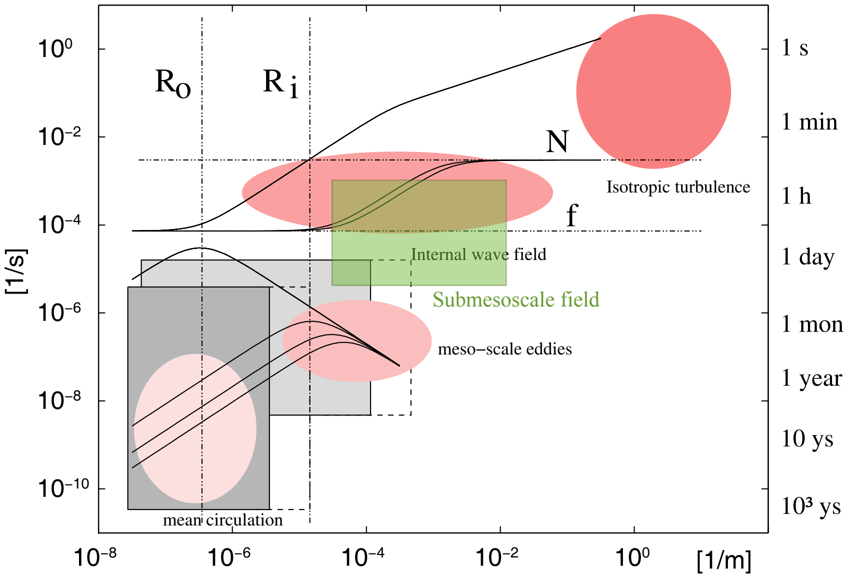

Figure 1.1: Space-time scales of important oceanic processes. The green area denotes approximately the submesoscale range. Adapted from Olbers et al. (2012, p. 333).

The ocean submesoscale plays a dominant role in the vertical heat and tracer transport in the upper ocean (Fu and Ferrari, 2008; Bachman et al., 2017). For example, Su et al. (2018) found that ocean submesoscales are critical components of the Earth's climate by transporting heat between the ocean interior and the atmosphere. Ocean submesoscales are found intensified in winter in the upper layer (e.g., Buckingham et al., 2016; Qiu et al., 2018; Zhang et al., 2021). Figure 1.2 shows a perfect agreement between submesoscale activity and submesoscale vertical heat transport, which is five times greater than mesoscale vertical heat transport in their experiments. The submesoscale vertical transport is impressively significant during wintertime in the upper 200 m in both hemispheres, implying a critical role that ocean submesoscales play in transporting heat from the interior to the surface. As climate change is regulated by heat, freshwater, and tracer transport in the ocean, ocean submesoscales partly account for the Earth's climate.

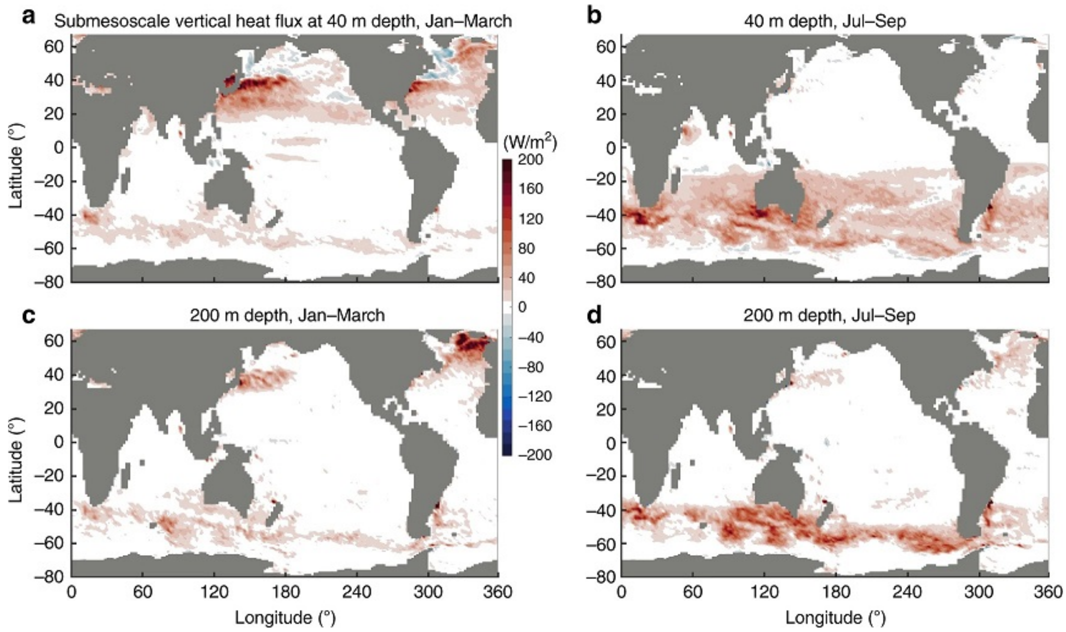

Figure 1.2: Global patterns of submesoscale vertical heat transport. Retrieved from Su et al. (2018).

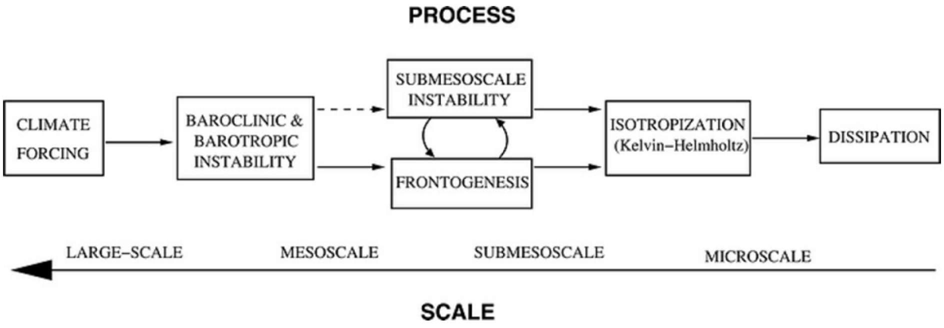

Figure 1.3: Schematic diagram of the important dynamical regimes sorted by scale. Retrieved from Capet et al. (2008b).

Ocean submesoscale processes also influence the ocean energy balance. This is realized in two ways: 1) through the interaction with mesoscale variability (e.g., Barkan et al., 2015; Capet et al., 2008a; Rocha et al., 2016a) and 2) acting as a pathway for dissipating energy (e.g., Bracco et al., 2019). Figure 1.3 shows, from the scale view, the centre position of the submesoscale in the energy transformation processes. The ocean submesoscale is connected with mesoscale motions by baroclinic and barotropic instabilities and impact the microscale motions by frontogenesis instabilities.

However, unlike the mesoscale motions, e.g., the mesoscale eddy field (with scales of about 100 km), which also partly accounts for the climate change (Zhang et al., 2014) but has been impressively investigated in the past three decades owing to the continuous global satellite altimetry measurements (e.g., Chelton et al., 2011), the submesoscale is still under-observed and under-investigated. There are several reasons why the submesoscale is under-observed. Resolving the ocean submesoscale requires high-resolution observations. Dropping corresponding equipment (e.g., Argo, XBT, .etc) is the mainstream method to measure the interior ocean. Nevertheless, the small size, fast movement and short life period of submesoscale motions are the main obstacles to their observation and thus, extensively dense observing devices are needed. Although it is technically and theoretically possible to track the submesoscale activity in the global ocean, the economic consideration makes it only possible for some specific events, e.g., the Deepwater Horizon spill incident (Poje et al., 2014). Therefore, observing the ocean submesoscale in large parts of the ocean could only rely on surface observations from satellites.

New technical problems arise for the satellite measurements to observe ocean submesoscales. For example, the signal contamination from high-frequency motions, as well as the measurement noise of existing altimeter missions, make it technically challenging to observe the ocean submesoscale with satellite altimetry (Fu and Ferrari, 2008; Chavanne and Klein, 2010). One of the current popular altimeter missions from AVISO provides gridded global sea surface height (SSH) with a resolution of 0.25°, which only makes it possible to resolve the mesoscale features. The good news is that despite the postponed launching of the new generation altimeter mission - Surface Water and Ocean Topography (SWOT), its new launching schedule will be at the end of 2022. The upcoming mission will be able to provide an unprecedented resolution for Earth's surface observations, namely 15 km-resolution for gridded SSH, therefore, offering scientists numerous opportunities to approach the study of submesoscale variability (Rocha et al., 2016b; Qiu et al., 2018; Zhang and Qiu, 2018). However, such improved resolution is still far from resolving ocean scales smaller than 30 km.

The status of the under-observed ocean submesoscale, therefore, determines their investigation mainly relying on numerical simulations. Due to the fast developments of supercomputers in recent years, there is increasing interest in exploring the ocean submesoscale with model simulations (e.g. Roullet et al., 2012; McWilliams, 2008; Molemaker et al., 2010; Callies and Ferrari, 2013; Gula et al., 2016). However, the statistics of the submesoscale are still absent in a global sense because of the enormous computational challenge.

From the above limitations from observations and simulations, the ocean submesoscale is still highly under-investigated. Plenty of questions remain unclear regarding the submesoscale (McWilliams, 2016). For example, as the submesoscale regime is largely overlapped with inertial gravity waves (see Figure 1.1), it is challenging to separate submesoscale from inertial gravity wave activity. Another important question regards the ocean energy balance. There is already a systematic study addressing the global ocean energy balance by diagnosing the Lorenz energy cycle (LEC) (von Storch et al., 2012). But their simulations are too coarse to resolve the submesoscale. Thus, a quantified description of the ocean submesoscale's role in the ocean energy balance remains to be performed. The work in the first part of the present thesis is therefore motivated by this absence.

The first work is to investigate the impact of the submesoscale on the energy balance, more specifically, on the kinetic energy conversion. Twin idealized simulations are used with very high resolution ($\sim$ 500 m), one with the wind forcing and the other without, wherein the former much more abundant submesoscales develop. The comparison between the two runs will show the influence of additional submesoscale activity on the ocean kinetic energy conversion. Moreover, by comparing different behaviours of kinetic energy conversion, the different abilities of cyclonic and anticyclonic eddies and filaments will be revealed.

Nevertheless, there is probably some distance between the results of the above-idealized simulations and the situation in the real ocean. Simulation results need, in the end, to be verified by observations. Our ultimate goal is to test results in the real ocean by using ocean observations. Although it will be impossible to obtain observations that can fully resolve scales of 500 m in the following two or three decades (personal estimation, hopefully wrong), it is still fascinating to explore which factors determine the inference of submesoscale processes in the real ocean. Our premise is that observations resolving the submesoscale (0.1$\sim$10 km) in vast ocean areas will only be possible at the surface and from satellites. But it remains challenging for the satellites to obtain very high-resolution observations due to technical reasons. Could we thus have a solution that would compromise the requirements of observation resolution and still resolve the ocean submesoscale?

The basic idea is that data assimilation could help. Data assimilation is the general procedure of combining the information from a numerical model and observations to estimate the true state of the ocean. In general, observations with 10 km resolution can only spatially resolve phenomena with scales larger than 20 km. However, when combining the 10 km resolution observations with a high-resolution (order of hundreds of meters) numerical model, we could, in principle, directly constrain the phenomena with scales larger than 10 km and infer the scales smaller than 10 km, which are supported by the resolved dynamics. In other words, with the help of data assimilation, we may lose the observation requirements to constrain the submesoscale.

Motivated by this thought, the work in the second part of my dissertation is to test this hypothesis and primarily to find out the sensitivity of an assimilation procedure, meaning the skill of the data assimilation model to accurately simulate the ”correct” submesoscale motions, to the spatial/temporal resolution and the accuracy of the ocean observations. In a twin experiment framework, SSH and/or sea surface temperature (SST) and/or sea surface salinity (SSS) will be first assimilated to investigate to what extent the surface information is enough to constrain the three-dimensional (3D) submesoscale field. In a second step, I will explore the assimilation sensitivity to spatial and temporal resolution and noise level of the observations.

1.2 State of the art

1.2.1 The ocean submesoscale

Due to the small size, fast movement, and short life cycle of the submesoscale, current observational systems are inadequate to represent complete three-dimensional submesoscale structures. At present, high-resolution models are therefore the only way to provide the richest realizations and the most feasible route for understanding submesoscale dynamics (McWilliams, 2016; Dauhajre et al., 2017). There is an increasing awareness that ocean submesoscales are critical to understand the physical ocean. Also, the development of supercomputers makes it possible to implement very high-resolution simulations (0.5∼2 km) of the regional ocean. Hence plenty of studies have paid attention to the ocean submesoscale in recent years.

Recalling from Figure 1.1 that the submesoscale and internal wave fields are highly overlapped, it is challenging to distinguish submesoscales from internal wave (McWilliams, 2016, 2019). Zhang et al. (2021) noted that to understand the surface submesoscale above ∼50 m or associated superinertial and even smaller-scale currents, very high-resolution observations are needed. There are also some studies addressing the interaction of superinertial waves and the submesoscale (e.g., Whitt et al., 2018; Boas et al., 2020). The superinertial motions may dominate the kinetic energy in the regions away from the surface forcing (Niwa and Hibiya, 1997; Meroni et al., 2017). This reminds us of considering the separation between the submesoscale and internal waves when the focus is only on submesoscales.

The generation and destruction of submesoscale structures are found to be associated with instabilities and boundary effects (Molemaker et al., 2015; Callies et al., 2016). Specifically, McWilliams (2016) concluded that the generation mechanisms of submesoscale currents are a) mixed layer instability, b) strain-induced frontogenesis, c) turbulent thermal wind, and d) topographic wakes (Srinivasan et al., 2019). On the other hand, Zatsepin et al. (2019) concluded that the formation mechanisms of submesoscale eddies are a) horizontal velocity shear instability, b) interaction of currents with topographic inhomogeneities and obstacles, c) baroclinic instability and frontogenesis. For the destruction, McWilliams and Molemaker (2011) demonstrated an essentially inviscid, baroclinic, dynamical process for frontogenetic arrest through frontal instability.

Most submesoscale work is undertaken using numerical simulations, and the resolution of the numerical model affects the richness of the submesoscale variations in those simulations. In general, within the effective range of the numerical model, higher-resolution simulations usually permit more abundant submesoscale activity (Couvelard et al., 2015; Jensen et al., 2018). Nevertheless, the resolution is not essentially responsible for submesoscales. Submesoscales happen around two primary places, one in the near-surface layer and another in topographic wakes (McWilliams, 2019). Zhang et al. (2021) explored the submesoscale dynamics by long-term high-resolution mooring arrays in the northwestern Pacific subtropical countercurrent region during 2017-2019. They pointed out that the submesoscale is generated mainly through a combination of baroclinic instability in the upper mixed and transitional layers.

The interplay between submesoscale and mesoscale variability was also recently widely investigated. For example, Rocha et al. (2016a) studied mesoscale and submesoscale wavenumber spectra in the Drake Passage. Capet et al. (2008a,b) investigated the mesoscale-to-submesoscale transition in the California Current System. Gula et al. (2016) proposed a mechanism by which energy is transferred from the mesoscale geostrophic flow to the submesoscale via vertical vorticity generation in the bottom boundary layer. More recently, Schubert et al. (2019) studied the submesoscale impact on mesoscale Agulhas dynamics. They showed that the representation of mesoscale eddies in the Agulhas ring path improves with increasing resolution of submesoscale flows, which implies the direct interaction between submesoscales and mesoscale eddies. In addition, Bracco et al. (2019) illustrated how meso- and submesoscale circulations impact (from a perspective of mesoscale-submesoscale interactions) the dispersion of biologically and climatically relevant tracers in the Gulf of Mexico. These studies suggest that submesoscale processes can directly influence the ocean energy balance through interactions with mesoscale phenomena.

Indeed, there is an increasing awareness that submesoscale processes are important for energy conversion and dissipation, particularly in the upper ocean. Frontogenesis is a highly efficient means of transferring kinetic and available potential energy to smaller scales through the contraction of the frontal width and depth (McWilliams and Molemaker, 2011). The restratification is usually associated with the conversion between potential and kinetic energy in the mixed layer. Lapeyre et al. (2006) implemented a twin simulation with and without surface frontogenesis in a baroclinic balanced jet and found that small-scale surface fronts have a considerable impact on the restratification process. Mensa et al. (2013) investigated the seasonality of the submesoscale dynamics in the Gulf Stream region and found a deepened mixed layer in winter, which is related to the vigorous winter submesoscale field.

Furthermore, Galperin et al. (2021) investigated the seasonal variability of the upper ocean meso- and submesoscale in the framework of the quasi-normal scale elimination (QNSE) theory. They suggested that the submesoscale processes can be quantified in terms of the energy flux related to the effective submesoscale dissipation. They further pointed out that the higher variability on the submesoscales than on the mesoscale is due to the sensitivity of the energy flux to seasonal energy flux changes. Their results are consistent with the previous findings that the intensity of the submesoscale is stronger in winter and weaker in summer (e.g., Shcherbina et al., 2015; Buckingham et al., 2016; Qiu et al., 2018; Zhang et al., 2020, 2021).

As for the dissipation, Molemaker et al. (2015) points out that the submesoscale turbulence is partly unbalanced and has elevated local dissipation and mixing. Mukherjee et al. (2016) studied the generation and destruction of kinetic energy in a submesoscale-resolving simulation and concluded that the interplay between geostrophic and ageostrophic shear at the periphery of surface intensified eddies is significant for the energy dissipation. Previously, Gula et al. (2016) proposed that small-scale dissipation is enhanced by the loss of balance during submesoscale instability. Barkan et al. (2015) conducted an idealized experiment that mimics the Antarctic Circumpolar Current (ACC), which exhibits both forward and inverse energy cascades. They showed that the loss of balance due to submesoscale instabilities provide an efficient route to dissipation. As pointed out by Barkan et al. (2015), ageostrophic frontal instabilities near the surface and symmetric instabilities in convection regions contribute determinedly to kinetic energy dissipation independently of boundary processes. More recently, Carpenter et al. (2020) found that small-scale turbulence can lead to significant loss of submesoscale kinetic energy. These studies suggest that the submesoscale could also directly influence the ocean energy balance.

Ocean submesoscales are found to influence the upper ocean stratification. For example, Chrysagi et al. (2021) implemented high-resolution simulations in the Baltic Sea to explore the effect of the submesoscale on restratification processes during the lifetime of storms. They found out that the submesoscales can maintain shallow mixed layer depths rapidly after the wind events subside. The submesoscale-induced restratification of the mixed layer furthermore influences the vertical mixing. Taylor et al. (2020) studied the influence of submesoscales on the export of sinking tracers in idealized large-eddy simulations. They found that the restratification of the mixed layer by submesoscales reduces the rate of vertical mixing and enhance the export rate of sinking tracers.

Recent numerical simulations have shown that ocean submesoscales play a significant role in vertical transport, including heat and tracers. Su et al. (2018) pointed out that ocean submesoscales are critical components of the Earth's climate by transporting heat from the ocean interior to the surface. However, their models only resolve submesoscale motions at ∼10-50 km, and those motions at ∼0.1-10 km are not included. Siegelman (2020) proposed that the submesoscales are not only confined to the ocean surface mixed layer but also significant in the ocean interior down to depths of 900m. The author further pointed out that deep submesoscales are efficiently transporting heat from the ocean interior to the surface, consistent with Su et al. (2018)'s result. Furthermore, Su et al. (2020) analyzed the result of a high-resolution ocean model and found that the high-frequency submesoscale motions double the upward heat transport in winter due to the submesoscales, therefore leading to a significant influence on the global climate.

As for the vertical tracer transport by the ocean submesoscale, it draws more attention from ecologists. For instance, Siegelman et al. (2019) found the biological hotspot for the southern elephant seal and accounted it for submesoscales. Whitt et al. (2019) found that submesoscales enhance storm-driven mixing of nutrients from a biogeochemical large eddy simulation. They pointed out that the resolved submesoscales double the vertical nutrient flux during the storm and still maintain higher nutrients within the mixed layer after the storm.

In the end, although there have been a number of studies on the ocean submesoscale, our understanding is still incomplete. On the one hand, the unique characteristic of ocean submesoscales makes it difficult to observe, which impedes the verification of model results. On the other hand, the computational cost will dramatically increase with enlarging the ocean region, limiting our understanding of the behaviours and influence of submesoscales on a large scale. Hence, the future investigation of the ocean submesoscale calls for the advent of high-resolution ocean observations and the further development of computing capabilities in the upcoming decades.

1.2.2 Ocean data assimilation

Measuring the oceanic submesoscale demands high-resolution observations. As high-resolution observations are difficult to obtain due to technical reasons, the community needs to think about an alternative way to reduce the requirements from observations and still address the ocean submesoscale. There are many ways to retrieve ocean states globally or regionally at large scales and at the mesoscale. Unfortunately, few of them successfully retrieve the oceanic submesoscale. Data assimilation may be an exception, as it can combine the dynamical information from high-resolution models with observations. So far, data assimilation is one of the most plausible methods to retrieve oceanic submesoscales, especially in the case that more and more high-resolution ocean observations will be available in the future.

This section will first review the methods to retrieve ocean states and explain why data assimilation is the most plausible method to constrain the ocean submesoscale. Then I will review the developments of data assimilation techniques.

1.2.2.1 Retrieval of ocean state

Unlike the atmosphere, the lack of ocean observations makes it hard to retrieve the ocean state through observations alone. Satellite sensors have successfully measured SST, SSS and SSH in the global ocean with moderate resolutions. However, they are still rare despite the recent rapid increase in interior ocean observations by Argo, XBT, and some other underwater observing devices. Retrieving the state of the entire ocean, therefore, needs the assistance of numerical models.

The variability of the ocean surface can be documented from SSS, SST, SSH, and surface velocity field measurements. The SSS has been retrieved by satellite sensors, for instance, onboard the European Space Agency's (ESA) Soil Moisture and Ocean Salinity (SMOS) satellite (Reul et al., 2013), and the United States National Aeronautics and Space Administration's (NASA) Aquarius satellite (Le Vine et al., 2010, 2015), and by the Argo network of free-drifting profiling floats (Argo, 2020). Their combination makes the distributions of ocean salinity more accurate and robust (Boutin et al., 2013; Drucker and Riser, 2014). There are two mature operational systems for SST, namely, the Group for High-Resolution Sea Surface Temperature (GHRSST) and the CEOS SST Virtual Constellation (CEOS SST-VC) (O'Carroll et al., 2019). For SSH, there has been a continuous record for 30 years, with missions like Topex/Poseidon, Envisat and Jason. Moreover, in the following years, the surface water ocean topography (SWOT) project will be launched and provide new SSH observations at much higher resolution (Rocha et al., 2016b; Qiu et al., 2018; Zhang and Qiu, 2018). As for the surface velocity field, it has been mainly derived from SSH using the geostrophic relation. However, SSH-derived currents are only available in the off-equatorial ocean. Kozlov et al. (2020) retrieved the meso- and submesoscale velocity field in marginal ice zones from sequential synthetic aperture radar observations. Soon, the ocean surface current multiscale observation mission (OSCOM) is going to be launched and will provide a simultaneous measurement of ocean surface current from the view of satellites (Du et al., 2021).

One primary source of direct observations of the ocean interior is the Argo network, providing profiles across the global ocean (including temperature and salinity). Other measurements of the interior ocean include Expendable BathyThermography (XBT) probes, which are dropped from a ship and measure the temperature as they fall through the water column, and Conductivity Temperature Depth (CTD) sondes, which are also deployed from a ship and measure with high precision *in situ* temperature and salinity. The Argo array provides much more observations than XBT and CDT surveys; however, those data are still far from sufficient to retrieve the interior ocean state. The lack of interior observations is a significant challenge for retrieving the interior ocean.

Besides depending on the direct observations, there are some efforts to retrieve the interior ocean state from a dynamical perspective. For instance, Lapeyre and Klein (2006) examined the relationship between the interior and surface dynamics for nonlinear baroclinically unstable flows. They raised the possibility to diagnose the three-dimensional (3D) structure from only the surface density using a simple method based on the surface quasigeostrophic theory (SQG).

Furthermore, LaCasce and Mahadevan (2006) examined a dynamic method for estimating subsurface fields in the upper ocean; Isern-Fontanet et al. (2006) examined the potential of SST measurements to complement altimeter data based on the SQG theory. They pointed out that the SQG approximation may apply in predicting 3D velocity in the upper ocean layers. Despite these dynamic ways to retrieve the interior state from the surface information, a more common method is assimilating observations into numerical models, as described next.

1.2.2.2 Application of ocean data assimilation

Data assimilation is a method to combine helpful information from observations and numerical models. It is used to obtain an optimal estimation of the ”true” state based on available information, including the information from observations and the dynamical processes included in the numerical model equations. Therefore, the data assimilation technique facilitates the retrieval of the ocean state in a dynamically consistent, complete and accurate sense (Ghil and Malanotte-Rizzoli, 1991).

The history of data assimilation can be traced back to the 1920s when Richardson (1922) first brought the idea of assimilation to the subjective analysis of numerical weather forecasting. However, his attempt failed because of no filtering process adopted in his primitive equations. With the development of computers, objective analysis (OA) was applied in meteorology since the 1940s. The early OA method simply fits all observations in a small analysis area encompassing several analysis grid points by a polynomial expansion (Panofsky, 1949). Later, Gilchrist and Cressman (1954) and Cressman (1959) proposed and developed the Cressman analysis, or the successive corrections method, which introduces the concept of the background information. This method is still used currently in some simple assimilation systems. However, the OA method does not consider the errors of models or observations and lacks the theoretical foundation. This problem was solved when Gandin (1965) developed the optimal interpolation (OI) method. The OI method is based on the theory of statistical estimation, and it considers the errors of the background field and the observations. It is widely used in operational numerical weather forecasting during the 1980s and 1990s.

With the rapid development of numerical models and observational systems, the simplicity of the OI method no longer meets the requirements of such a complex system. Therefore, Sasaki (1958) proposed the variational method, which gradually became one of the mainstream operational assimilation methods (e.g., Courtier et al., 1998; Derber and Bouttier, 1999; Barker et al., 2004; Lindskog et al., 2004). The variational methods include three-dimensional variational (3DVAR) and four-dimensional variational (4DVAR) data assimilation. 4DVAR is a generalization of the 3DVAR, including the time dimension. Variational methods define a cost function ($\mathcal{J}$) and search for the state where $\mathcal{J}$ reaches its minimum.

Meanwhile, Kalman (1960) proposed the Kalman filter (KF) for linear systems. The extended Kalman filter (EKF) was developed later for the nonlinear systems (Bucy and Joseph, 1968). As the EKF requires expensive computational resources for estimating error covariance, it is often used for idealized problems in the atmospheric and oceanic sciences (Kao et al., 2004). Therefore, the ensemble Kalman filter (EnKF) (Evensen, 1994) was developed to deal with the highly nonlinear atmospheric and oceanic systems. The methods above, however, rely on linearization and Gaussian assumptions of the prior and observation errors. A nonlinear data assimilation method, the particle filter (PF), was then proposed to eliminate those limitations (Van Leeuwen et al., 2015). The PF method developed rapidly in recent years and has shown comparable performance to the EnKF in the nonlinear Lorenz96 model(Zhu et al., 2016; Wang et al., 2020).

The history of data assimilation shows a trend towards more sophisticated methods and models, more complex observation systems and increasing non-linearity. The dramatically enhanced computation ability primarily drives this trend. However, the systems with abundant submesoscale are of high non-linearity and demand enormous computation resources. It is interesting to check what key factors constrain the submesoscale in a data assimilation system.

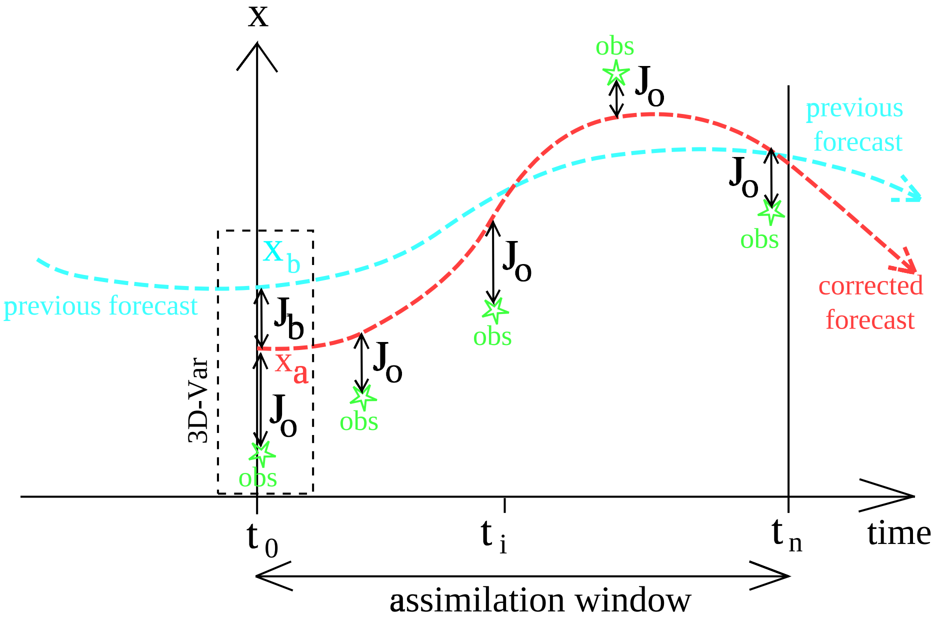

Figure 1.4: Example of 4DVAR assimilation in a numerical forecasting system. Retrieved from Bouttier and Courtier (1999, p. 35).

One of the usages of data assimilation is to produce an initial condition for a numerical forecast. As the atmosphere and ocean systems are nonlinear and chaotic, the forecast performance is essentially dependent on the initial condition. During the assimilation process, the initial condition is corrected by the observations. An excellent initial condition represents the optimal estimate of the ”true” state at the initial time and ensures the numerical model integrates forward in the ”correct” direction. Figure 1.4 shows how the model state is adjusted during one assimilation window of 4DVAR.

Ocean data assimilation has been used for producing re-analysis data of the global ocean. Stammer et al. (2002) firstly estimated the global ocean state during 1992-1997 by assimilating ocean observations into a general circulation model. They pointed out that when there are not enough ocean observations, it is challenging to ascribe the residuals to either the observations or the model, resulting in the retrieved state being less convincing. Various re-analysis products have been developed in the past decades. For example, the HYbrid Coordinate Ocean Model (HYCOM) re-analysis is produced by combining HYCOM with the Navy Coupled Ocean Data Assimilation (NCODA) system (Cummings, 2005; Cummings and Smedstad, 2013). NCODA adopts a three-dimensional variational (3DVAR) scheme and assimilates observations from satellites and *in situ* observations. Another popular dataset is the Simple Ocean Data Assimilation (SODA), which is produced by National Center for Atmospheric Research (NCAR) (Carton et al., 2000; Carton and Giese, 2008). These re-analyses reflect the real ocean state, and they improve our understanding of the past ocean state.

In addition to assimilating observations of traditional ocean variables, some unconventional observations are also assimilated. For example, Korotaev et al. (2008) tried to retrieve ocean surface current by four-dimensional variational (4DVAR) assimilation of a sequence of satellite images. Furthermore, apart from assimilating original observations into the numerical models, some derived observations are assimilated. For instance, LaCasce and Mahadevan (2006) pointed out the SQG model has the potential to assimilate SST into ocean models in a dynamical way, which is realized by assimilating the SQG-derived temperature instead of projecting SST downward into the interior using empirical relations(Tang et al., 2004).

The success of data assimilation depends on many factors. For example, in a variational assimilation system, the success relies on the design of the background errors, the observation variables, the design of the observation operator, and the observation accuracy. Unfortunately, as ocean observations at high resolution are not available, few studies addressed the retrieval of oceanic submesoscale. However, with the increasing awareness of the oceanic submesoscale recently, it will be interesting to explore which factors determine the constraining performance of oceanic submesoscales. Also, the high-resolution ocean observations planned soon (e.g., the SWOT and OSCOM missions) may help answer the limitation of those future high-resolution observations when using them to retrieve ocean states.

1.3 Study objectives

In the present work, I will first use an idealized high-resolution ocean model to characterize the kinetic energy conversion in a wind-forced submesoscale flow. This first part aims at understanding and quantifying the main processes behind the forcing of kinetic energy conversion in a surface-intensified submesoscale-rich flow. Several questions are addressed in this part:

1. What is the impact of resolved submesoscale motions on the kinetic energy conversion?
2. Where are the energy conversion terms intensified?
3. How do the conversion terms change in the presence of wind stress forcing?
4. What is the difference between cyclones and anticyclones in terms of kinetic energy conversion? Does this relation change when external forcing is imposed?

In the second part of this dissertation, I will investigate how to constrain submesoscale flows in an eddy-resolving adjoint-based data assimilation model. The following questions are sought in this part:

1. To what extent is surface information enough to constrain the three-dimensional submesoscale field?
2. What is the assimilation sensitivity to horizontal and temporal resolution and noise level of the observations?
3. What is the predictability timescale of the submesoscale flow?

1.4 Thesis outline

This thesis is structured as follows. Chapter 2 describes the methodology employed. The model set-up and spin-up will be first described. Then the framework of the adjoint model will be introduced.

Chapter 3 studies the kinetic energy conversion in a wind-forced submesoscale flow. The comparison between the wind forced case and the unforced control case will be thoroughly investigated. In addition, the different roles of cyclonic and anticyclonic eddies in the kinetic energy conversion will be explored statistically.

Chapter 4 investigates the problem of constraining the submesoscale in an adjoint-based data assimilation system. First, different assimilation windows will be tested. Then several sets of experiments will be implemented to study the sensitivity of retrieving the submesoscale to the observation resolution and error. The contents of chapter 3 and chapter 4 have been collected into two independent papers, which are going to be submitted soon.

Finally, chapter 5 summarizes the main conclusions of this thesis and outlines future work.

Chapter 2

Methodology

This thesis includes two main parts. The first part addresses the impact of submesoscale processes on kinetic energy conversion, while the second part focuses on constraining the submesoscale in an adjoint-based data assimilation system. As pointed out in the previous chapter, current observational systems are not adequate to fully measure three-dimensional ocean submesoscale structures. A systematic study of both parts therefore relies on high-resolution numerical simulations. In this chapter, the numerical model used in my study is described, followed by a description of the setup used in the subsequent experiments. The adjoint model used in this study is afterwards described.

2.1 The numerical ocean model and setup

2.1.1 The forward model

In this model-based study, I use the Massachusetts Institute of Technology general circulation model (MITgcm, Marshall et al. (1997)). The MITgcm is here used in both hydrostatic and non-hydrostatic integrations. Non-hydrostatic conditions are used to study the impact of the submesoscale phenomena on the kinetic energy conversion, and hydrostatic conditions are applied in the data assimilation study, as hydrostatic simulations are computationally less expensive.

2.1.2 Model configuration and spin-up

Our simulations consist of an idealized open-ocean domain, which is 832×832 km wide and 300 m deep, configured with 500-m and 5-m horizontal and vertical resolutions, respectively. The f-plane approximation is assumed, evaluated at the latitude 45°N. Double-periodic boundary conditions are applied. We adopt the K-profile parameterization (KPP) (Large et al., 1994) for vertical mixing.

Parameter	Value	Description
f_0	$1.0284 \times 10^{-4}\text{s}^{-1}$	reference Coriolis parameter
A_4	$2{\times}10^5\text{m}^4\ \text{s}^{-1}$	lateral biharmonic viscosity
A_v	$10^{-4}\text{m}^2\ \text{s}^{-1}$	vertical viscosity
K_4	$10^2\text{m}^4\ \text{s}^{-1}$	lateral biharmonic diffusion coefficient
K_r	$10^{-5}\text{m}^2\ \text{s}^{-1}$	vertical diffusion coefficient
Δt	90 s	time step

Table 2.1: List of key model parameters.

Some key configuration parameters are included in Table 2.1.

The initial conditions are composed of two parts, a steady stratified background and an anomalous cold pool in the middle of the domain (Figure 2.2). The background temperature and salinity are horizontally uniform and decline with depth as a hyperbolic tangent function as follows:

$$T(z) = 20 - 10\tanh(\frac{z-2.5}{200}) \tag{2.1}$$

$$S(z) = 36.5 - \tanh(\frac{z-2.5}{200}) \tag{2.2}$$

where z is depth, and T and S are temperature and salinity, respectively.

The cold pool, which has two sinusoidal density fronts on its north and south boundaries to make it more unstable, has a lower temperature and less salinity than the surrounding. The temperature decreases linearly with depth until reaching the background temperature. The salinity is constant in the whole cold pool. This temperature and salinity distribution ensure that the cold pool's water is always heavier than its surrounding at the same depth. Figure 2.1 shows the vertical profile of the initial temperature and salinity and the corresponding potential density and buoyancy frequency. As discussed above, Figure 2.2 illustrates the density distribution of the initial condition.

The forward model is spun up from the above state for approximately one year until abundant mesos- and submesoscale features prevail. Figure 2.3 shows the distribution of potential density at the surface after spin-up. The figure reveals a richness of submesoscale patterns, including fine filaments, vortices, and sharp density fronts. The simulations performed hereafter are based on this spin-up final state.

2.1.3 Twin simulations with and without wind forcing

Once the eddy field was established, two simulations were continued: the first still unforced and the second applying wind stress forcing. The wind stress was spatially

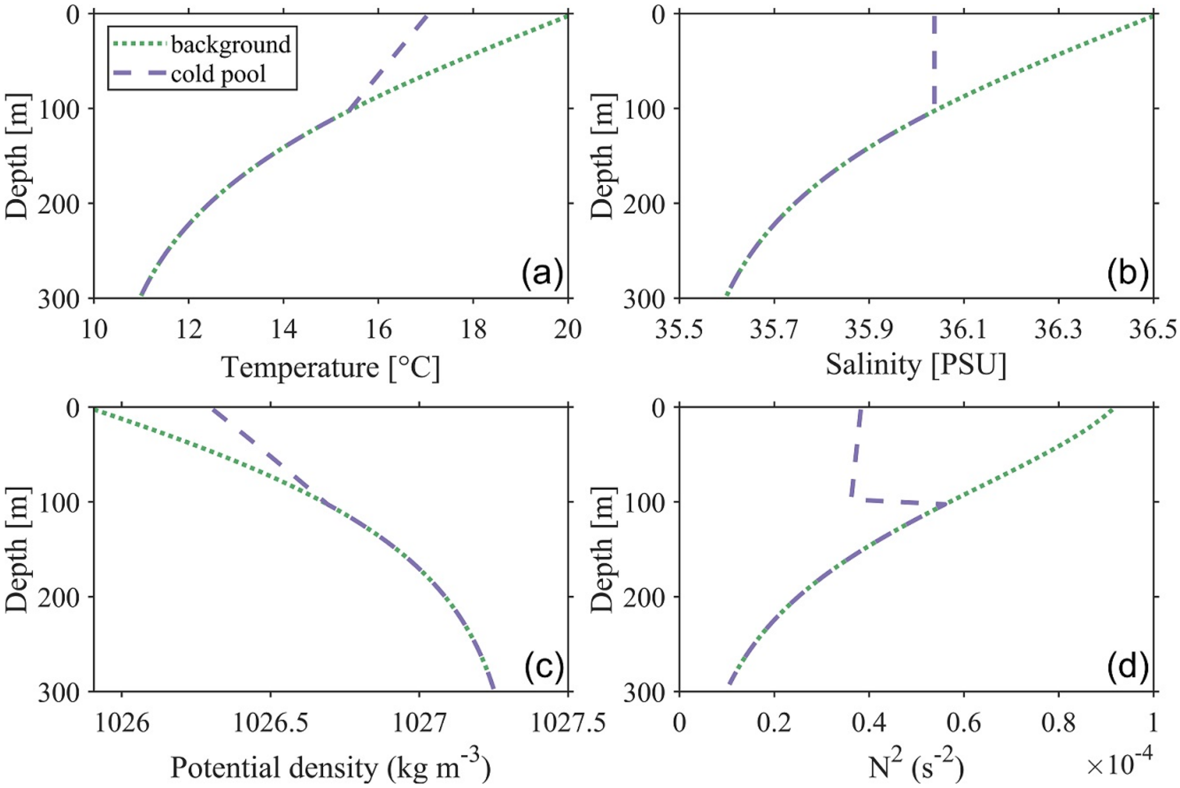

Figure 2.1: Initial Temperature and salinity and corresponding potential density and buoyancy frequency profiles in the model spin-up run.

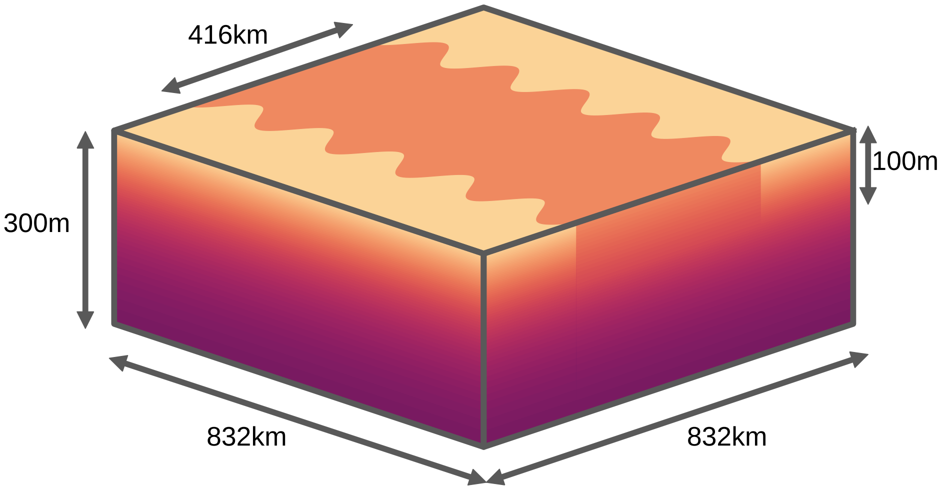

Figure 2.2: Schematic view of the numerical ocean box. A cold pool is located in the middle of the upper ocean. The color shows the density distribution of the initial condition, with darker colors indicating denser water.

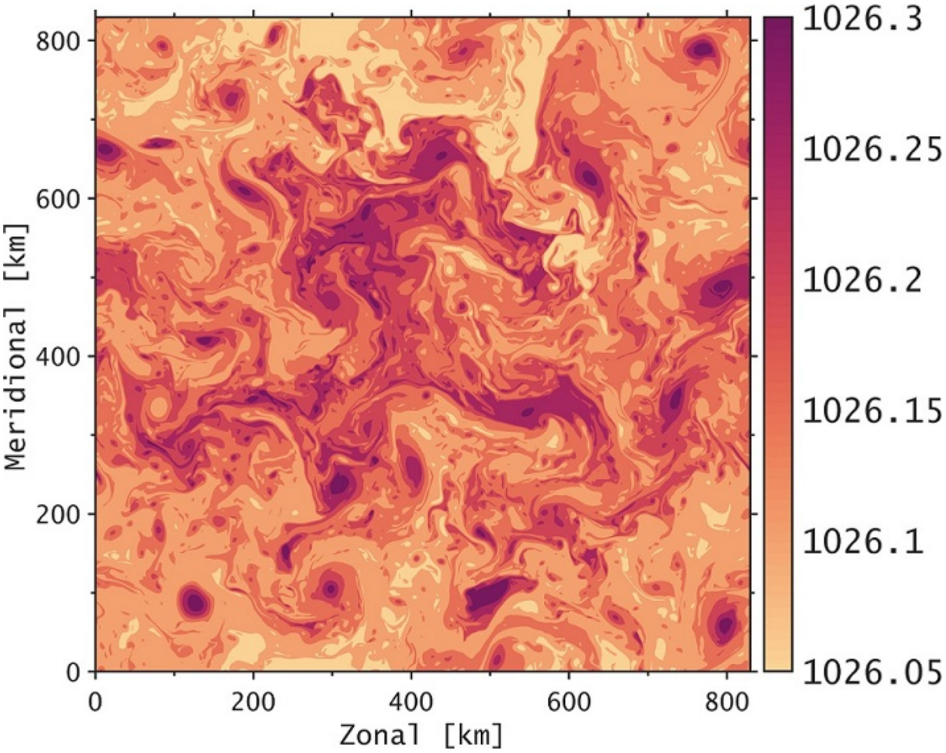

Figure 2.3: Distribution of potential density at the surface after the model spin-up.

uniform and resonant at the inertial frequency (as stated above, a f-plane is assumed and evaluated at the latitude of 45°N). The two forward simulations lasted 67 days, and results were output on an hourly basis.

The wind stress forcing was prescribed as:

$$(\tau_x, i\tau_y) = \tau_0 e^{-ift}, 0 \leq t \leq T_0 \tag{2.3}$$

where τ_x and τ_y are the zonal and meridional wind stress components, respectively; τ_0 is the constant wind stress magnitude (here τ_0=0.15 Nm^{-2}); f is the inertial frequency and T_0 (≈17h) is the inertial period. The wind stress forcing pulse was applied every 30 days and thus repeated three times in our experiment.

The 500-m horizontal resolution was enough to resolve submesoscale features with scales larger than $\mathcal{O}(1)$ km. The resulting flow field is composed of eddies and abundant filaments and fronts surrounding them (Figure 2.4) in both the unforced and forced runs. However, the eddies were split into smaller sized eddies, and the filament and frontal structures were more complex in the wind-forced run, which featured an impressive enhancement of submesoscale motions.

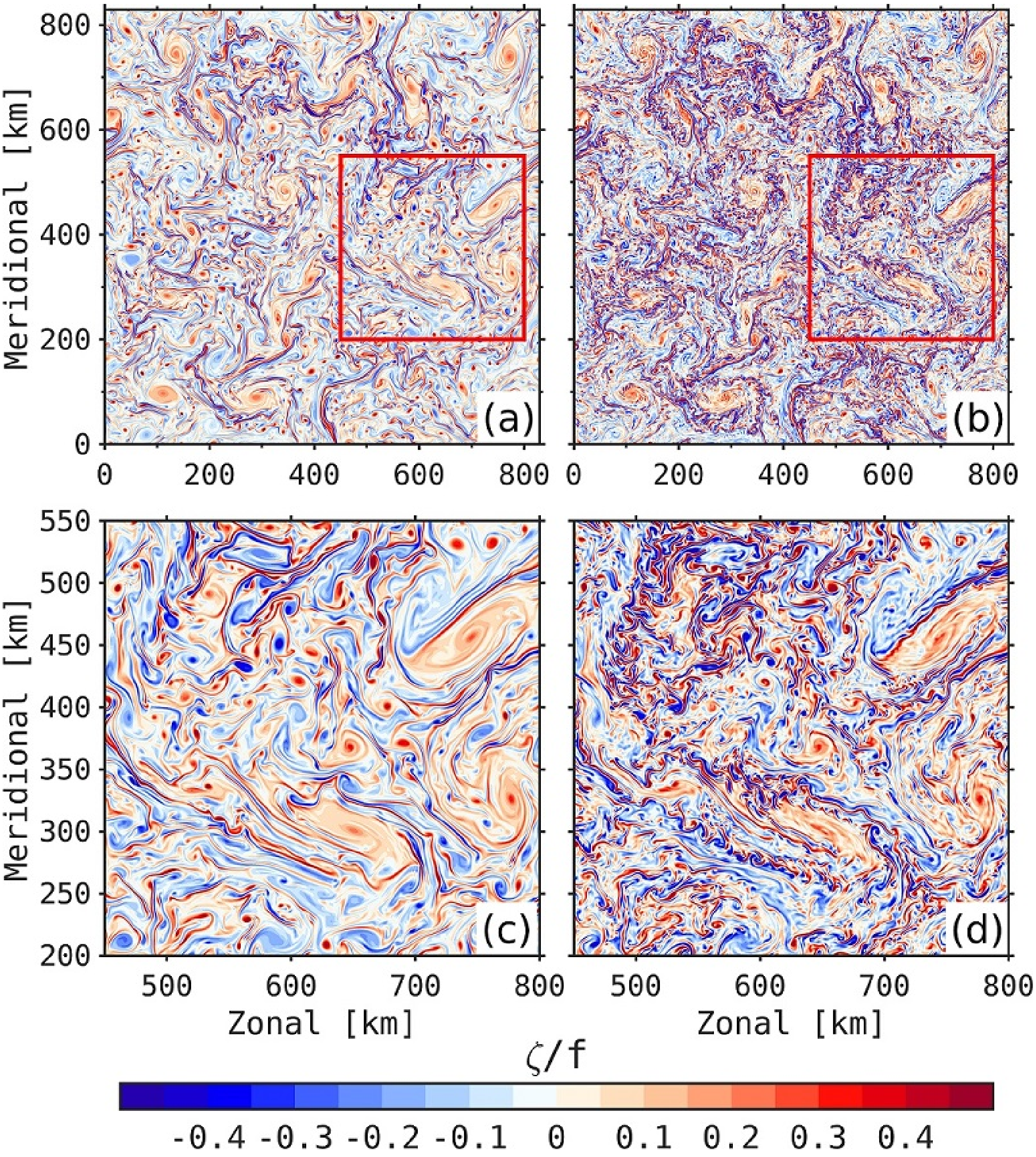

Figure 2.4: Snapshots of normalized relative vorticity, ζ/f, at T = 20 days at the surface for the full domain: (a) unforced run and (b) wind-forced run. (c) and (d) present zoomed domains denoted by red rectangles in (a) and (b).

2.2 The adjoint model

The adjoint of the MITgcm is used in my 4DVAR data assimilation experiments. The cost function is defined as:

$$\mathcal{J}(\mathbf{x_0}) = \frac{1}{2}(\mathbf{x_0} - \mathbf{x_b})^{\mathrm{T}}\mathbf{B}^{-1}(\mathbf{x_0} - \mathbf{x_b}) + \frac{1}{2}\sum_{\mathbf{k=1}}^{K}[\mathbf{y_k} - \mathcal{G}_{\mathbf{k}}(\mathbf{x_0})]^{\mathrm{T}}\mathbf{R_k}^{-1}[\mathbf{y_k} - \mathcal{G}_{\mathbf{k}}(\mathbf{x_0})]. \quad (2.4)$$

The formulation of (2.4) and meaning of symbols can be found in Appendix A.1. To minimize $\mathcal{J}(\mathbf{x_0})$, the adjoint model $\mathbf{M}^{\mathrm{T}}$ is required to compute the gradients of the cost function with respect to the control variables x_0. The formulation of $\mathbf{M}^{\mathrm{T}}$ is described in Appendix A.2.

To calculate the gradients, $\nabla\mathcal{J}(\mathbf{x_0})$, we do a forward integration with the forward model and perform a backward integration with the adjoint model, the latter forced by the model-observations data differences. This is repeated in an iterative process, and as the number of iterations increases, the minimum of $\mathcal{J}(\mathbf{x_0})$ will be approached and the corresponding $\mathbf{x_0}$ (which is our target) is retrieved as the optimal initial condition for the model forecast.

The core of the 4DVAR is therefore to calculate $\nabla_{\mathbf{x_0}}\mathcal{J}$ and thus to obtain the adjoint model $\mathbf{M}^{\mathrm{T}}$. In this work, the adjoint model was built using an Automatic Differentiation (AD) tool. This software tool (Transformation of Algorithms in Fortran - TAF, Giering and Kaminski (1998)) automatically transforms the forward code in its adjoint code. The technical realization of the adjoint code is beyond the scope of this thesis and will therefore not be addressed in detail.

The process of a complete 4DVAR experiment is summarized in Figure 2.5. The M1QN3 program, a solver of large-scale unconstrained minimization problems (Gilbert and Lemaréchal, 1989), is used to iteratively search for the optimal $\mathbf{x_0}$ for $\mathcal{J}(\mathbf{x_0})$. The core of M1QN3 is a variable-storage quasi-Newton method, which is based on the quasi-Newton principle but does not store any matrix of order n (the dimension of the variable). Therefore variable-storage quasi-Newton methods make it possible to optimize large-scale models as large as $n \sim 10^8$.

The forward model begins from an initial state ($\mathbf{x_0^{(0)}}$, first guess) and calculates the corresponding cost function ($\mathcal{J}(\mathbf{x_0})$) as it integrates forward. If the difference with the latest cost function is smaller than a given criterion (ϵ), the current initial state ($\mathbf{x_0^{(k)}}$) is the optimal state we are seeking. Otherwise, the adjoint model is run to calculate the gradient of the cost function ($\nabla\mathcal{J}(\mathbf{x_0})$) with respect to the initial conditions. Finally, the M1QN3 tool is run to search for the minimizing direction of $\mathcal{J}(\mathbf{x_0})$. The above procedure is iteratively repeated until the optimal initial state ($\mathbf{x_0}$) is determined.

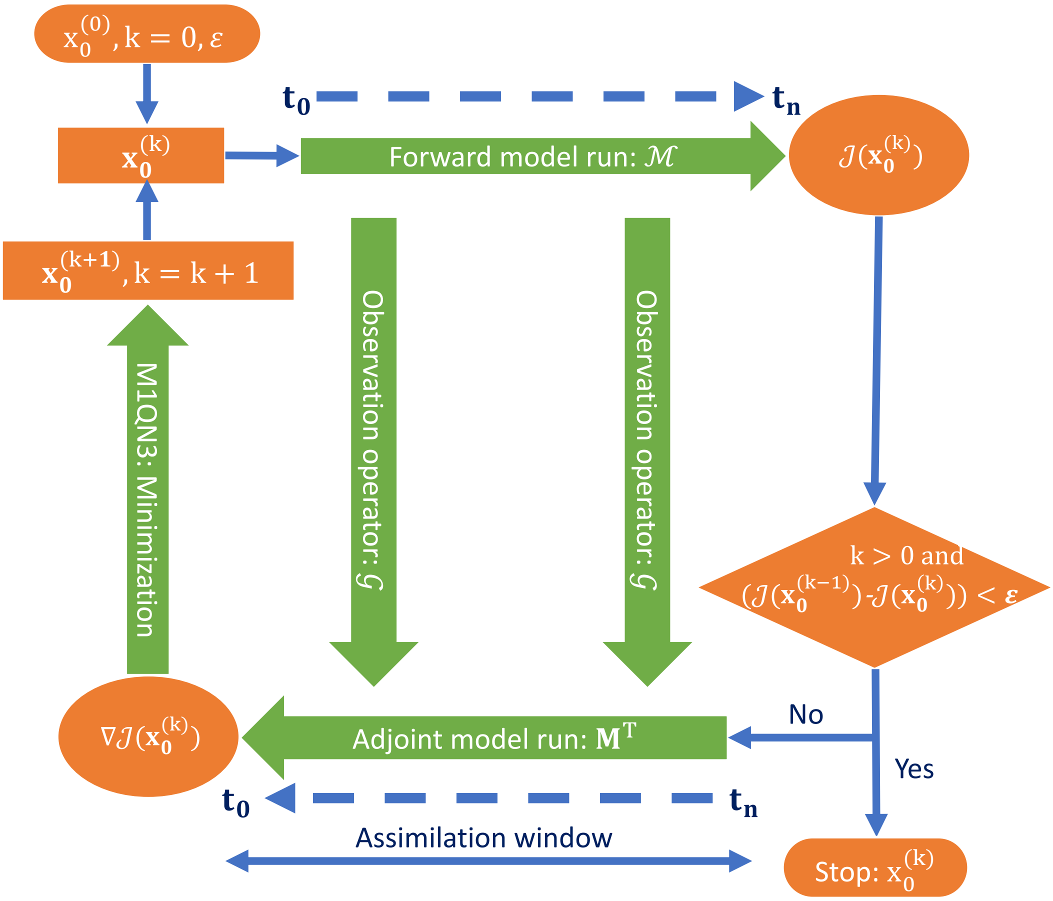

Figure 2.5: Schematic diagram of the 4DVAR data assimilation process. Retrieved from Lyu (2017).

Chapter 3

Kinetic energy conversion in a wind-forced submesoscale flow[1]

3.1 Introduction

The Lorenz Energy Cycle (LEC) is a classic concept to depict the atmosphere and/or ocean energy balance (e.g., Ferrari and Wunsch, 2010; Zemskova et al., 2015; Ashkenazy and Tziperman, 2016; Chen et al., 2016), which was first used to describe dynamical processes in atmosphere (Lorenz, 1955). Four energy reservoirs, i.e., mean kinetic energy (K_m), eddy kinetic energy (K_e), mean available potential energy (P_m) and eddy available potential energy (P_e), together with the respective generation, dissipation, and conversion terms compose the LEC. The available potential energy is defined as the difference between the total potential energy - the sum of the potential and internal energies - and the minimum total potential energy under any adiabatic redistribution of mass (Lorenz, 1955). Inferring the full oceanic LEC from observations remains impossible, so the focus is put on using ocean models.

Recently, scientists have explored the oceanic LEC with high-resolution models in global and regional configurations. For instance, Wu et al. (2017) studied the impact of intensified westerlies on the LEC in the Southern Ocean with a global eddy-permitting ocean-sea ice model. They suggested that all energy conversions are enhanced under stronger wind forcing with stronger westerlies. von Storch et al. (2012) investigated the LEC in an eddy-resolving simulation using the Max-Planck Institute of Meteorology ocean model. Their study focused essentially on global energy budgets and did not address in detail the spatial distribution of the kinetic energy, primarily as a function of depth, nor addressed the temporal variations in the budget terms and their relation to climate indicators.

---

[1] Li S., N. Serra and D. Stammer (2021): Kinetic energy conversion in a wind-forced submesoscale flow. *To be submitted.*

Furthermore, Jüling et al. (2018) studied the multidecadal variability in the Southern Ocean with a LEC analysis and found that the baroclinic energy pathway is one of the crucial aspects of the variability. After analysing the time series of spatially integrated LEC terms, Jüling et al. (2018) indicated that the result is sensitive to the choice of integration region since positive and negative anomalies can counterbalance each other regionally. It implies a regional difference in LEC distributions and reminds us of the essential reasons for those differences.

There are many potential factors responsible for those regional variations, e.g., topography, wind forcing, solar radiation, precipitation, .etc. Nevertheless, they are not the only reasons for those differences. According to the balance equations, the flow variations are the most relevant factors in determining LEC reservoirs and conversion terms. All previous LEC studies were based on eddy-permitting or even coarser models, and the submesoscale processes were not resolved in those simulations. As previously pointed out, the submesoscales play essential yet not fully known roles in the ocean energy balance. This suggests that the impact of submesoscales on the energy balance, which LEC quantifies, has not been addressed and that this subject is worth a systematic investigation.

The eddy kinetic energy is one of the most important components of the LEC. Despite recent progress in measuring the mesoscale (order of 100 km) ocean eddy field with satellite missions, containing the major fraction of ocean kinetic energy, many questions still remain regarding the generation, conversion and dissipation mechanisms of eddy kinetic energy. Although the ocean energy balance has been quantified by von Storch et al. (2012), their simulations are too coarse to resolve ocean submesoscales. The impact of ocean submesoscales on ocean energy conversion is, therefore, not addressed.

In this part, I use the output from an idealised 500-m resolution ocean numerical simulation to study the conversion of K_e in the absence and presence of wind stress forcing, wherein the latter one more abundant ocean submesoscale features appear. By contrast to the simulation without forcing, the impact of additional submesoscale activity on K_e conversion will be investigated.

3.2 Description of the flow field

The results described in this chapter are based on the hourly output of the twin simulations described in chapter 2. 500-m horizontal resolution is enough to resolve submesoscale characteristics with scales $\mathcal{O}(1)$ km. The flow field was composed of eddies, as well as abundant filaments and fronts surrounding them (Figure 2.4), this being true in both the unforced and the forced runs. However, in the forced case, the eddies split into smaller sized eddies, and the filamentary and frontal structures were more sophisticated, leading to an impressive enhancement of submesoscale motions by wind events.

Besides the vertical component of relative vorticity, the lateral strain rate (α) is an important variable describing the flow field (Shcherbina et al., 2013; Chelton et al., 2011). α is defined as

$$\alpha = \sqrt{\mathrm{Ss}^2 + \mathrm{Sn}^2}, \tag{3.1}$$

where Ss and Sn are the shear strain and the normal strain, respectively. They are defined as

$$\mathrm{Ss} = v_x + u_y, \tag{3.2}$$

$$\mathrm{Sn} = u_x - v_y, \tag{3.3}$$

where u and v are the zonal and meridional velocity components, subscripts denote partial differentiation. The background strain primarily comes from mesoscale currents and eddies (McWilliams, 2016). By comparing with the no forcing run (Figure 3.1), wind events dramatically increased the strain rate surrounding eddies. Wind events therefore created small steep fronts along filaments, leading to a strongly unstable flow field.

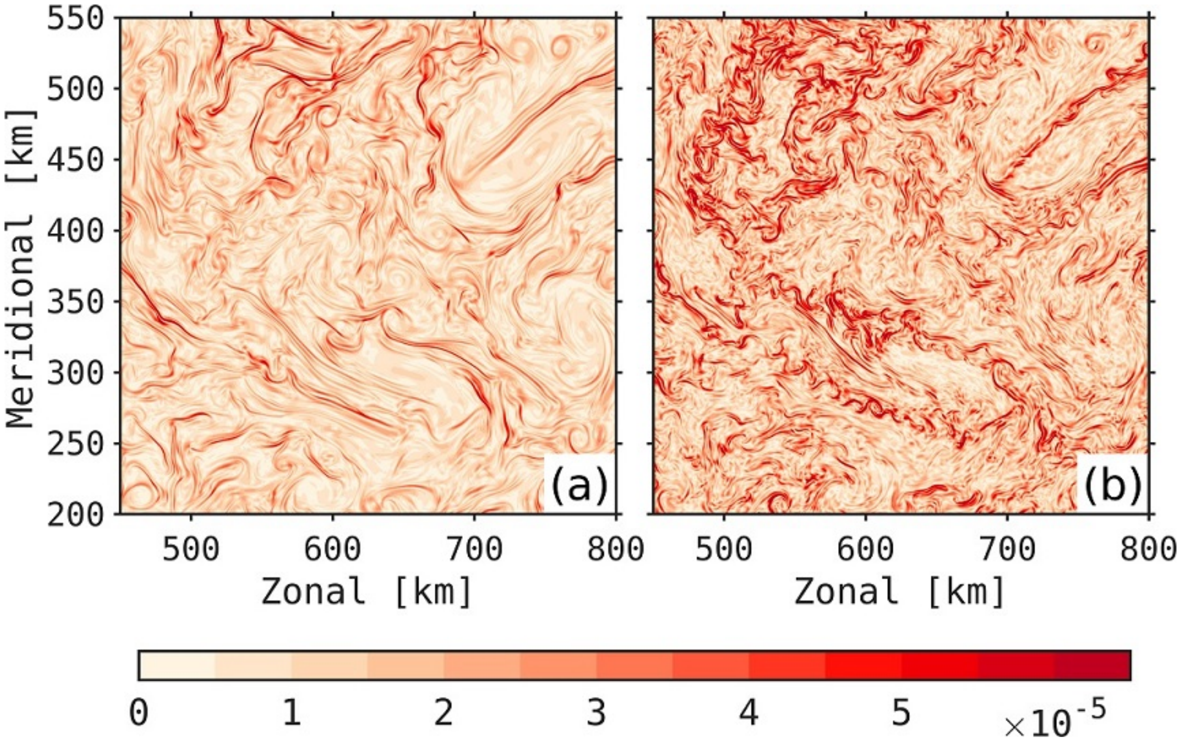

Figure 3.1: Snapshots of lateral strain rate α at T = 20 day at the surface in the same domain as Figure 2.4c (a) and Figure 2.4d (b).

The spectrum of zonal velocity describes the kinetic energy distribution in corresponding spectral space. In the frequency space, a broad peak at the inertial frequency and several weak peaks at superinertial frequencies characterised the inertial oscillation and superinertial oscillation in the forced run (Figure 3.2a). These oscillations are introduced by the variable wind, which changes at the inertial frequency at which the ocean is resonant. Such winds can especially excite inertial oscillations in the upper ocean (Callies and Ferrari, 2013). In the wavenumber space, there was approximately 60∼70% more kinetic energy contained at the surface at all scales in the forced run than that in the unforced run (Figure 3.2b). The slope $k^{-5/3}$ from the Kolmogorov's surface-quasigeostrophic (SQG) turbulence theory is matched further at higher wavenumbers, indicating that the dissipating scale was decreased from 33 km to 14 km by wind events, here supposed to be contributed by the increased submesoscale motions (Callies and Ferrari, 2013; Vallis, 2017).

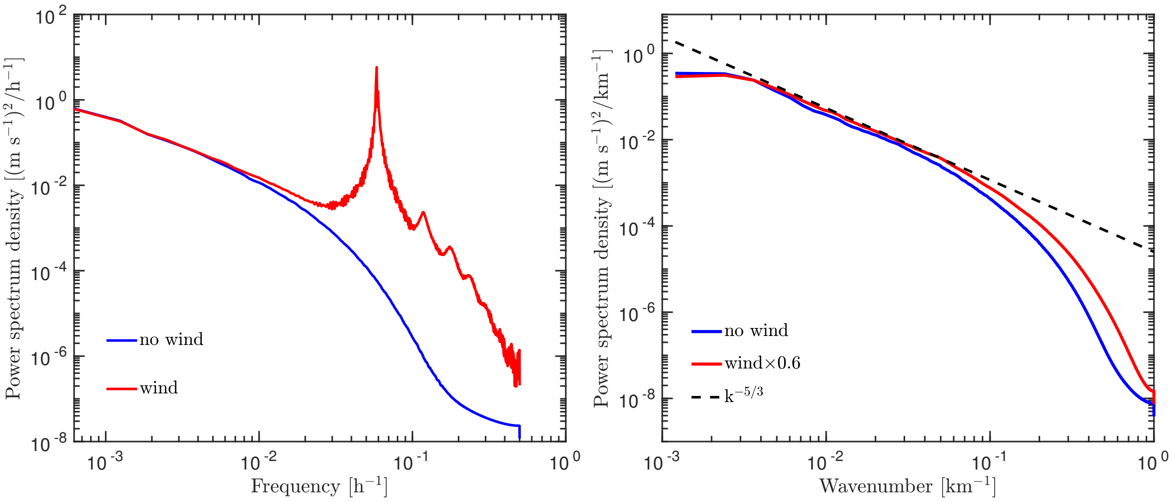

Figure 3.2: (left) Frequency and (right) wavenumber spectrum of zonal velocity at the surface. Note that the wavenumber spectrum of the forced run has been multiplied by a factor.

In summary, 1) both runs resolved well submesoscale flows, but the forced run contained more abundant submesoscale motions; 2) the wind forcing excited inertial and superinertial motions in the forced run.

3.3 Kinetic energy reservoirs and conversion terms

3.3.1 Quantifying the Lorenz energy cycle

Four energy reservoirs are used to describe the time-mean balance: P_m and P_e, the mean and eddy available potential energy, and K_m and K_e, the mean and eddy kinetic energy. Together with the corresponding conversion, generation, and dissipation rates, they compose the ocean's Lorenz energy cycle (LEC).

The three reservoirs relevant for the study of kinetic energy are defined as (von Storch et al., 2012):

$$\begin{aligned} P_e &= -\int_V \frac{1}{2}\frac{g}{n_0}\overline{\rho{*}'^2}\mathrm{d}V, && (3.4)\\ K_m &= \int_V \frac{1}{2}\rho_0(\bar{u}^2+\bar{v}^2)\mathrm{d}V, && (3.5)\\ K_e &= \int_V \frac{1}{2}\rho_0\overline{(u'^2+v'^2)}\mathrm{d}V, && (3.6) \end{aligned}$$

where $\rho*$ is the time mean of density anomalies defined by:

$$\rho* = \rho - \rho_{ref}. \tag{3.7}$$

Here ρ_{ref} is the reference density defined by the area average of the time mean density at each level, $\rho_0 = 1025\text{kg m}^{-3}$ and g is gravity. $\int_V \mathrm{d}V$ indicates the integral over the whole domain. $\overline{X}$ denotes the time mean of X and X' denotes the deviation from $\overline{X}$, i.e., $u' = u - \bar{u}$, $v' = v - \bar{v}$ and $\rho*' = \rho * -\overline{\rho*}$. $n_0(z)$ is the vertical gradient of the layer-averaged and time-mean local potential density.

The conversion terms related to eddy kinetic energy are defined as:

$$\begin{aligned} C(K_m, K_e) &= -\int_V (\rho_0\overline{u'\mathbf{u'}}\cdot\nabla\bar{u} + \rho_0\overline{v'\mathbf{u'}}\cdot\nabla\bar{v})\mathrm{d}V, && (3.8)\\ C(P_e, K_e) &= -\int_V g\overline{\rho' w'}\mathrm{d}V, && (3.9) \end{aligned}$$

the positive $C(X,Y)$ implies the conversion from X to Y and thus $C(X,Y) = -C(Y,X)$. The full derivation of the eddy kinetic energy equation is attached in Appendix A.3.

All terms related to K_e, except for generation and dissipation, are calculated and compared in Figure 3.3 for the two runs. Regarding the reservoirs, K_e increased approximately five times due to the wind events, while P_e only increased 2.5 times, and K_m nearly had no change.

More meaningful differences were introduced by the wind forcing regarding the conversion terms. The directions of $P_e \leftrightharpoons K_e$ and $K_m \leftrightharpoons K_e$ were both reversed. $C(P_e, K_e)$ was 5.85 MW in the unforced run, indicating conversion from P_e to K_e; while it was -20.8 MW in the forced run, indicating conversion from K_e to P_e. As extracting P_e to K_e always implies baroclinic instability, such reverse induced by wind events therefore undermined the dominance of baroclinic instability (Bleck, 1985). Similarly, K_e was transferred to K_m with a rate of 4.76 MW in the unforced run while it was -3.3 MW in the forced run. As barotropic instabilities grow by extracting kinetic energy from the basic mean flow (McAvaney and Holland, 1995), the negative sign of $C(K_e, K_m)$ implies wind events greatly energised the barotropic instabilities.

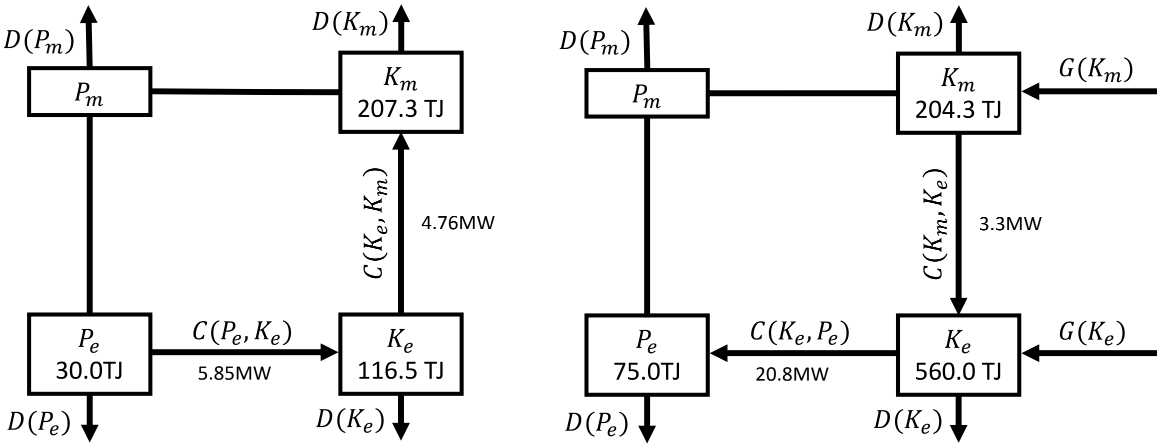

Figure 3.3: Lorenz Energy Cycle (LEC) for the unforced run (left) and the wind stress forced run (right). The $D(X)$ and $G(X)$ represent the dissipation and generation rates of X, respectively. Energy reservoirs are in terajoules (TJ), rates of conversion in megawatts (MW).

Now we turn to transient processes. Throughout this thesis, we use lower-case letters to denote corresponding transient LEC-terms, e.g., k_e represents K_e without time mean.

The layer-integrated, time-averaged k_e profile shows the unequal impact induced by wind events on different depths (Figure 3.4a). k_e was dramatically increased by the wind events by nine times in the mixed layer and considerably in the pycnocline. That sounds reasonable as the wind forcing mainly influences the upper ocean, especially the mixed layer. This unequal impact is reconfirmed by the evolution of their increment Δk_e, which is defined as the k_e difference between the forced and unforced run (Figure 3.4b).

Apart from the spatial differences, k_e also shows a strong temporal variation related to three wind events during the run. There were three 17-hours long wind stress forcing events during the whole integration period, which are highly consistent with the three Δk_e ridges in Figure 3.4b. Δk_e reached its local maximum rapidly as soon as the forcing was added and then weakened gradually until the next forcing event. Interestingly, those influences were unequal for each wind event, although the wind was identical every time.

The impact induced by the first wind event was greater and lasted longer than that by the second wind event and the foreseeable third. One possible explanation is that submesoscale motions could efficiently counteract kinetic energy input by wind stress. Due to the stimulus of the first wind event, the submesoscale motions before the second wind event were much more abundant and energetic than those before the first wind event. The enhanced submesoscale motions counterbalanced the kinetic energy introduced by the second wind event more than by the first wind event. Therefore the remained Δk_e enhancement was weaker for the subsequent wind events.

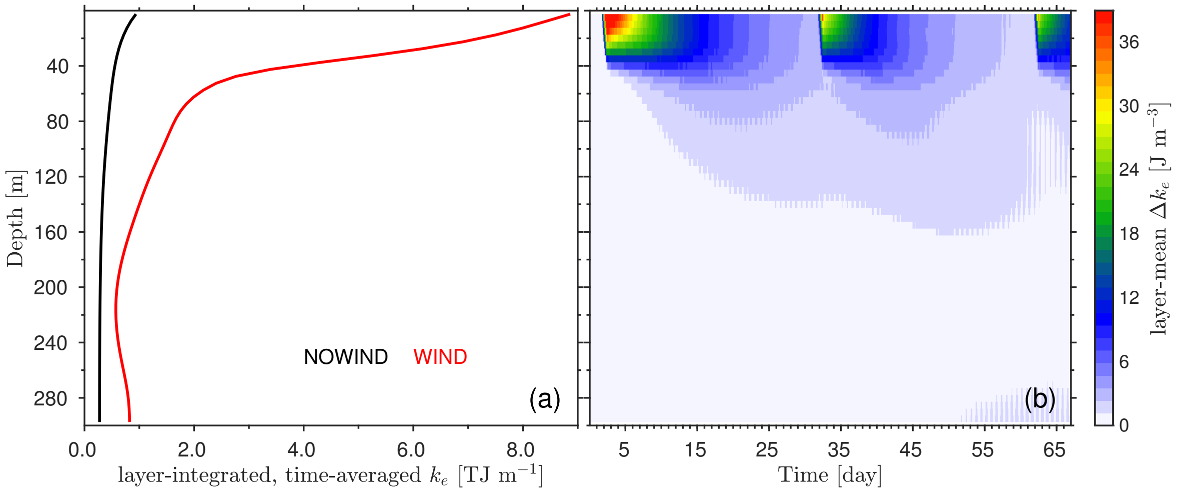

Figure 3.4: (a) Layer-integrated, time-averaged k_e profile for the unforced run (black line) and forced run (red line). The average is taken among the whole 67-days period. The units are TJ m^{-1}. (b) Variation of layer-mean Δk_e with time and depth. Δk_e is defined as the difference between the forced and unforced runs.

3.3.2 Conversion between p_e and k_e

We address here in more detail the transient conversion between p_e and k_e. First, the layer-integrated and time-averaged $c(p_e, k_e)$ reached 0.3 MW m^{-1} in the mixed layer in the forced run, three times larger than the maximum value ($\sim$0.1 MW m^{-1}) in the unforced run (Figure 3.5c). On the other hand, $c(p_e, k_e)$ kept positive through all layers in the unforced run (Figure 3.5a,Figure 3.5c), revealing the dominance of baroclinic instability in the upper ocean. On the other hand, this sign changed to negative at the base of the mixed layer and kept so below in the forced run (Figure 3.5c).

Second, $c(p_e, k_e)$ has a strong temporal variation in the forced run (Figure 3.5b). $c(p_e, k_e)$ oscillated with time in the forced run, and such oscillation was excited by the oscillating wind. Third, recalling from the integrated result over the full domain in Figure 3.3 and combining the layer-integrated result in Figure 3.5c, we conclude that in the forced run, the reverse of converting direction of $c(p_e, k_e)$ is mainly contributed by the layers below the base of the mixed layer.

The question of why the layer-integrated, time-averaged $c(p_e, k_e)$ changed sign in the mixed layer in the forced run remains. The definition of $c(p_e, k_e)$ (Equation 3.9) reveals that the conversion is dependent on the anomaly of density (ρ') and vertical velocity (w'). We list all possible situations regarding different signs of $c(p_e, k_e)$ in Table 3.1. At different moments, $c(p_e, k_e)$ could be negative or positive at any depth (Figure 3.5b), indicating the downwelling or upwelling of dense or light water. The average overtime eliminated the oscillating fluctuations, with the net effect only remaining. Therefore, according to Figure 3.5c and Table 3.1, 1) the downwelling of dense water and/or upwelling of light water dominated in the mixed layer, leading to the flattening and/or lowering of isopycnals, respectively; below the mixed layer, 2) the upwelling of dense

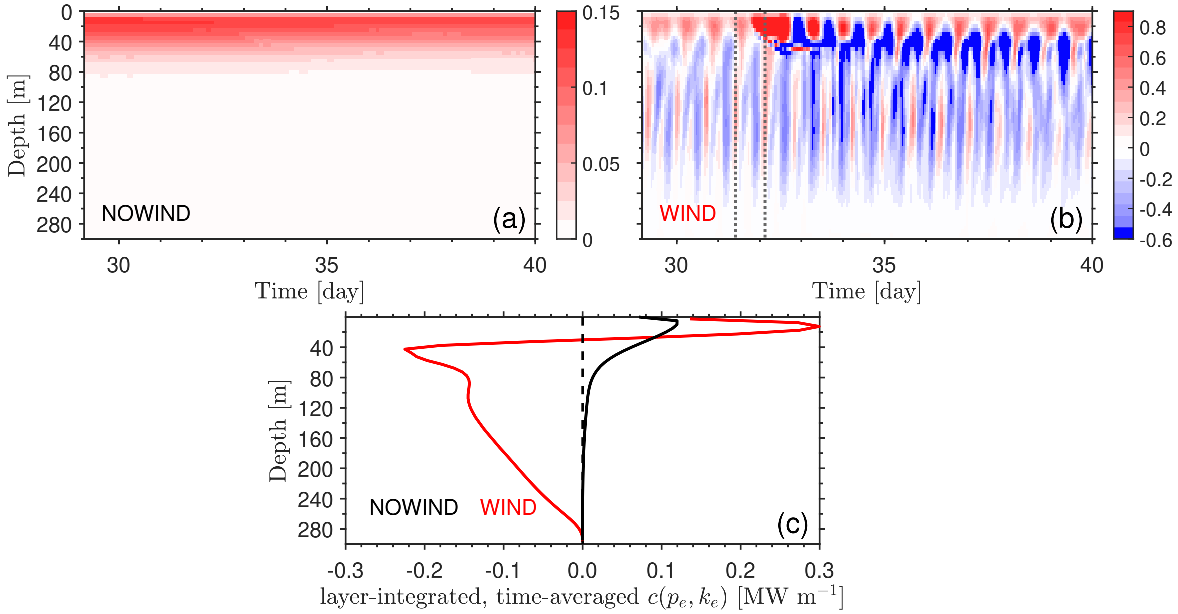

Figure 3.5: (a) Depth-time dependence of layered integrated $c(p_e, k_e)$ for the unforced run. (b) The same as (a) but for the forced run. The presented period is around one wind event, which happens between the two vertical dashed lines depicted in (b). (c) Layer-integrated, time-averaged $c(p_e, k_e)$ profile for the unforced run (black line) and forced run (red line).

water and/or downwelling of light water dominated, leading to the sloping and/or rising of isopycnals, respectively. A further discussion about which processes were indeed involved is presented ahead.

$c(p_e, k_e) > 0$	$p_e \to k_e$	$\rho' > 0$ and $w' < 0$	downwelling of dense water	flattening of isopycnal
		$\rho' < 0$ and $w' > 0$	upwelling of light water	lowering of isopycnal
$c(p_e, k_e) < 0$	$k_e \to p_e$	$\rho' > 0$ and $w' > 0$	upwelling of dense water	sloping of isopycnal
		$\rho' < 0$ and $w' < 0$	downwelling of light water	rising of isopycnal

Table 3.1: All possibilities regarding different signs of $c(p_e, k_e)$.

We first consider the oscillating fluctuations carefully, which are also revealed in the spectral space. The $c(p_e, k_e)$ frequency spectrum was calculated on individual horizontal grid points and then averaged over the whole horizontal domain. In the forced run, $c(p_e, k_e)$ has several peaks at frequencies multiple of f_0 nearly in the entire ocean domain (Figure 3.6b). Such peaks do not exist in the unforced run (Figure 3.6a). We select three depths to depict their frequency spectra in the forced run (Figure 3.6c). The spectral value at $2f_0$ or higher-order frequency has comparable magnitude as the value at f_0, and larger than the subinertial frequency range ($0 \leq f \leq 0.05\mathrm{h}^{-1}$), which implies that $c(p_e, k_e)$ is governed by inertial and superinertial motions. On the other hand, the inertial patterns were quite weak in the no wind run, and no superinertial signals appeared. We can conclude that the wind stress forcing excited inertial and superinertial motions, and therefore dramatically enforced the conversion between p_e and k_e.

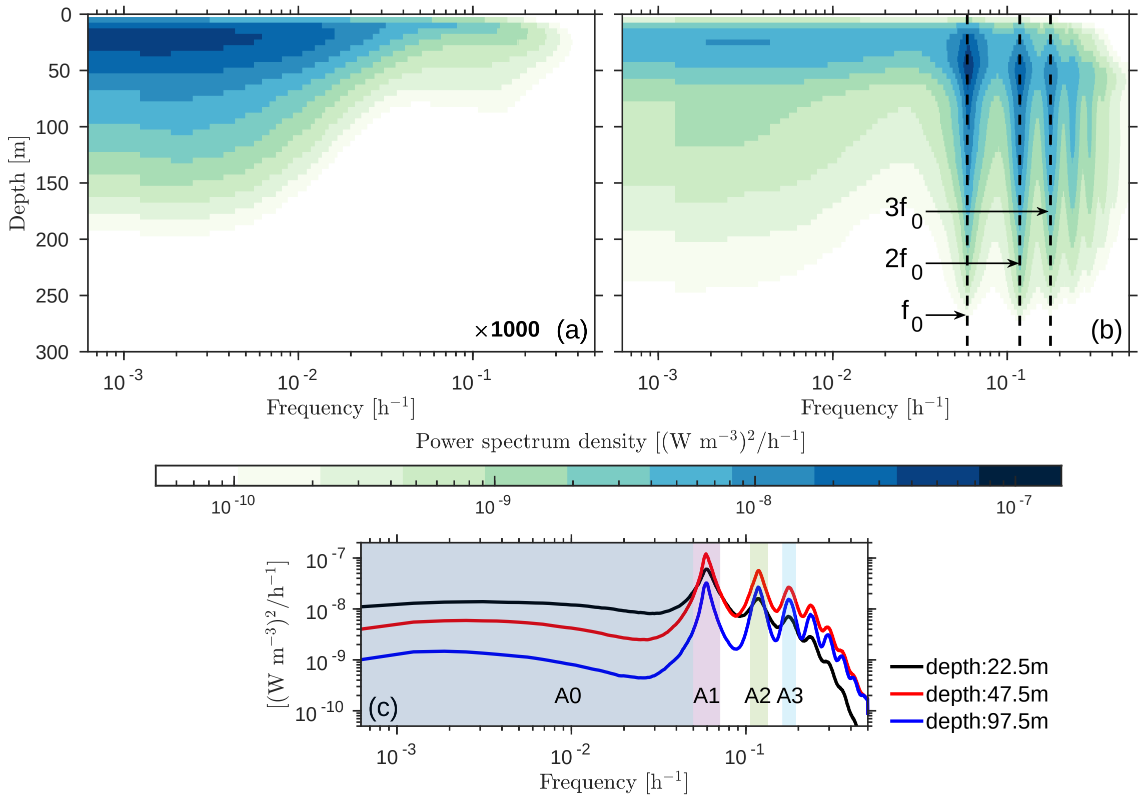

Figure 3.6: (a) The depth dependence of the $c(p_e, k_e)$ frequency spectrum for the unforced run, where the value has been multiplied by a factor 1000; (b) Same as (a) for the forced run, with the inertial frequency, 2x and 3x the inertial frequency denoted. (c) The $c(p_e, k_e)$ frequency spectrum for the forced run at three depths. The shaded columns denote the four frequency bands: $0 \leq f \leq 0.05\ \mathrm{h}^{-1}$ (A0), $0.05 \leq f \leq 0.0714\ \mathrm{h}^{-1}$ (A1), $0.1054 \leq f \leq 0.1335\ \mathrm{h}^{-1}$ (A2) and $0.1624 \leq f \leq 0.1938\ \mathrm{h}^{-1}$ (A3), which represent the subinertial frequency part and three multiple of inertial frequency if_0 ($i = 1, 2, 3$), respectively.

To visualize the variability of $c(p_e, k_e)$ in different frequency ranges, we applied a band-pass filter to separate $c(p_e, k_e)$ into the four frequency bands, as shaded in Figure 3.6c, i.e., $0 \leq f \leq 0.05\ \mathrm{h}^{-1}$ (subinertial frequency range, A0), $0.05 \leq f \leq 0.0714\ \mathrm{h}^{-1}$ (inertial frequency range, A1), $0.1054 \leq f \leq 0.1335\ \mathrm{h}^{-1}$ (2x inertial frequency range, A2) and $0.1624 \leq f \leq 0.1938\ \mathrm{h}^{-1}$ (3x inertial frequency range, A3).

We start by looking at a snapshot of the horizontal distribution of $c(p_e, k_e)$ at the depth 37.5 m within different frequency bands (Figure 3.7). The pattern and magnitude of

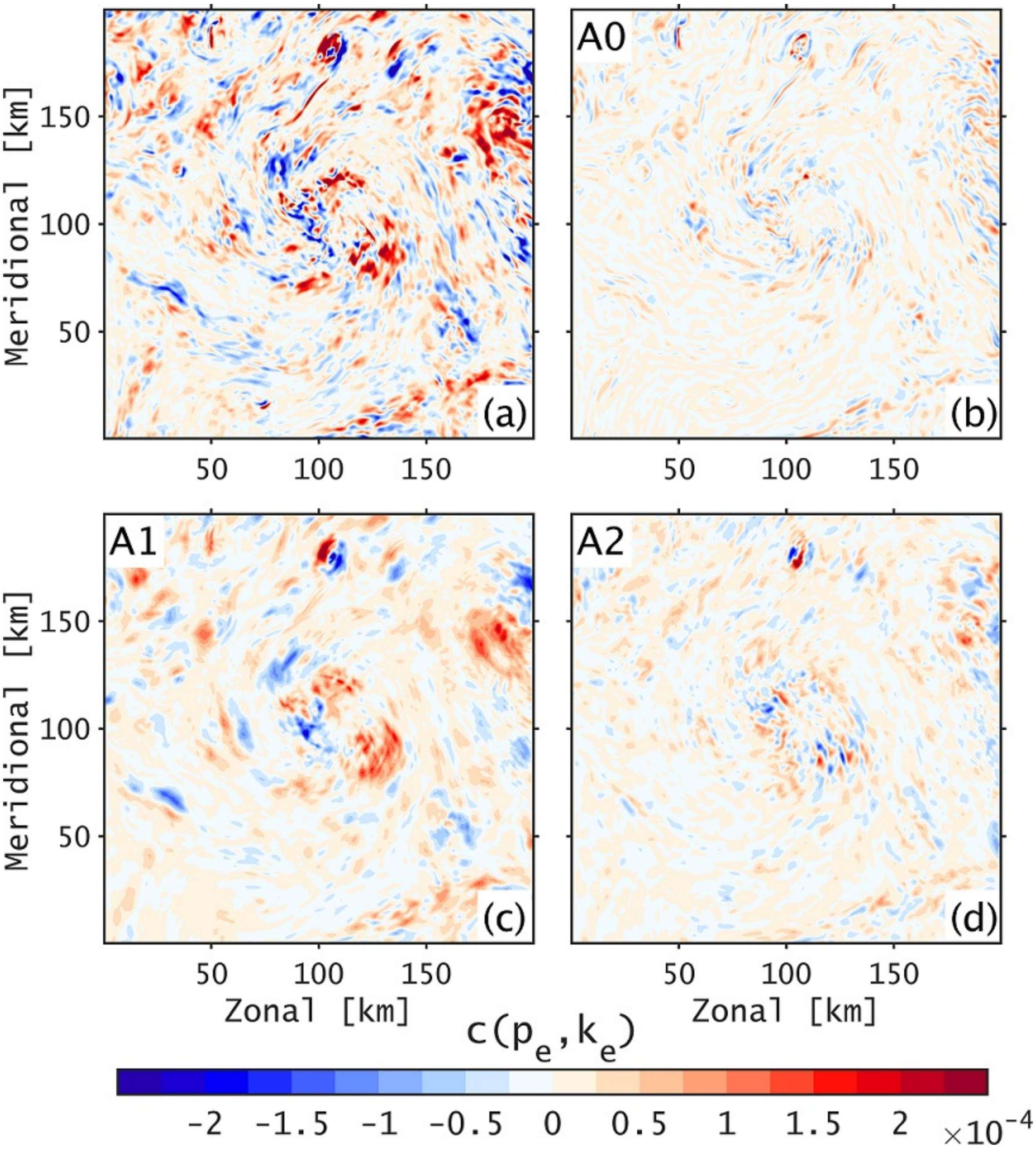

Figure 3.7: Snapshot of $c(p_e, k_e)$ within different frequency ranges at T = 37.5 day, depth = 37.5 m (wind run). (a) $c(p_e, k_e)$ in full frequency range; (b) $c(p_e, k_e)$ filtered within frequency band A0; (c) $c(p_e, k_e)$ filtered within frequency band A1; (d) $c(p_e, k_e)$ filtered within frequency band A2. The units are W m^{-3}.

the inertial frequency part (A1) (Figure 3.7c) is most similar to the total pattern (Figure 3.7a). By contrast, the subinertial frequency part (A0) only accounts for a small portion to the total (Figure 3.7b). The contribution from the 2x inertial frequency part (A2) is between the quantity from A0 and A1 in this snapshot (Figure 3.7d). The $c(p_e, k_e)$ within the 3x frequency range (A3) is smaller than that in A2 and thus not shown. Actually, the $c(p_e, k_e)$ within A2 could be larger than that within A1 in some deeper layers but generally the inertial frequency motions dominate most of $c(p_e, k_e)$.

Next we move to the time-depth dependence of the layer integrated $c(p_e, k_e)$. We present the variables over a period including one wind event (Figure 3.8). Again, the depth-time dependence of $c(p_e, k_e)$ over the total frequency range (Figure 3.8a) is highly consistent with that within the inertial frequency range (Figure 3.8c). In addition, the $c(p_e, k_e)$ introduced by inertial and 2x inertial frequency motions shows a vertically uniform shape (Figure 3.8c, Figure 3.8d). Such vertical coherency and the oscillating nature is not so pronounced in the subinertial range (Figure 3.8b). Noteworthy, the $c(p_e, k_e)$ governed by superinertial motions penetrate deeper than that by inertial motions and the superinertial signal is absent in the mixed layer, whereas the inertial signal is enhanced within the mixed layer.

On the other hand, the subinertial frequency motions extracted p_e to k_e only at the top tens of meters, below which k_e was always converted to p_e. Interestingly, the wind event dramatically excited the surface baroclinic instability induced by the subinertial motions, but such excitation only lasted for a short period (Figure 3.8b).

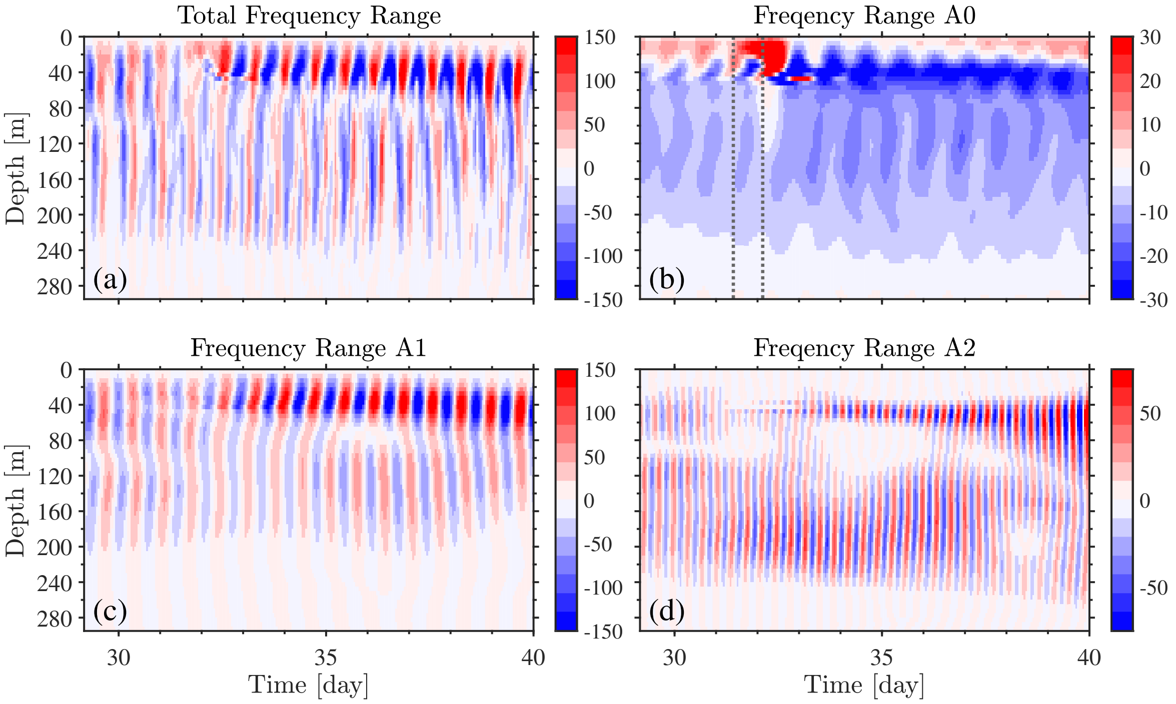

Figure 3.8: The depth-time dependence of the layer integrated $c(p_e, k_e)$ over a selected region ($0 \leq x \leq 200$ km , $0 \leq y \leq 200$ km): (a) The original total frequency range; (b) The low frequency part A0; (c) Same as (b) but for the inertial frequency part A1; (d) Same as (b) but for the 2x inertial frequency part A2. The period between the two dashed black lines in (b) corresponds to the wind event forcing time. The units are KW m^{-1}.

However, if we focus on the time-mean $c(p_e, k_e)$, the inertial and superinertial parts were close to vanishing, and only the subinertial part remained (Figure 3.9). Therefore, one can conclude that the inertial motions dominate the transient conversion between

p_e and k_e, while the subinertial motions dominate the mean process.

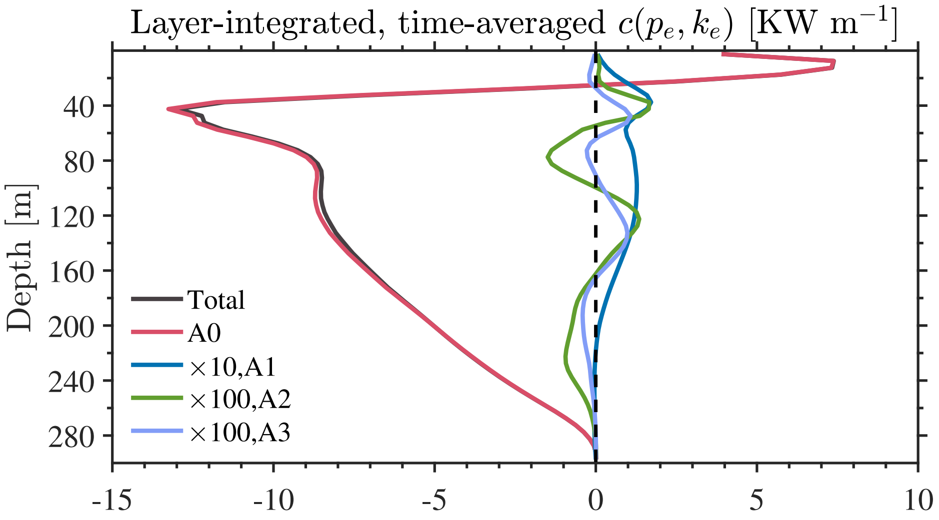

Figure 3.9: Layer-integrated profile of $c(p_e, k_e)$ for the time-averaged field over the full running period and selected region ($0 \leq x \leq 200$ km , $0 \leq y \leq 200$ km). The inertial part has been multiplied by 10 and the superinertial parts have been multiplied by 100.

So far, we have made it clear that the $c(p_e, k_e)$ introduced by subinertial frequency motions is the only part that remained after the time mean. We can turn back now to find out which process leads to that conversion. This is accomplished by concentrating on the subinertial parts of the anomaly of vertical velocity (w') and density (ρ'), which determine $c(p_e, k_e)$ (Equation 3.9). They were filtered with the same filter as $c(p_e, k_e)$ and Figure 3.10 shows their depth-time dependence within the subinertial frequency band.

The pattern of w' is similar to that of $c(p_e, k_e)$ within the same frequency band except for the opposite sign (Figure 3.10a,Figure 3.8b). The wind event significantly re-stratified the mixed layer: the dense anomaly came to the surface and a light anomaly came to deeper depths (Figure 3.10b). Therefore the $c(p_e, k_e)$ in the mixed layer induced by the wind event was due to the upwelling of dense water anomaly.

The wavenumber spectrum of $c(p_e, k_e)$ (Figure 3.11) was calculated along the zonal direction and then averaged over the meridional and time dimension. First, the magnitude of $c(p_e, k_e)$ wavenumber spectrum increased approximately three to four orders of magnitude over scales larger than 10 km due to the wind forcing (Figure 3.11b,Figure 3.11c). Besides, the $c(p_e, k_e)$ enhancement over a scale of 5-10 km was additionally promoted in the wind run, which is a piece of evidence that the wind event increased the submesoscale activity.

Second, a strong correlation between $c(p_e, k_e)$ and the depth of the base of the mixed layer was confirmed by the comparison between the density (layer- and time- mean) vertical gradient ($\rho_z = \partial\rho/\partial z$) and the $c(p_e, k_e)$ wavenumber spectra. The maximum of ρ_z indicated the position of the base of the mixed layer, which increased from 30

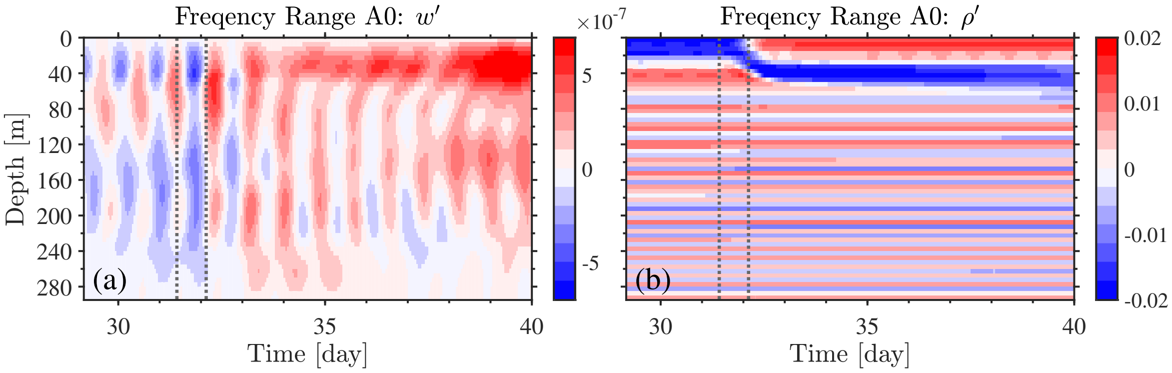

Figure 3.10: (a) Anomaly of vertical velocity within the subinertial frequency band (in m s^{-1}). (b) Anomaly of density within the subinertial frequency band (in kg m^{-3}).

m to 50 m due to wind (Figure 3.11a). Both runs show a perfect consistency between the depth of $c(p_e, k_e)$ peak in the wavenumber space and that of the base of the mixed layer, where the conversion between p_e and k_e is most active.

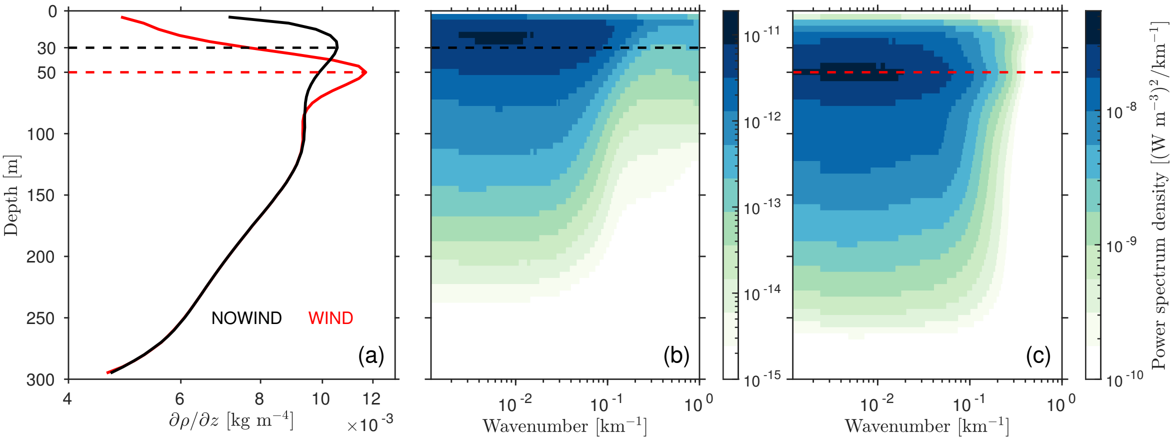

Figure 3.11: (a) Layer-averaged, time-mean density vertical gradient for the forced run (solid red line) and unforced run (solid black line). Dashed lines indicate the corresponding depth of the mixed layer base. (b) Wavenumber spectrum for $c(p_e, k_e)$ of the unforced run with the dashed line representing the corresponding mixed layer depth in (a). (c) Same as (b) but of the forced run. Both have been averaged over all sampling points after performing the spectral analysis.

To summarise, the enhanced submesoscale eddy and filament activity due to wind burst events re-stratified the mixed layer. The wind-induced turbulence at the base of the mixed layer promoted its deepening and therefore dramatically increased the conversion efficiency between p_e and k_e. The inertial motions dominated the transient conversion, whereas the subinertial motions dominated the mean conversion. In the forced run, the dominance of $c(p_e, k_e)$ in the mixed layer was mainly due to the upwelling of denser water, i.e., by upward entrainment into the mixed layer.

3.3.3 Conversion between k_m and k_e

We turn attention to the conversion term $c(k_m, k_e)$. From a time-averaged point of view, the eddy kinetic energy was converted to the mean kinetic energy in all layers in the no wind run, with decreasing efficiency with depth. In the wind-forced run, however, $c(k_m, k_e)$ was close to that in the no wind run in the surface layers but increased with depth until reaching the base of the mixed layer, with reversing its sign in between (Figure 3.12c). On the other hand, the transient $c(k_m, k_e)$ oscillated with time in the forced run (Figure 3.12b) while it kept negative in the unforced run (Figure 3.12a).

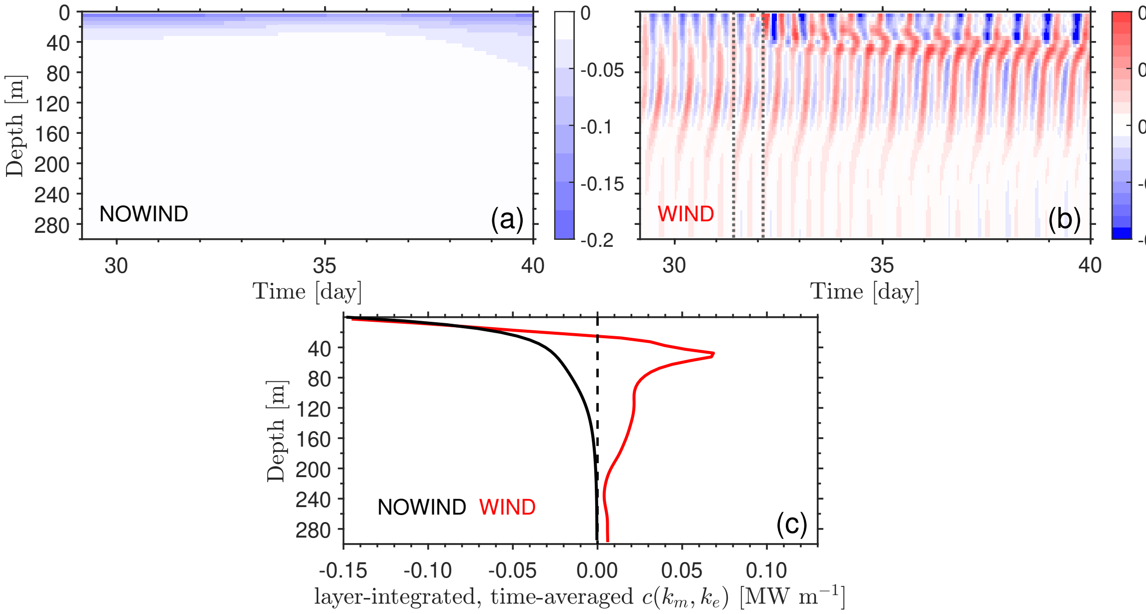

Figure 3.12: (a) Depth-time dependence of layered integrated $c(k_m, k_e)$ in the unforced run. (b) The same as (a) but in the forced run. The period is presented for the time around one wind event (between the two vertical dashed lines). (c) Layer-integrated, time-averaged $c(k_m, k_e)$ profile for the unforced (black line) and forced (red line) runs.

In the frequency space, the conversion between k_m and k_e was energized by the wind-induced inertial and superinertial motions (Figure 3.13). Those motions dominated the conversion from the surface down to the bottom, with decreasing magnitude with depth. The subinertial part was also enhanced in magnitude by the wind.

As above, we implemented a band-pass filter of $c(k_m, k_e)$ to obtain its subinertial, inertial and superinertial components. The total frequency pattern seems to be the sum of inertial and 2x inertial parts (Figure 3.14). The inertial part dominated before the wind event (a result of the previous wind event), and after the wind event, the 2x inertial part dominated. For the subinertial part, k_m was converted to k_e at the base of the mixed layer one day after the forcing stopped, revealing the barotropic instability growing there (Figure 3.14b).

However, the mean of the inertial and 2x inertial parts of $c(k_m, k_e)$ was small compared to that of the subinertial part, which overlapped the total quantity perfectly (Fig-

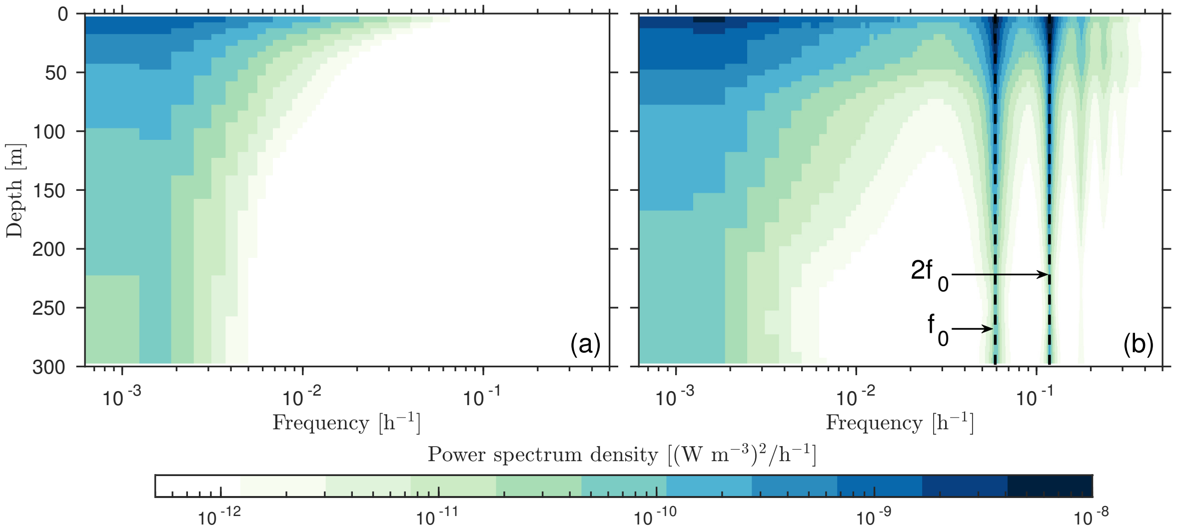

Figure 3.13: (a) The frequency spectrum for $c(k_m, k_e)$ of the unforced run; (b) The frequency spectrum for $c(k_m, k_e)$ of the forced run, with inertial frequency and 2x inertial frequency position denoted.

ure 3.15). Thus we conclude that $c(k_m, k_e)$ was transiently dominated by the inertial and 2x inertial motions, but the subinertial motions dominated on the mean.

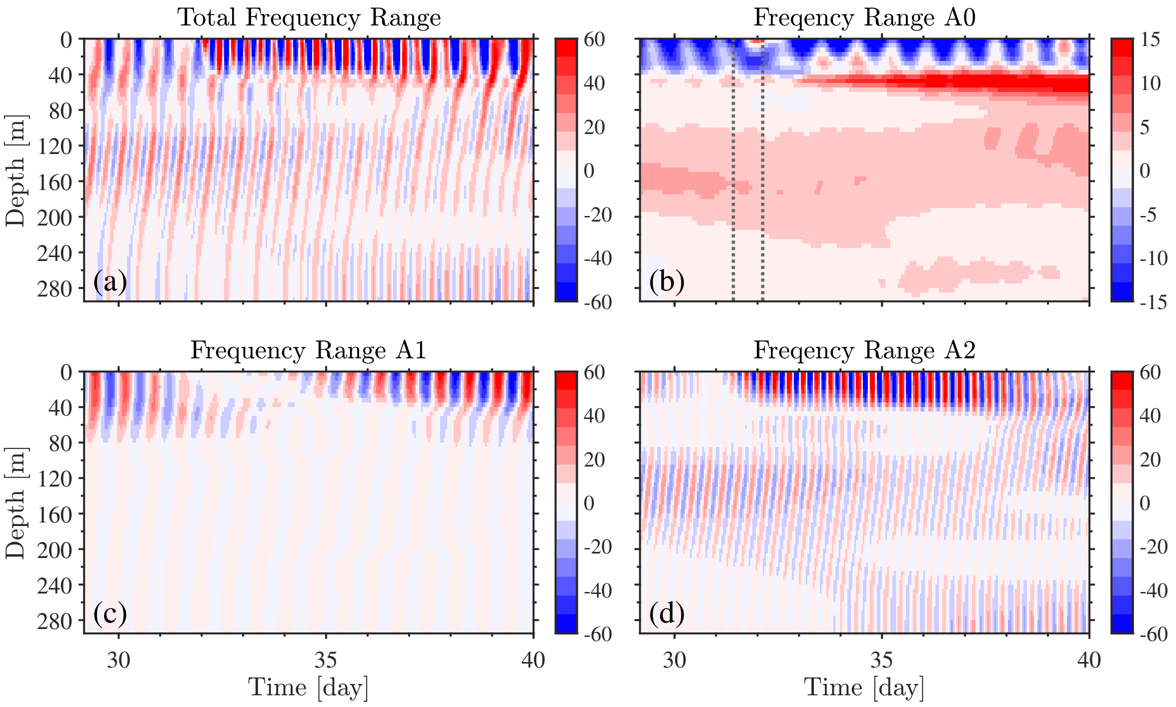

Figure 3.14: Same as Figure 3.8 but for $c(k_m, k_e)$ (units are KW m^{-1}.

We seek to find which dynamic processes changed $c(k_m, k_e)$ around the base of the mixed layer and below by wind events by expanding the calculation of $c(k_m, k_e)$ as follows:

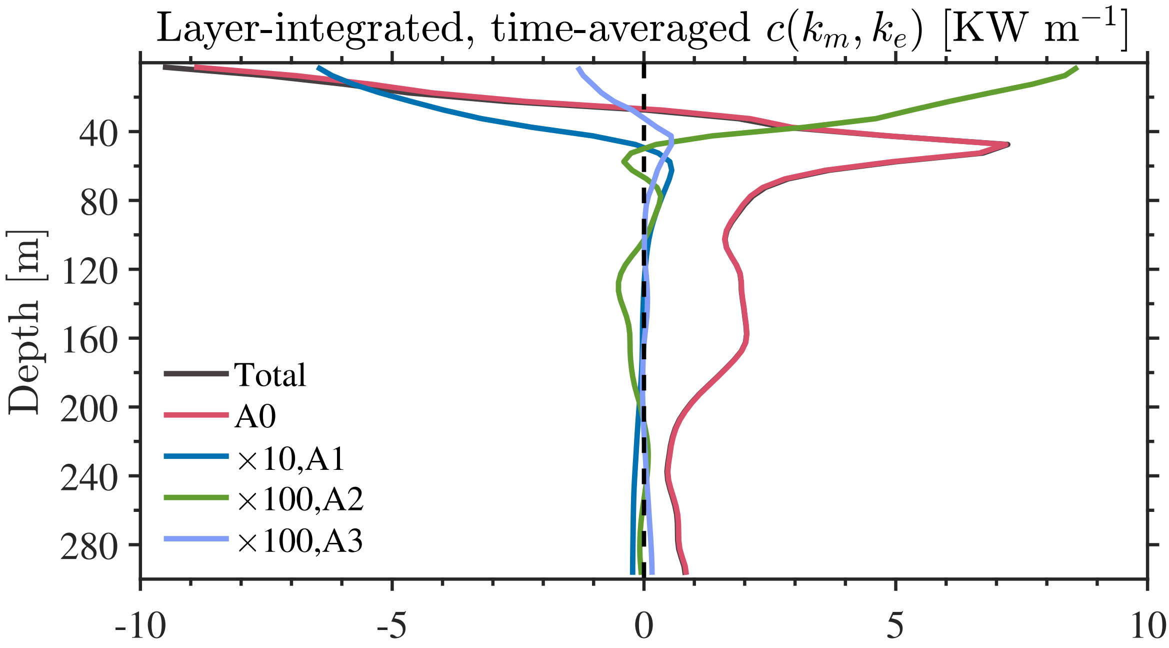

Figure 3.15: The same as Figure 3.9 but for $c(k_m, k_e)$. The black line and red line almost overlap.

$$
\begin{aligned}
c(k_m, k_e) &= -\rho_0 u' \mathbf{u}' \cdot \nabla \bar{u} - \rho_0 v' \mathbf{u}' \cdot \nabla \bar{v} \\
&= \underbrace{-\rho_0 u' u' \bar{u}_x}_{\text{term 1}} \underbrace{-\rho_0 u' v' \bar{u}_y}_{\text{term 2}} \underbrace{-\rho_0 u' w' \bar{u}_z}_{\text{term 3}} \underbrace{-\rho_0 v' u' \bar{v}_x}_{\text{term 4}} \underbrace{-\rho_0 v' v' \bar{v}_y}_{\text{term 5}} \underbrace{-\rho_0 v' w' \bar{v}_z}_{\text{term 6}} \\
&= \underbrace{-\rho_0 (u' u' \bar{u}_x + v' v' \bar{v}_y)}_{\text{term 1+term 5}} \underbrace{-\rho_0 u' v' (\bar{u}_y + \bar{v}_x)}_{\text{term 2+term 4}} \underbrace{-\rho_0 w' (u' \bar{u}_z + v' \bar{v}_z)}_{\text{term 3+term 6}} \qquad (3.10)
\end{aligned}
$$

where all symbols are as defined above.

As we already pointed out, the subinertial part dominates the time mean processes; therefore, we only focus on the subinertial part of those terms. Layer integrated terms of $c(k_m, k_e)$ reveal that the vertical velocity related terms, i.e., term3 and term6 are together responsible for the reverse sign of $c(k_m, k_e)$ around the base of the mixed layer and below (Figure 3.16), ultimately leading to a reversed converting direction in the total integrated $C(K_m, K_e)$ (see Figure 3.3).

On the other hand, in the wavenumber space, the conversion between k_m and k_e was most active in the surface and kept meaningful in the mixed layer (Figure 3.17). The wind event energised the process about 100 times in the mixed layer but less enhancement below. Also, the wind event additionally excited the conversion with scales of 7-10 km in the mixed layer.

To summarise, the conversion between k_m and k_e was mainly active in the mixed layer while the wind forcing significantly influenced it. In the mixed layer, the wind event

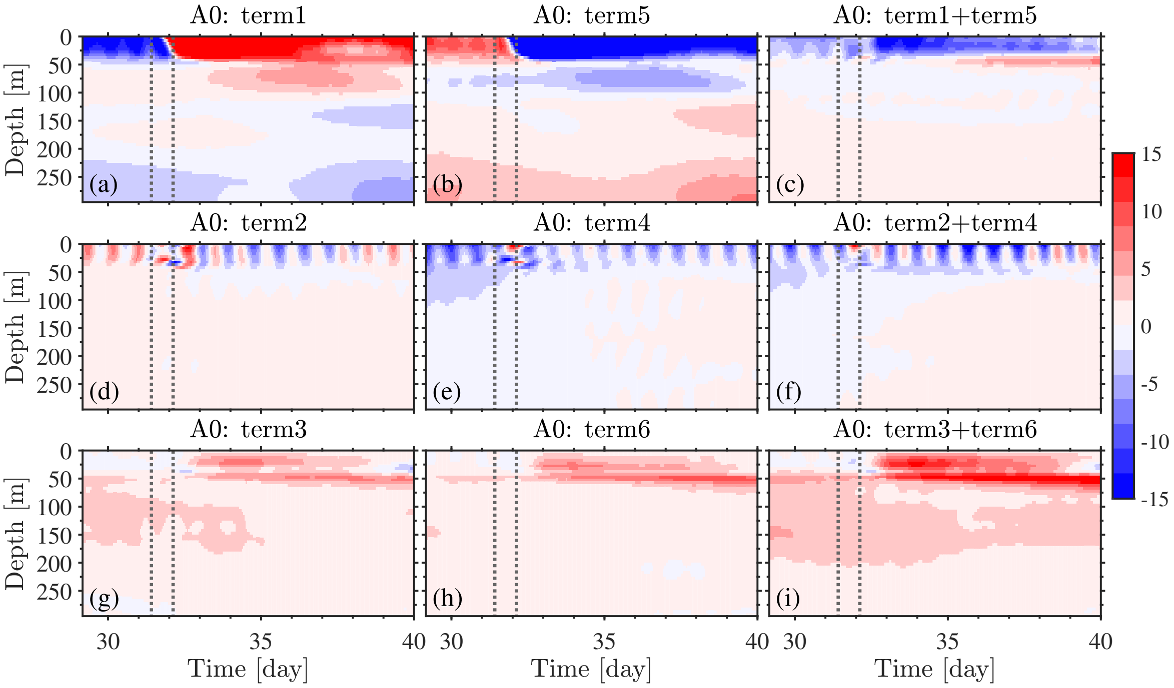

Figure 3.16: Layer integrated terms of $c(k_m, k_e)$ indicated in Equation 3.10 within the subinertial frequency range A0 (units are KW m^{-1}.

energised the process by enhanced submesoscale motions; at the base of the mixed layer, the wind excited strong barotropic instability by subinertial motions.

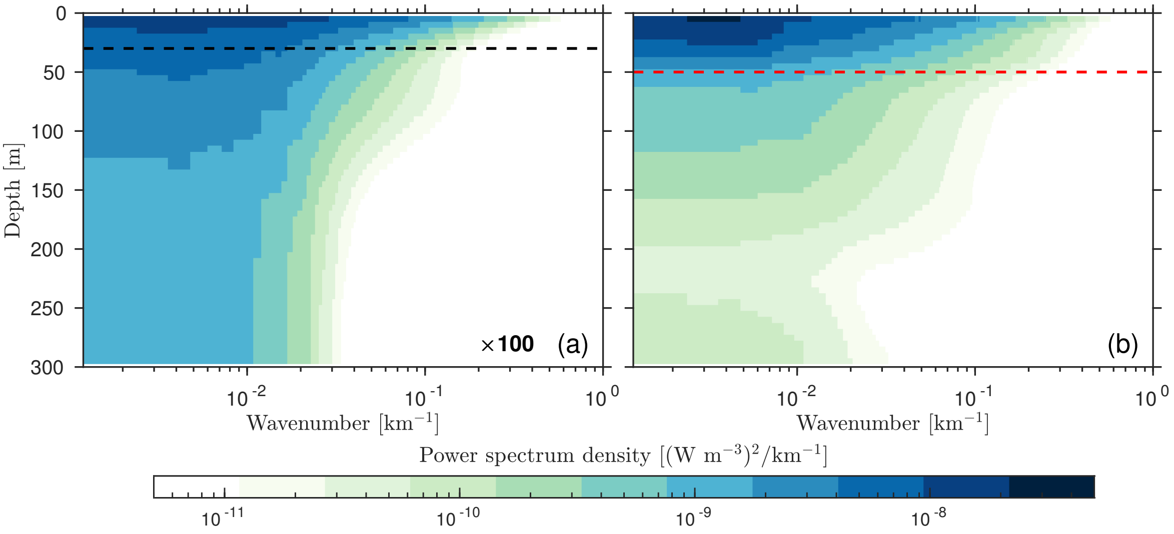

Figure 3.17: (a) Wavenumber spectrum of $c(k_m, k_e)$ for the unforced run (values multiplied by 100). (b) Wavenumber spectrum of $c(k_m, k_e)$ for the forced run. Horizontal dashed lines in both panels indicate the corresponding position of the base of the mixed layer as depicted in Figure 3.11a.

3.4 Asymmetry in kinetic energy conversion by eddies

Three different flow components, namely anticyclonic eddies, cyclonic eddies and filaments, were closely investigated to understand their role in the kinetic energy conversion.

3.4.1 Components separation

Existing eddy detecting strategies include geometry-based methods, flow-dependent methods and hybrid methods (Wang et al., 2015). Those methods mainly address identifying mesoscale eddies in an eddy-resolving resolution background. When the resolution increases to resolve submesoscales, problems arise, including the difficulty of separating much smaller vortices from a more complex flow background.

Our goal is to study the different behaviour in kinetic energy conversion by cyclonic and anticyclonic eddies, regardless of the eddy size or shape. We propose some criteria based on a vorticity detection technique to simplify the question of flow split into the three components. Note that such criteria do not ensure the eddy structure; they only roughly denote those model grid points satisfying the following conditions, which are attributed to some specific component:

1. if $\mathrm{OW} < 0$ and $\zeta > 0$, point belongs to a cyclonic eddy;
2. if $\mathrm{OW} < 0$ and $\zeta < 0$, point belongs to an anticyclonic eddy;
3. otherwise, point belongs to an elongated filament.

where OW is the abbreviation of Okubo-Weiss parameter (Chelton et al., 2011), which is defined as

$$\mathrm{OW} = \mathrm{Ss}^2 + \mathrm{Sn}^2 - \zeta^2, \tag{3.11}$$

with Ss and Sn as defined in Equation 3.2 and Equation 3.3.

A typical distribution of the relative vorticity in the three components reveals that the splitting strategy works reasonably well (Figure 3.18). Although some strong filaments surrounding the eddies are identified as part of eddies, generally, the entire eddy population was extracted from the background flow field, which is good enough for our purpose.

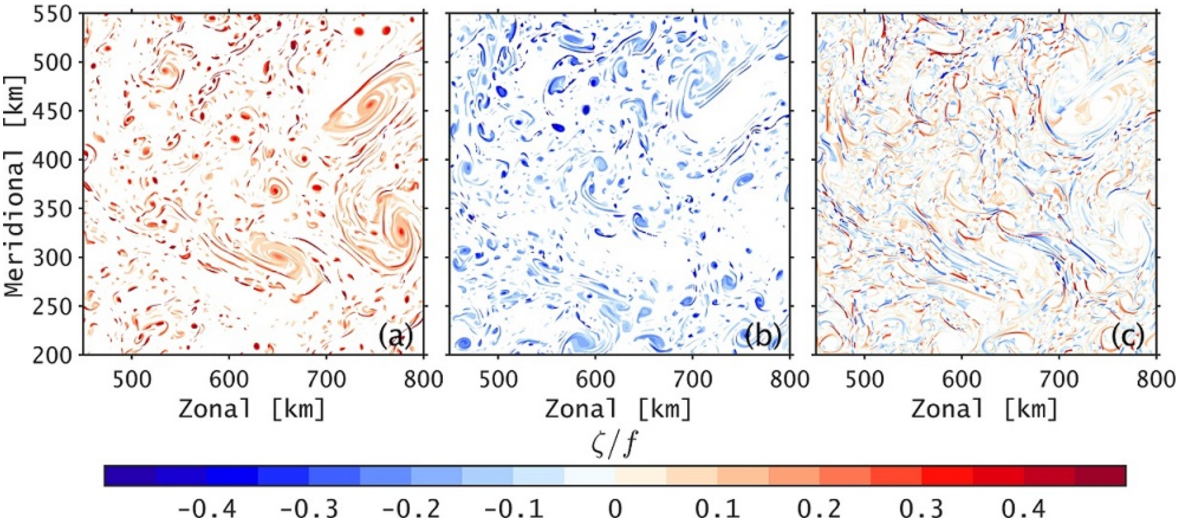

Figure 3.18: Snapshots of normalized relative vorticity, ζ/f, at T = 20 days at the surface (no forcing run): (a) cyclonic eddies, (b) anticyclonic eddies and (c) filaments.

3.4.2 Eddies and filaments in the unforced run

We applied the above criteria to the unforced simulation and found some significant differences between eddies and filaments regarding their ability to contain K_e and P_e as well as their roles in kinetic energy conversion (Table 3.2).

	Area %	K_e [J/m^3]	P_e [J/m^3]	$c(p_e, k_e)$ [W/m^3]	$c(k_m, k_e)$ [W/m^3]
cyclonic eddies	18.70	1.26	1.09	1.27×10^{-7}	-1.36×10^{-7}
anticyclonic eddies	20.61	0.84	0.66	9.69×10^{-8}	-7.43×10^{-8}
filaments	60.69	0.94	0.46	1.40×10^{-7}	-8.93×10^{-8}

Table 3.2: Average percentage of occupation and average quantities contained in the three flow components over the upper 50 m (no forcing run).

During the whole integration period, filaments reigned in the top ten layers and occupied about 60% of the water volume, while cyclonic and anticyclonic eddies both occupied around 20%.

On average, however, cyclonic eddies preserved about 50% more K_e than anticyclonic eddies (per unit volume) and 34% more than filaments, revealing cyclonic eddies having a larger capacity to contain K_e. Regarding P_e, cyclonic eddies had approximately 65% more P_e than anticyclonic eddies and 137% more as filaments.

Cyclonic and anticyclonic eddies showed an asymmetry in kinetic energy conversions $c(p_e, k_e)$ and $c(k_m, k_e)$. Cyclonic and anticyclonic eddies mainly convert p_e to k_e in the upper ocean (Figure 3.19), but the $c(p_e, k_e)$ by cyclones was about 30% larger than in anticyclones (Table 3.2), and this is true in almost all levels (Figure 3.19c).

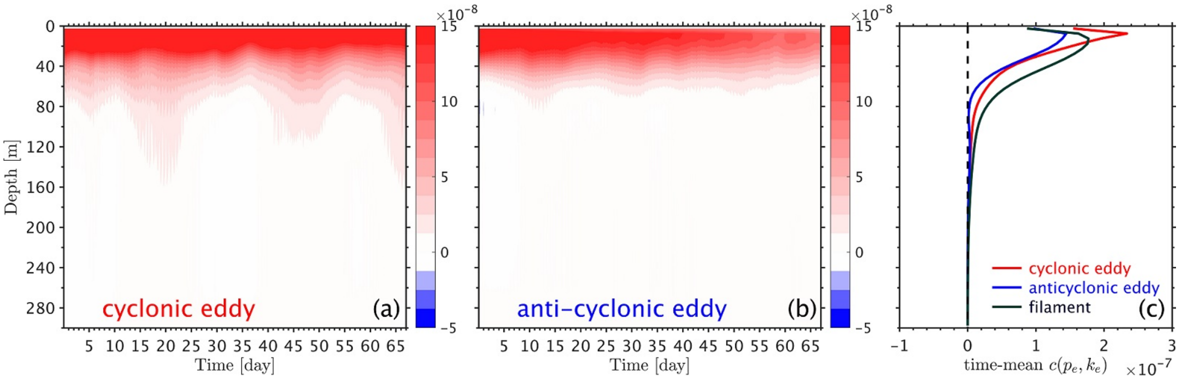

Figure 3.19: (a) Average $c(p_e, k_e)$ among cyclonic eddies on each layer. (b) The same as (a) but for anticyclonic eddies. (c) Time-mean profile for (a) and (b) and also display the profile for filaments (no forcing run). Unit: W/m^3.

Interestingly, the $c(p_e, k_e)$ by filaments was larger than that by anticyclonic eddies in all levels and it was smaller than that by cyclones in the mixed layer (Figure 3.19c).

As for $c(k_m, k_e)$, the conversion efficiency of cyclonic eddies was 83% larger than that of anticyclonic eddies in the top 50m (Table 3.2) but also larger at all depths (Figure 3.20). In addition, the $c(p_e, k_e)$ by anticyclones was similar to that by filaments (Figure 3.20c).

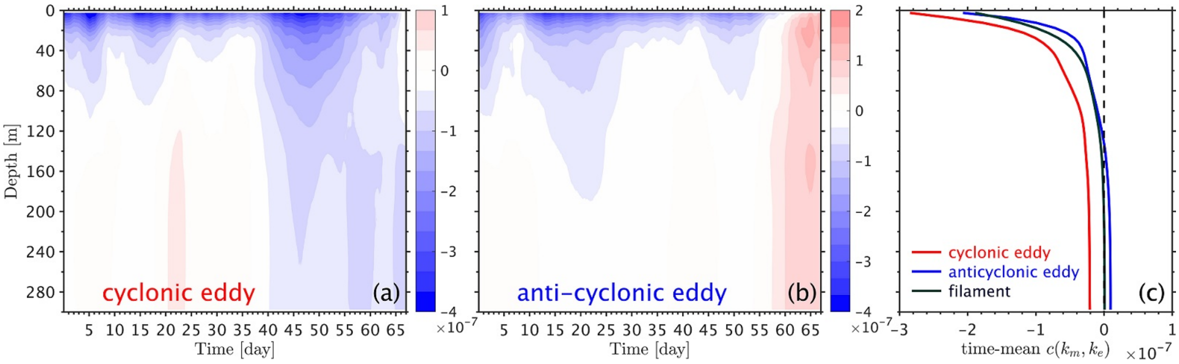

Figure 3.20: (a) Average $c(k_m, k_e)$ in cyclonic eddies (unforced run). (b) Same as (a) but for anticyclonic eddies. (c) Time-mean profile of (a) and (b), also computed for the filaments. Units are W/m^3.

3.4.3 Eddies and filaments in the wind-forced run

Now we turn attention to the wind forced case and check whether the wind forcing impacts the above asymmetry in kinetic energy conversion by eddies (Table 3.3).

Like in the unforced case, filaments occupied most of the water volume (~70%), and cyclonic and anticyclonic eddies nearly equally share the remaining domain. In the forced run, the three components have similar capacity to contain K_e and P_e (Table 3.3). However, they presented different behavior regarding $c(p_e, k_e)$ and $c(k_m, k_e)$.

	Area %	K_e [J/m^3]	P_e [J/m^3]	$c(p_e, k_e)$ [W/m^3]	$c(k_m, k_e)$ [W/m^3]
cyclonic eddies	14.41	5.00	1.26	1.64×10^{-7}	8.06×10^{-8}
anticyclonic eddies	16.08	6.31	1.08	4.41×10^{-6}	7.55×10^{-8}
filaments	69.51	5.69	0.93	-1.07×10^{-6}	-1.58×10^{-8}

Table 3.3: Average percentage of occupation and average quantities contained in three components over the upper 100 m (forced run).

In general, anticyclonic eddies were approximately 27 times more efficient in converting p_e to k_e than cyclonic eddies in the upper 100 m (Table 3.3). Additionally, if we look at the temporal-depth variations, the two types of eddies presented an opposite behavior (Figure 3.21): while the anticyclones converted p_e to k_e, the cyclones converted k_e to p_e. But obviously, the absolute conversion efficiency of anticyclones was bigger than the cyclones, which is the opposite behaviour compared to the unforced case.

Although the time average $c(k_m, k_e)$ efficiency by cyclonic and anticyclonic eddies were about the same (Table 3.3), $c(k_m, k_e)$ in cyclonic and anticyclonic eddies also showed an opposite temporal-depth distribution (Figure 3.22).

The comparison between the wind forced and the unforced run comes to the result that anticyclonic eddies were dramatically energised. This is connected to the rotating direction of the wind stress. Our wind stress forcing was designed to rotate clockwise with an inertial period; it could energise the anticyclonic eddies on the surface and gradually into the mixed layer. The enhanced anticyclonic eddies dramatically promoted the $c(p_e, k_e)$ and finally led to 27 times more efficient than cyclonic eddies. We could expect that if the wind stress forcing was anti-clockwise rotating, there would be an opposite result: cyclonic eddies were greatly enhanced instead of anticyclonic eddies. But this needs to be verified.

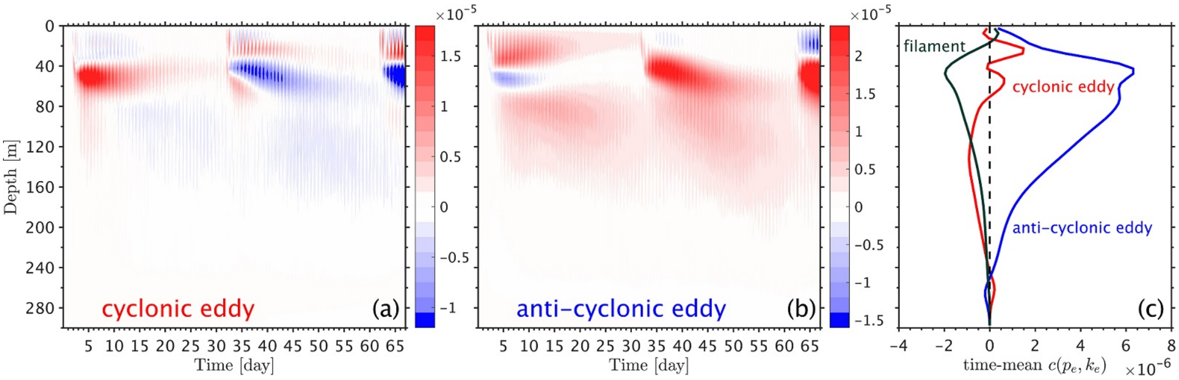

Figure 3.21: (a) Average $c(p_e, k_e)$ in cyclonic eddies in the wind-forced run. (b) Same as (a) but for anticyclonic eddies. (c) Time-mean profile of (a) and (b) with the corresponding profile for filaments showed. Units are W/m^3.

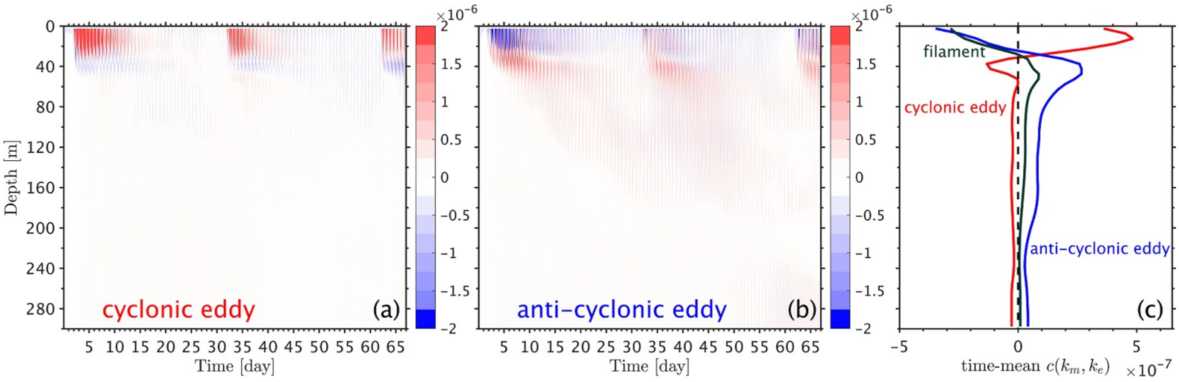

Figure 3.22: (a) Average $c(k_m, k_e)$ in cyclonic eddies in the wind-forced run. (b) Same as (a) but for anticyclonic eddies. (c) Time-mean profile of (a) and (b) with the corresponding profile for filaments showed. Units are W/m^3.

3.5 Summary and discussion

Our purpose was to understand and quantify the wind forcing of kinetic energy conversion in a surface-intensified submesoscale flow.

The increase of K_e in the second wind event is smaller than in the first wind event. We believe that this is due to the increased ”roughness” of the surface currents during the second wind event. This agrees with the result by Hughes and Wilson (2008), who studied the work done on the geostrophic circulation by wind stress and found that the small scales in the currents are crucial, smoother currents leading to more wind power input.

Niwa and Hibiya (1997) studied with a numerical model the generation of large-scale internal waves by a hurricane propagating eastward. They found that the spectral value at $\omega \approx 2f$ becomes larger than that of the near-inertial waves in the area away from the hurricane track. Therefore the low-vertical-mode superinertial waves are believed to play significant roles in supplying energy to the internal wave field in the deep ocean by promoting the energy dispersion from the mixed layer. Our results corroborate their conclusions. In the wind forced run, the K_e spectrum of the superinertial frequency components was larger than that of the inertial component in the deep ocean. This is more likely the case when the layer is deep, where the area is more distant from the surface wind stress.

Additionally, we showed that both inertial and superinertial motions dominate the transient kinetic energy conversion, while the subinertial motions dominate in the time-mean perspective.

Previously, asymmetry study of eddies mainly involved their vorticity distributions (Shcherbina et al., 2013; Wang and Jordi, 2011). We have here investigated the asymmetric characteristic of kinetic energy conversion by eddies. As we found above, the cyclonic eddies have different capacities to contain K_e and different abilities to convert K_e to P_e or K_m. And such asymmetry changed with the external forcing. The wind stress, in our case, magnified such asymmetry and led to an opposite behaviour regarding the kinetic energy conversion by cyclonic and anticyclonic eddies.

In summary, the study presented in this chapter answered the following questions:

1. What is the impact of resolved submesoscale motions on the kinetic energy conversion?

   The submesoscale motions promoted the efficiency of kinetic energy conversion, both for $c(p_e, k_e)$ and $c(k_m, k_e)$. In addition, the intensified submesoscale motions brought about by the wind stress forcing changed the time-mean direction of $C(P_e, K_e)$ and $C(K_m, K_e)$ by modifying the baroclinic and barotropic instability occurrence, respectively.

2. Where are the energy conversion terms intensified?

   Both terms $c(p_e, k_e)$ and $c(k_m, k_e)$ were surface intensified, the former peaking in the mixed layer and the latter at the surface.

3. How do the conversion terms change in the presence of wind stress forcing?

   The wind forcing greatly enhanced the efficiency of $c(p_e, k_e)$ and $c(k_m, k_e)$, leading to an opposite behaviour regarding the cyclone and anticyclone asymmetry when compared to the absence of wind.

4. What is the difference between cyclones and anticyclones in terms of kinetic energy conversion? Does this change when external forcing is imposed?

   In the unforced case, the cyclonic eddies contained more K_e and P_e and were more efficient in converting kinetic energy than the anticyclones. The external anticyclonic wind stress forcing dramatically changed such relation, with anticyclones accumulating more K_e and being more active in converting p_e to k_e.

The numerical simulations were highly idealised, neglecting the variation of seabed topography and buoyancy flux on the surface. Future work is expected to investigate the influence of buoyancy and topography.

Chapter 4

Constraining the submesoscale flow in an eddy-resolving adjoint-based data assimilation model[1]

4.1 Adjoint model set-up

In the 4DVAR data assimilation, a cost function measuring the distance between the model simulation and the observations is minimized in an iterative process in order to bring the model into consistency with the observations. To this end, the sensitivity of the model-data misfit cost function to a few control variables (in our case, the initial potential temperature and salinity condition) is computed to determine the adjustments of the control variables needed to bring the cost down. In this process, the adjoint of the tangent linear version of the nonlinear model is integrated backwards in time to find the gradients of the cost function. As stated in Section 2, the adjoint of the MITgcm as generated by TAF(Giering and Kaminski, 1998) was used. Once the corrections to the control variables are determined via a gradient descent algorithm, a new forward simulation is conducted, which lies closer to the observations in a global sense. A reasonable degree of convergence (meaning the proximity of the cost function minimum) is reached after a few iterations of the described iterative process.

Our experiments consisted of unconstrained forward model runs, namely a ”truth” and a ”first guess” run and several constrained adjoint model runs performing data assimilation.

---

[1] Li S., N. Serra, C. Liu, A. Köhl, G. Lyu, W. Zhang and D. Stammer (2021): Constraining the submesoscale flow in an eddy-resolving adjoint-based data assimilation model. *To be submitted.*

4.1.1 ”truth” state and ”observations”

After the spin-up was completed, the initial condition for the ”truth” simulation was chosen from a snapshot of the submesoscale run analyzed in Section 3. For computational reasons, we took only part of the domain (a 180 km × 180 km × 300 m box, with original resolution), speeding up the computing-intensive calculations. The chosen area presents submesoscale filaments surrounding a surface-intensified cyclonic eddy (Figure 4.1). The submesoscale variability is mostly confined to the upper 50-100m of the water column, with the interior showing a tendency for larger (mesoscale) scales.

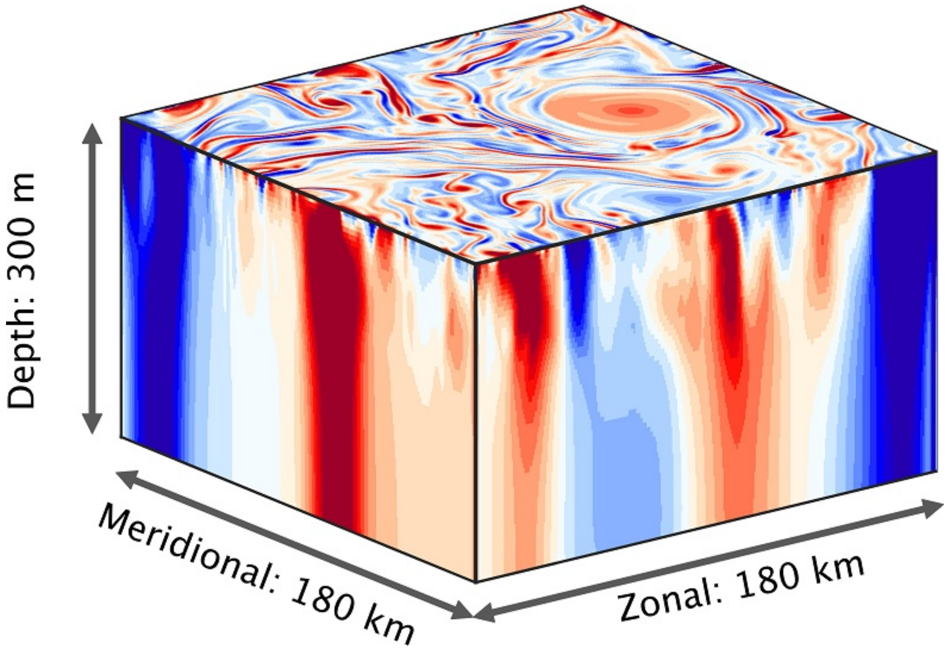

Figure 4.1: Adjoint model domain, as a subset of the original model. Shown is a snapshot of horizontal relative vorticity normalized by the planetary vorticity (ζ/f) corresponding to the ”truth” run initial condition.

The forward model was integrated for 30 days to generate the ”truth” state starting from those potential temperature and salinity initial conditions. This ”truth” run is used to evaluate further ahead of the assimilation results and provide ”observations” for the assimilation experiments.

4.1.2 ”First-guess” initial condition

Our purpose is to constrain the submesoscale flow; we eliminate all submesoscale features (with scales less than 10 km) from the 3D initial conditions and then try to recover those exact signals by assimilating surface observations. Therefore, we obtained the initial state for the ”first-guess” by applying a spatial smoother to remove all scales smaller than ∼10 km present in the ”truth” initial condition. The spatial smoother is designed as

$$A(i,j) = \frac{1}{(2k+1)^2} \sum_{\substack{m=i-k,\dots,i+k \\ n=j-k,\dots,j+k}} A(m,n) \tag{4.1}$$

where k is the smoother level (if eliminating signals with scales less than 10 km, then $k = 10$ since, in our case, the horizontal resolution is 500 m). A is the state variable for the initial condition, i.e., zonal velocity (u), meridional velocity (v), temperature (T) and salinity (S). Indices i,j correspond to the horizontal model grid.

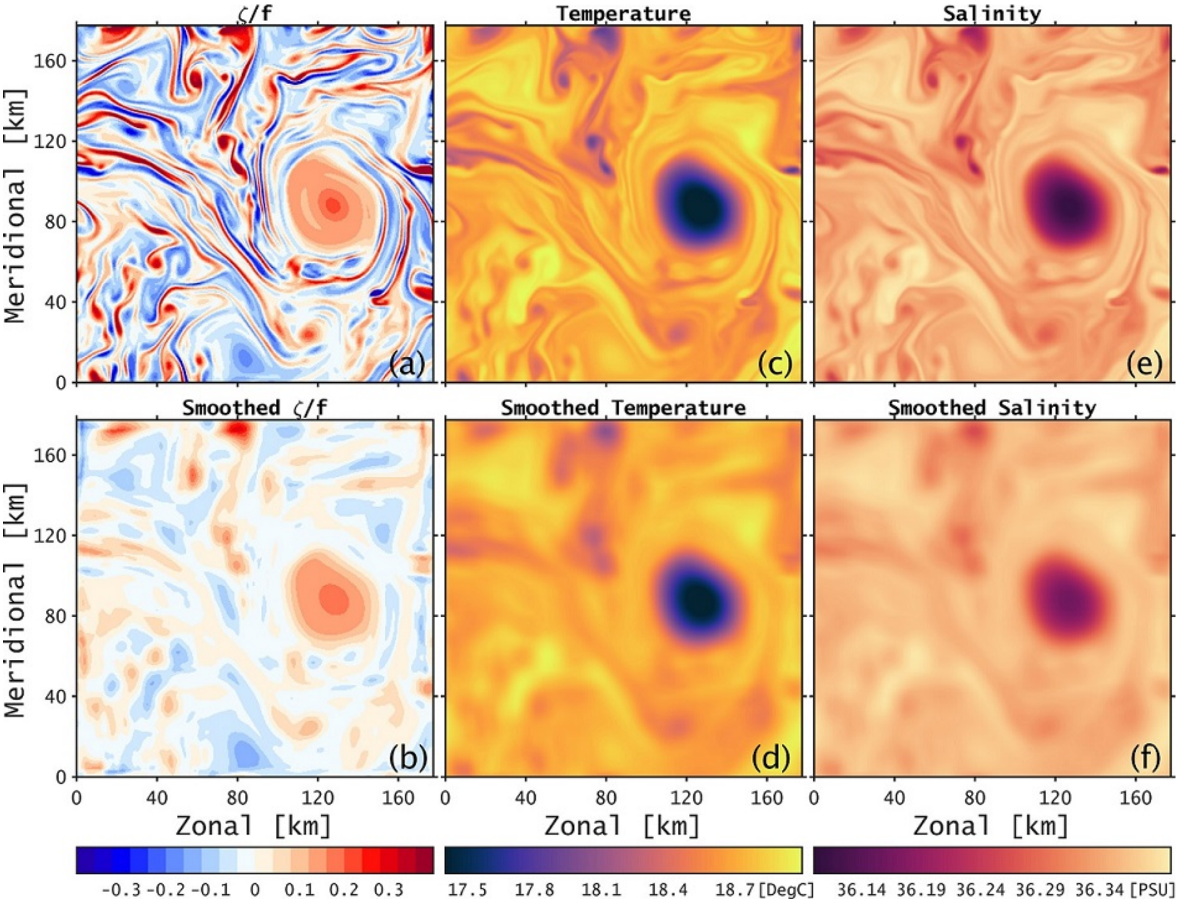

Figure 4.2: Comparison of the surface initial condition before and after smoothing. The above three panels (a,c,e) present the original fields while the bottom three panels (b,d,f) show the smoothed fields: (a,b) relative vorticity normalized by Coriolis parameter (ζ/f), (c,d) temperature and (e,f) salinity.

The comparison between the flow, temperature and salinity fields before and after smoothing shows that the smoother works well in removing nearly all submesoscale filaments (Figure 4.2). From the spectral view, the smoother almost removed all motions with wavelength less than ∼10 km (Figure 4.3). Additionally, the smoothing process decreased the whole kinetic energy level.

The smoothed fields are used as the model initial conditions also in the following assimilation experiments. Again, our goal is to reproduce the eliminated filaments by

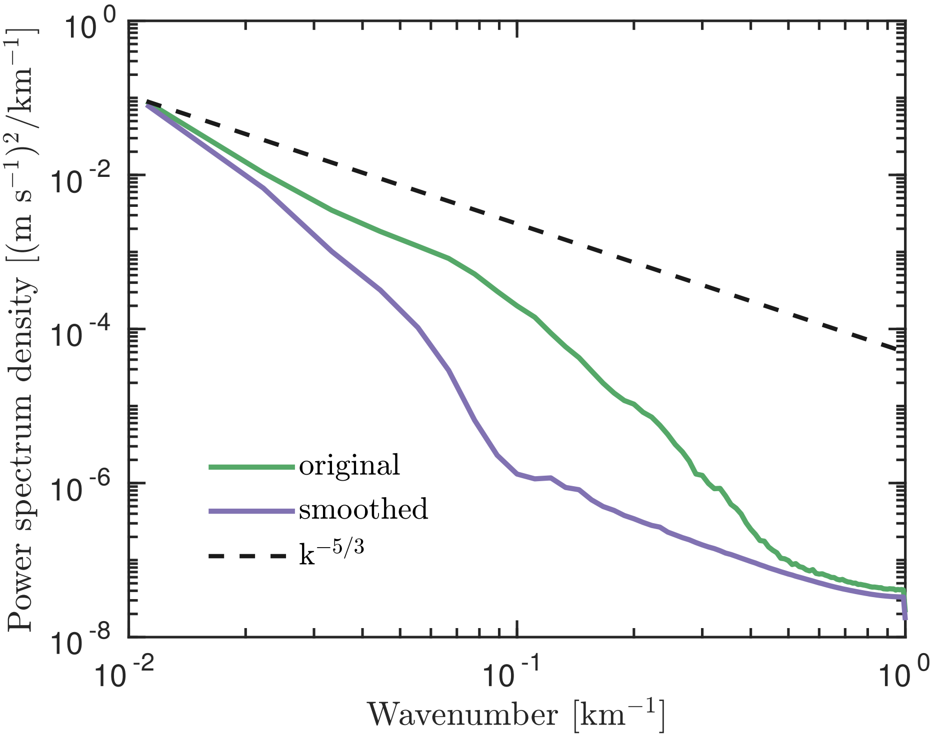

Figure 4.3: Wavenumber spectra of surface zonal velocity with and without smoothing of the initial conditions.

assimilating surface-only ”observations”.

4.1.3 Cost function and control variables

The assimilation results depend on many factors, including which observations are assimilated, how accurate the observations are (i.e., the observation error), and how long the assimilation time window is.

We first need to design the cost function. Together with the contribution from the observation-model misfit, we choose initial temperature (*temp*0) and initial salinity (*salt*0) to also contribute with penalties to the cost function. Those initial conditions are the control variables, meaning that in the iterative process, those variables will be corrected in such a way that and until when the cost function reduces towards a minimum.

We implemented an extra forward experiment starting from a smoothed velocity field but with original temperature and salinity (from the ”true” state). The integration results indicate that the flow field can get close to the ”true” velocity state very soon (in ∼1 day), i.e., the filaments with fine structures could be recovered relatively well (Figure 4.4). This is not surprising since it is due to a geostrophic adjustment process. But it suggests that there might not be a need to take initial velocity as a control variable and that there might not be a need to assimilate velocity observations.

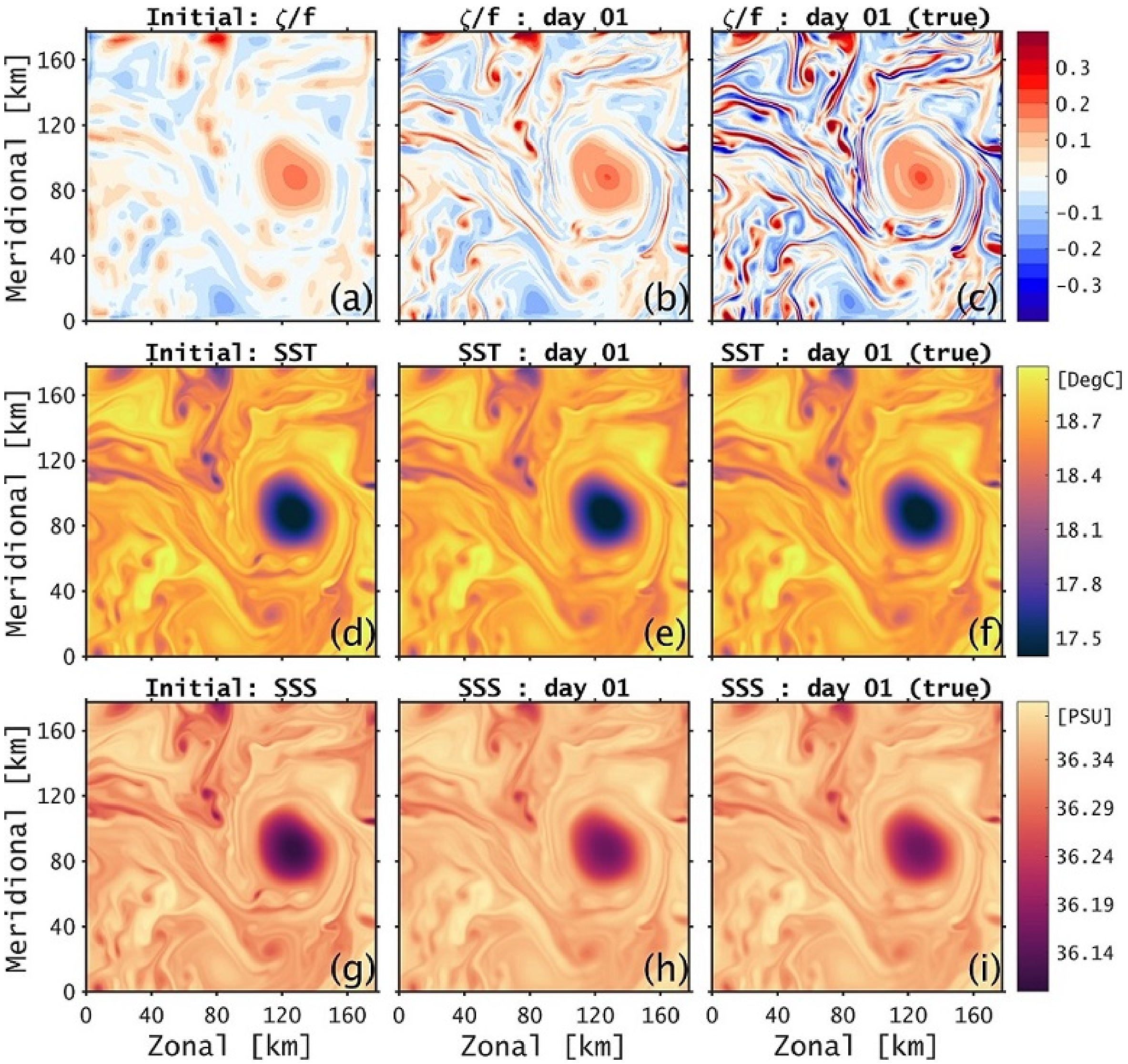

Figure 4.4: Results from a forward run with smoothed velocity and original temperature and salinity as initial conditions. (a,d,g) Initial conditions for the relative vorticity, temperature and salinity at the surface. (b,e,h) Model state after one day. (c,f,i) True sate after one day.

4.1.4 Error of first-guess and observations

In the cost function definition, prior and observation errors need to be specified. They were simply estimated as the standard derivation of the corresponding variables based on the 30-day ”truth” run. As the observations were taken from the ”true” state, they have, in principle, no error. However, a null error is not acceptable in an assimilation framework. The consistency between model, observation and prior information is the key to the success of the assimilation. The consistency is achieved when on average, each observation contributes a value of 1 to the cost (Köhl, 2020). We determined the observation error based on this criterion, and we named it ”intrinsic error”.

4.2 Impact of the assimilation window length

Our first purpose was to investigate to what extent the surface information is enough to constrain the 3-dimensional submesoscale field. The surface information includes surface velocity, SSH, SST and SSS. As already pointed out before, there is no need to assimilate velocity information as the model could constrain the velocity field by geostrophic adjustment. For simplicity, we start with assimilating SSH and later involve more observations.

In the first set of experiments (listed in Table 4.1), we seek to constrain the submesoscale field by assimilating SSH. Furthermore, we will explore the impact of the assimilation window length.

Ex-W	DA window	σ_{ssh}	Initial Condition
Ex-W1	5 days	σ_n	10 km smoothed
Ex-W2	10 days	σ_n	10 km smoothed
Ex-W3	15 days	σ_n	10 km smoothed

Table 4.1: Experiments exploring the length of the assimilation window. σ_{ssh} is the error of SSH and σ_n is the ”intrinsic error” determined according to subsection 4.1.4.

Three different assimilation window lengths (5 days, 10 days and 15 days) were tested. For the experiments with an assimilation window of 5 days and 10 days, forecasts until day 15 were obtained by continuing running the model forward for additionally 10 and 5 days, respectively.

In principle, all three experiments were able to bring the surface flow (here visualized by the normalized relative vorticity) back to their ”true” state at, respectively, day 5 (Figure 4.5), day 10 (Figure 4.6) and day 15 (Figure 4.7). The small filaments, most of which were removed by the smoothing process and failed to be recovered by the free model run (whose state from here on is termed ”prior state”), were well reproduced after assimilating SSH data (henceforth termed ”posterior state”).

The results imply that the surface submesoscale flow could be fully constrained by assimilating ”perfect” SSH observations.

Next, we investigated how deep the surface information incorporated via the assimilation process can penetrate the interior ocean. Taking Ex-W2 as an example, the same comparison as in Figure 4.6 but for the depth 25 m is presented in Figure 4.8. Although the submesoscale flows at 25 m were much weaker than at the surface, the assimilation process also captured the submesoscale features. The investigation into even deeper depths showed that assimilating SSH could constrain the submesoscale flows in the whole mixed layer. This is inspiring, as below the mixed layer, the submesoscale flows were weak or no longer significant. Hence we could conclude that assimilating SSH

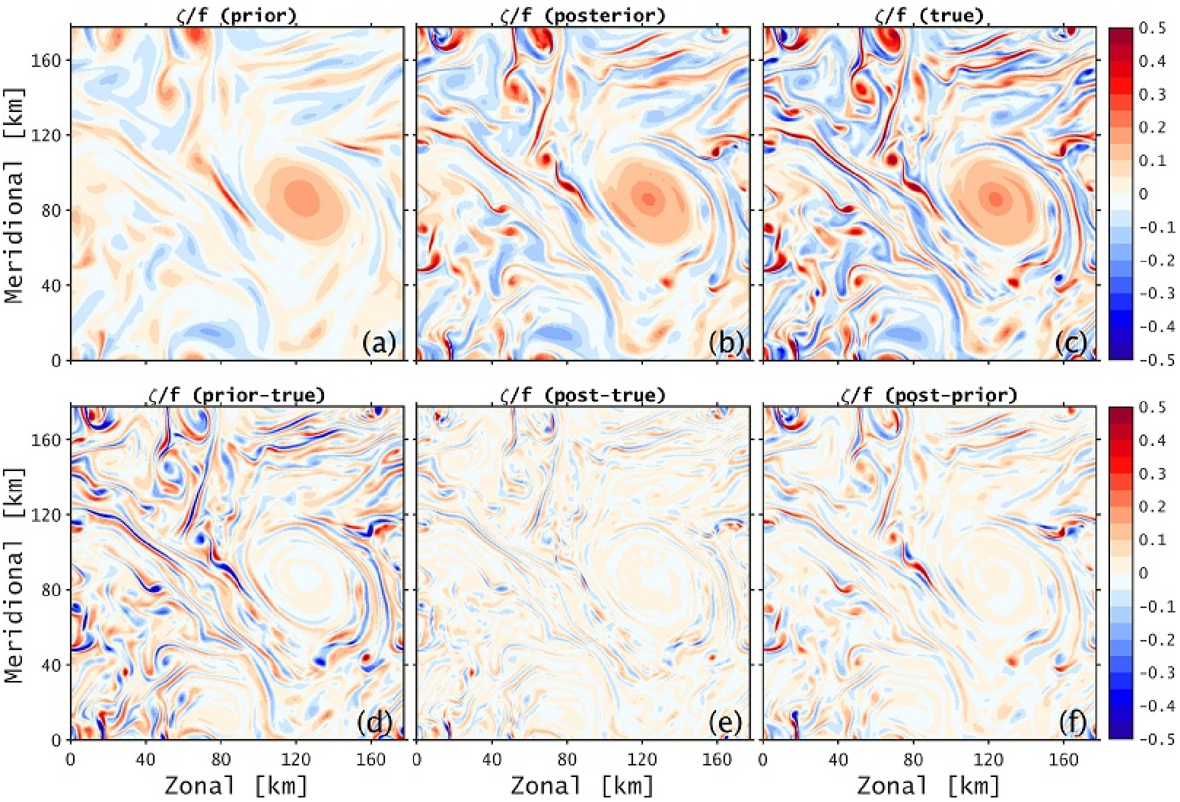

Figure 4.5: Comparison between prior, posterior and true state of surface ζ/f at time T = 5 days (from Ex-W1).

could constrain the 3D surface-intensified submesoscale flow, at least as far as it is represented in our idealized simulations.

To more easily quantify the effect of assimilating data, we introduce a normalized root mean square error (NRMSE) metric. NRMSE is a measure to evaluate how close the model state is to the "true" state and is defined as follows:

$$\mathrm{NRMSE} = \frac{1}{\sqrt{\overline{y_t^2}}}\sqrt{\frac{\sum(y_m - y_t)^2}{N}} \tag{4.2}$$

where y_m and y_t are the model state (prior or posterior) and "true" state, respectively; N is the total number of grid points. The normalization factor ensures that the comparison between the prior and posterior state is consistent and that the error field in different levels is comparable.

We plot the evolution of the depth-dependent NRMSE of ζ/f in Figure 4.9, from which we could come to the following conclusions. First, The improvements from assimilating SSH exist mainly in the mixed layer, i.e., down to about 50-m depth. Second, the improvements increased with time and depth in the mixed layer. This is due to the submesoscale patterns needing some time to form and adjust. Third, the improvement was no longer significant below the mixed layer, but the submesoscale

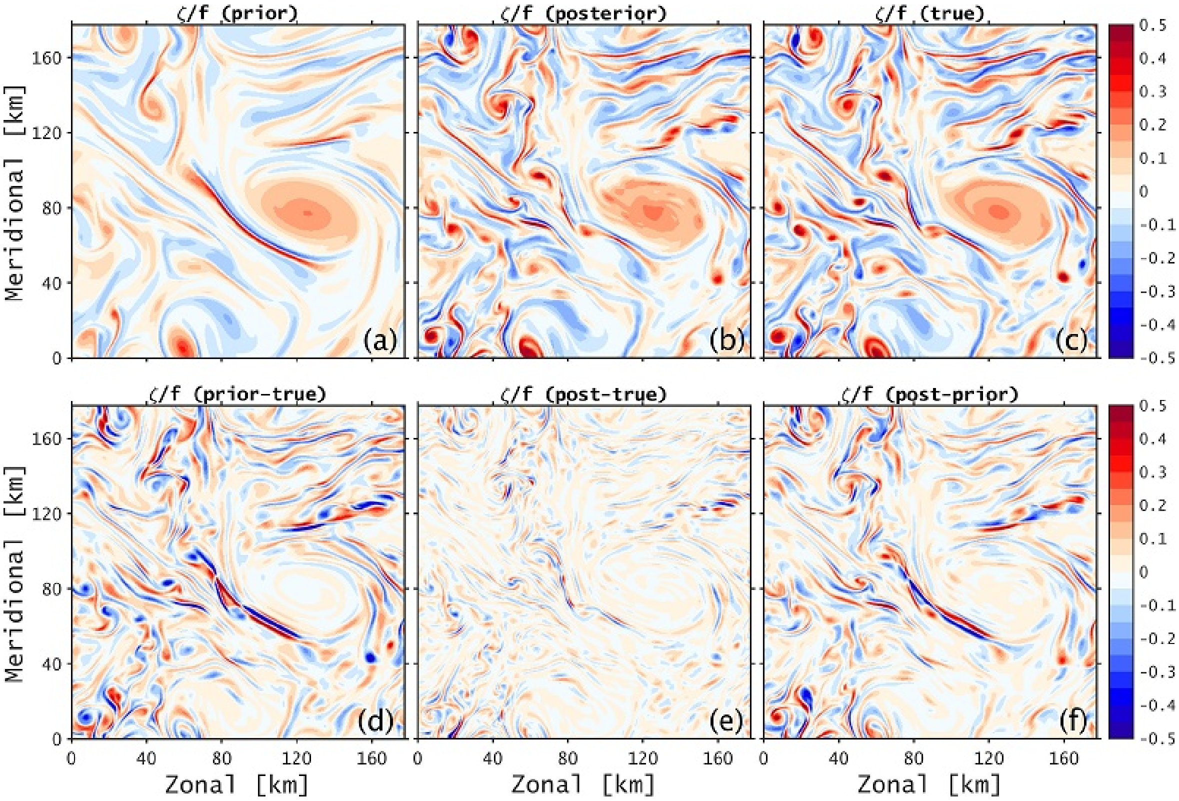

Figure 4.6: Comparison between prior, posterior and true state of surface ζ/f at time T = 10 days (from Ex-W2).

flows are much inactive below the mixed layer, where the RMSE was already small (not shown). Fourth, the improvement is always best at the time equal to the assimilation window length, but it persists for some days afterwards.

Some hints about the predictability of the submesoscale could also be concluded from Figure 4.9b and Figure 4.9e. When continuing integrating the forward model after assimilation, either after day 5 (for Ex-W1) or day 10 (for Ex-W2), the model state eventually evolves away from the "true" state. However, it could be seen that the state stays pretty close to the "true" state for about four days after stopping constraining by observations. Therefore, the predictable time of submesoscale flows in our model simulation seems to amount to 3∼4 days.

On the other hand, the length of the assimilation window also impacts the adjoint iterative process. A longer window leads to slower convergence, i.e., a slower decrease of the cost function (Figure 4.10) and demands more computational resources. Considering the predictability scales of the submesoscale flows as discussed above, the longer window ultimately is not a good choice. In the rest of this paper, we thus mainly concentrate on experiments with assimilation windows of 5 and 10 days.

In summary, assimilating SSH could constrain the 3D submesoscale flow structure in the mixed layer. The predictable period of the submesoscale flows was estimated to be 3∼4 days in our experiments. A longer assimilation window leads to increased

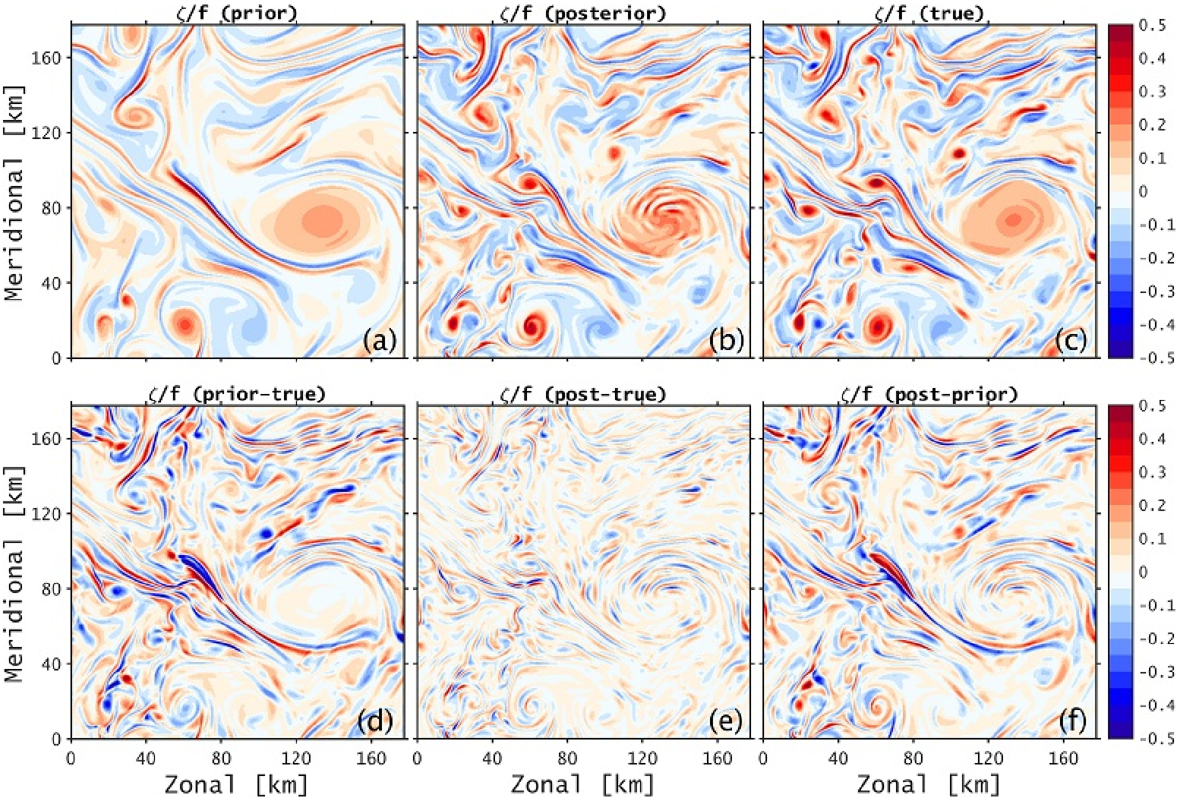

Figure 4.7: Comparison between prior, posterior and true state of surface ζ/f at time T = 15 days (from Ex-W3).

assimilation benefits at the time equal to the length of the window but will slow the convergence of the assimilation process.

With the only SSH being assimilated, the dynamic processes adjusted the temperature and salinity fields. Taking Ex-W2 as an example, the temperature at T = 10 days was significantly improved after assimilation (Figure 4.11). In the mesoscale eddy region the temperature in the prior run is generally higher than the "true" state (Figure 4.11d). This was corrected by the assimilation (Figure 4.11f), leading to a slightly lower temperature compared to the "truth" in the posterior state (Figure 4.11e). In the filaments surrounding the mesoscale eddy, the submesoscale temperature structure was also reconstructed by the assimilation processes (Figure 4.11b). Same as for the flow field, this is also the case in deeper layers until the base of the mixed layer (not shown).

When turning attention to the salinity field, however, the impact of assimilating SSH was not positive. In the mesoscale eddy region, the bias to the "true" state was actually slightly increased (Figure 4.12d and Figure 4.12f). On the contrary, the salinity structure in the filaments surrounding the vortex benefited from the assimilation. The reason why the filaments and vortex regions have different behaviour remains open.

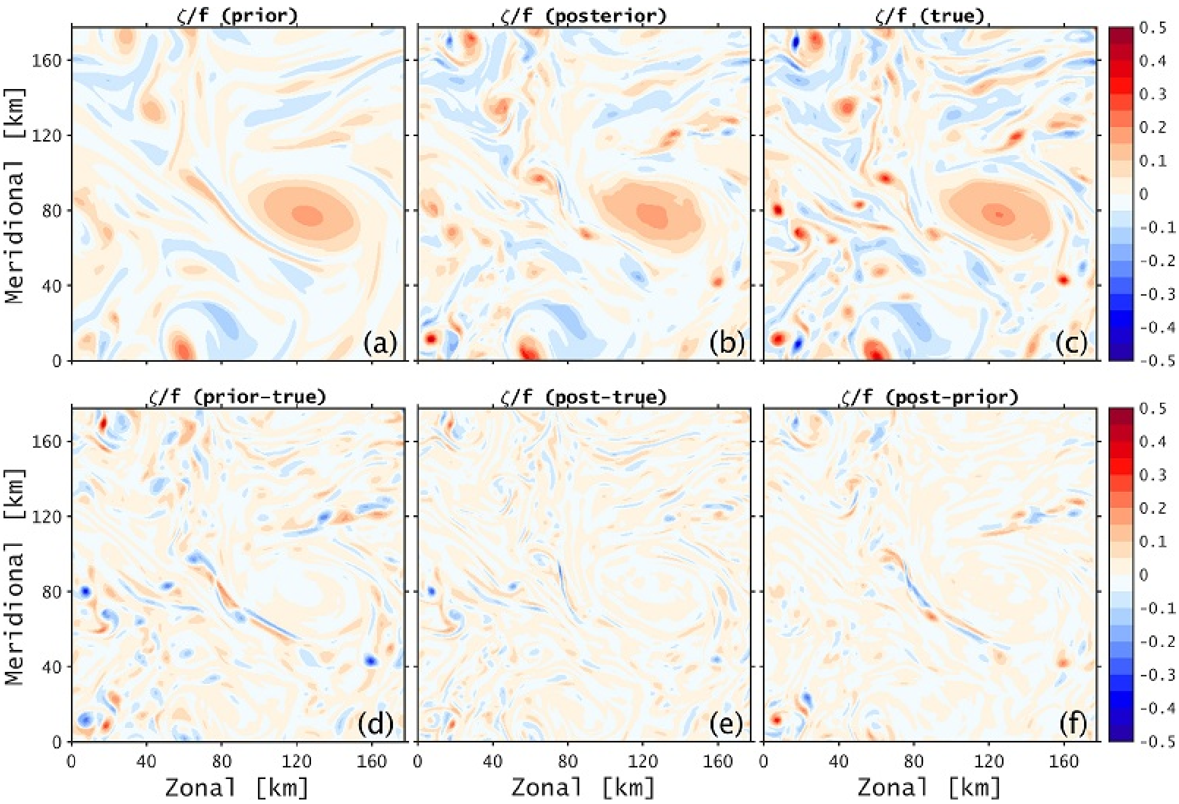

Figure 4.8: Comparison between prior, posterior and true state of ζ/f at 25 m and at time T = 10 days (from Ex-W2).

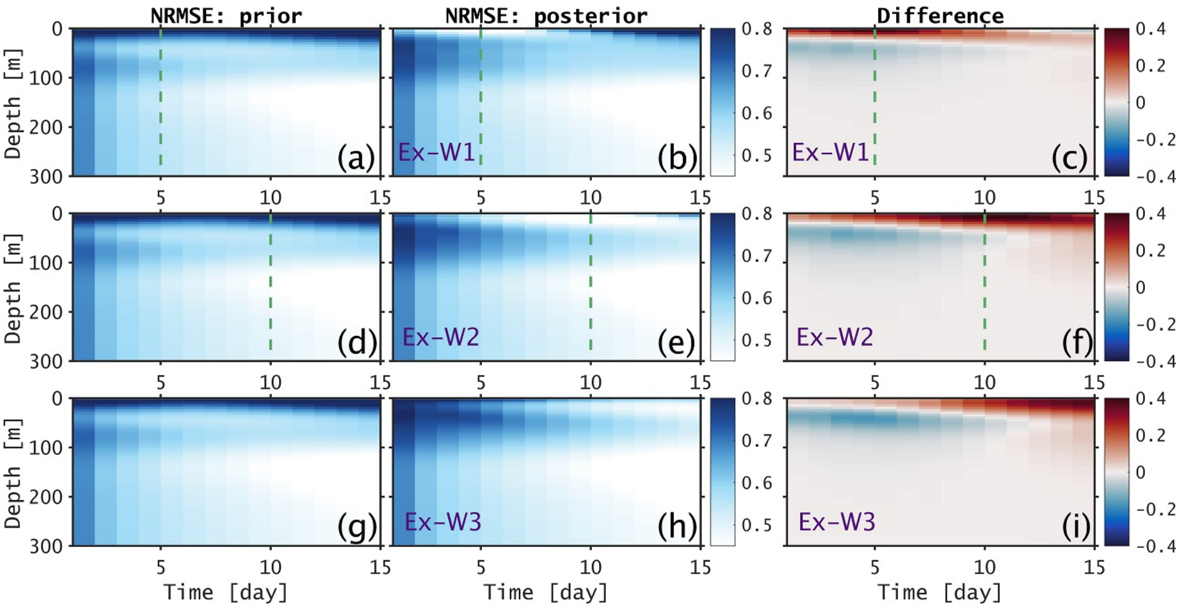

Figure 4.9: The comparison of NRMSE between the prior and posterior states in experiments Ex-W. The "Difference" is obtained by subtracting the posterior from the prior, i.e., red means improvement after assimilation. The green dashed lines in Ex-W1 and Ex-W2 indicate the time equal to the length of the assimilation window.

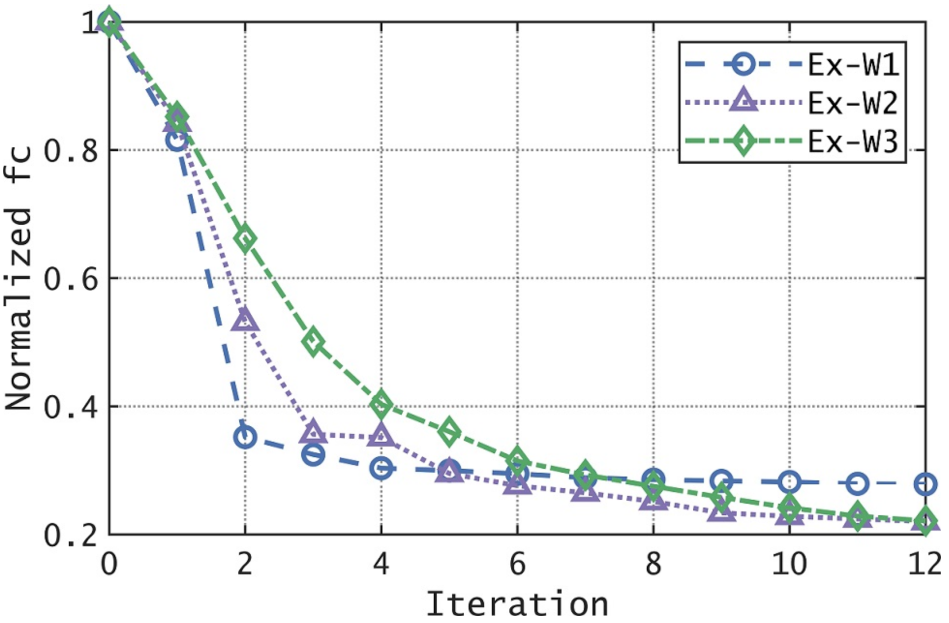

Figure 4.10: Evolution of the normalized cost function as function of iteration number.

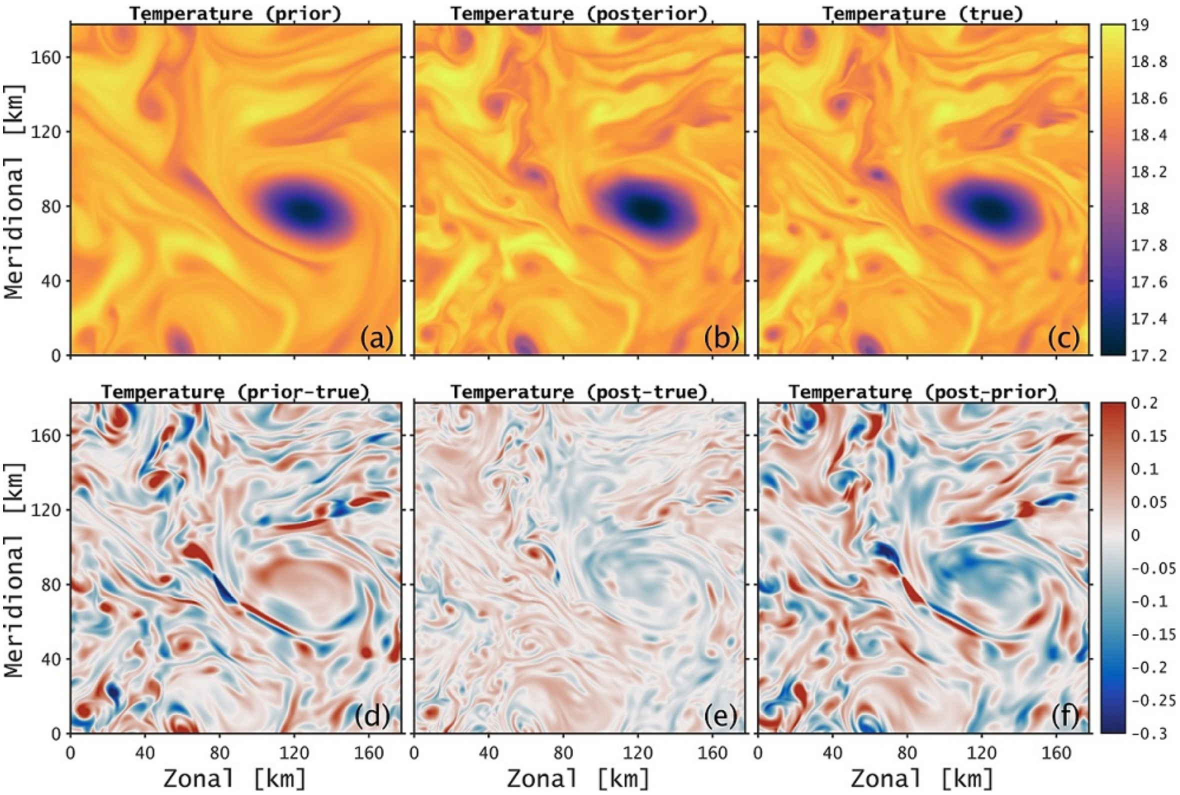

Figure 4.11: Comparison between prior, posterior and true state of surface temperature at time T = 10 days (from Ex-W2).

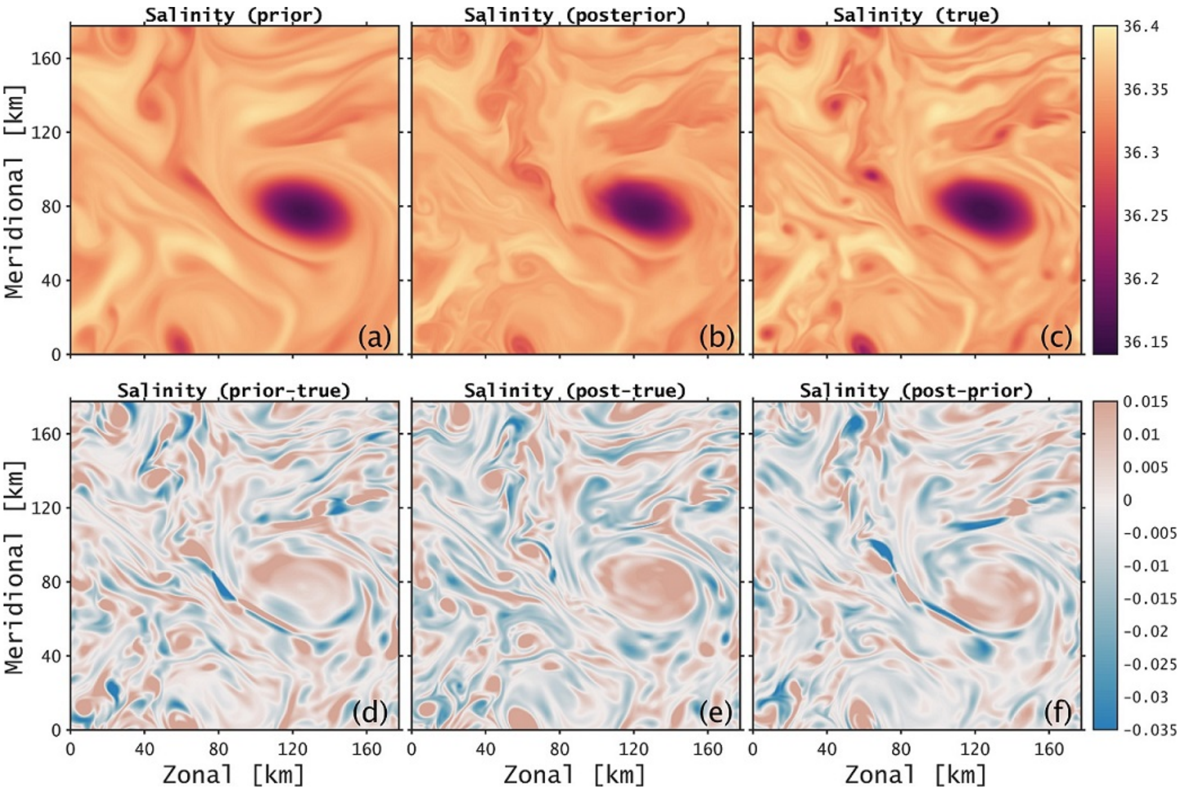

Figure 4.12: Comparison between prior, posterior and true state of surface salinity at time T = 10 days (from Ex-W2).

4.3 Impact of assimilating additional surface observations

In a second step, we assimilated SST and SSS to test the impact of having another set of observations. This set of experiments (Table 4.2) includes three runs: assimilating SST only, assimilating SST and SSH together and assimilating SSH, SST and SSS simultaneously.

Ex-ADD	DA window	SSH	SST	SSS
Ex-ADD1	5 days	*no*	*yes*	*no*
Ex-ADD2	5 days	*yes*	*yes*	*no*
Ex-ADD3	5 days	*yes*	*yes*	*yes*

Table 4.2: Experiment exploring the impact of multiple assimilated variables.

Before examining the impact of assimilating additional surface information, we investigate the individual contribution to density by temperature and salinity alone. This will give an idea if salinity is important to the dynamical processes or if temperature alone is responsible.

Ignoring compression effects, a fair approximation to the change of density is (Pedlosky, 1987):

$$\begin{aligned}\Delta\rho &= \left.\frac{\partial\rho}{\partial\theta}\right|_{S,p}\Delta\theta + \left.\frac{\partial\rho}{\partial S}\right|_{\theta,p}\Delta S \\ &= \underbrace{-\rho_0\alpha\Delta\theta}_{\text{term 1}} + \underbrace{\rho_0\beta\Delta S}_{\text{term 2}},\end{aligned} \tag{4.3}$$

where ρ is density, S is salinity, θ is potential temperature, ρ_0 is a reference density, α and β are the thermal expansion and haline contraction coefficients. The latter were calculated based on McDougall (1987). One typical result for the terms in Equation 4.3 is presented in Figure 4.13.

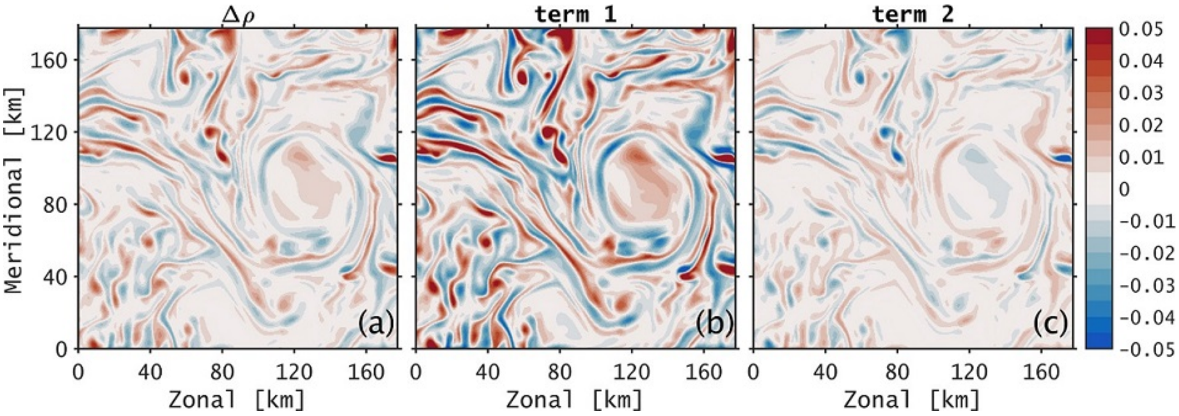

Figure 4.13: A typical distribution of $\Delta\rho$, $term1$ and $term2$ (Equation 4.3) at the surface in our simulation.

The consistent pattern and sign between $\Delta\rho$ and $term1$ in Figure 4.13 revealed that the variability in density ($\Delta\rho$) is mainly dominated by the change of temperature ($term1$). But the salinity also modulated the change of density. In fact, the positive density change by the decrease of temperature ($term1$ positive) was partly balanced by the decrease of salinity ($term2$ negative). The different contributions to density by temperature and salinity show that our model is highly temperature-stratified. This is not surprising since it was started and spun up with constant salinity and differential temperature fields.

As pointed above, assimilating only SSH could hardly constrain the submesoscale salinity field, so we tried to solve this problem by assimilating more surface information, in particular, SST and SSS. Before assimilating both, we first test the individual impact by assimilating SST only. SST is closely connected with SSH by dynamic processes and tied with salinity by the equation of state. Therefore, it is interesting to see to what extent assimilating SST could impact both the flow and the salinity field.

Comparing Figure 4.14 and Figure 4.5 we can see that assimilating SST instead of SSH has only a little impact on the improvement of the submesoscale salinity. This is also true when assimilating both SSH and SST (Ex-ADD2, third column). However, as expected, the temperature field improves when additionally assimilating SST and even slightly more when assimilating both SSH and SST. When assimilating SSS additionally (fourth column), we could estimate all three fields well. The submesoscale salinity field gets constrained in this case, and the temperature field is also better reproduced than without assimilating SSS.

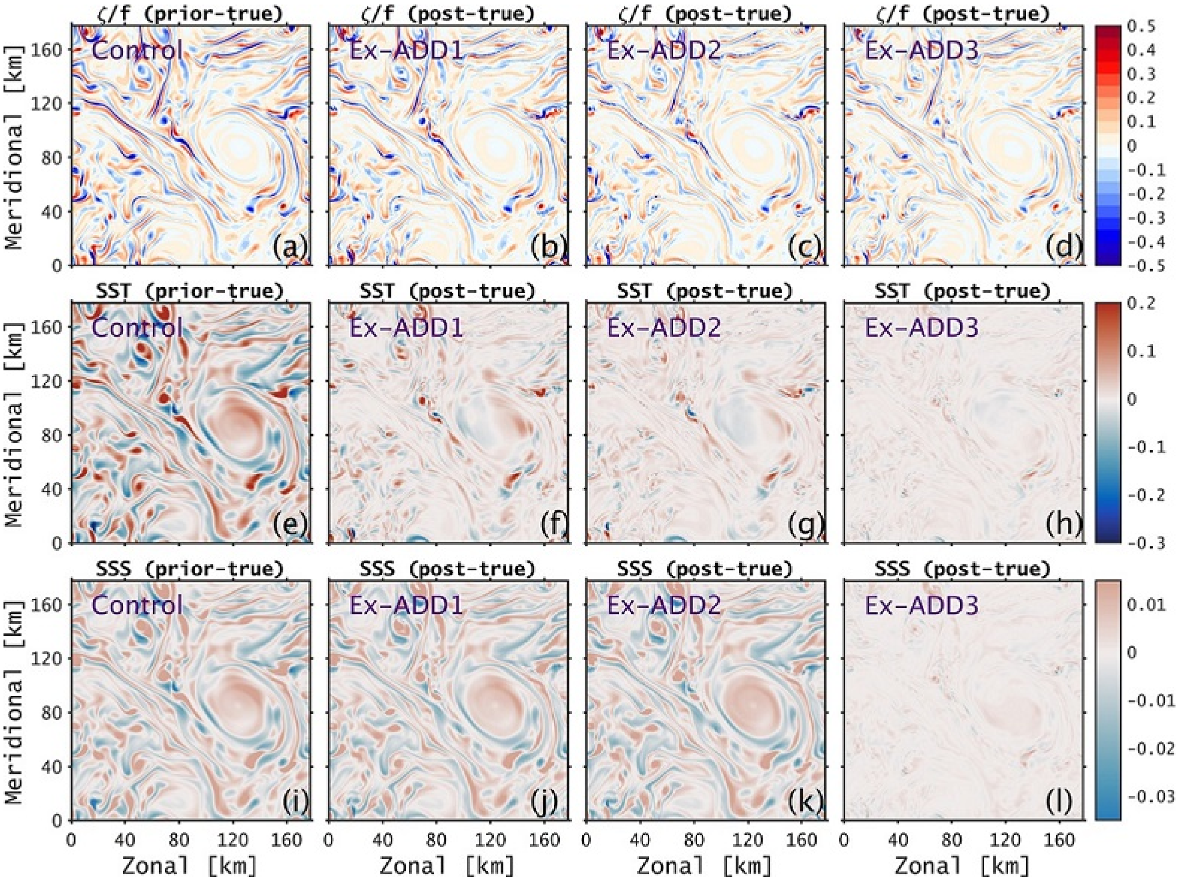

Figure 4.14: Differences between posterior and true surface state for all Ex-ADD experiments (see Table 4.2) at T = 5 days. Control corresponds to the state without observations being assimilated.

Looking at the individual contributions to the total cost function and their evolution during the iterative process for the case of assimilating all three surface quantities (Figure 4.15), we can notice a pronounced and consistent decrease in the SST and SSS misfit and a much more moderate decrease of the SSH error. The slight increase in initial temperature (*temp*0) and salinity (*salt*0) penalties does not play a significant role.

In summary, 1) assimilating SST alone fails to constrain the submesoscale flow and salinity field but improves the SST reconstruction largely; 2) assimilating SST and SSH together fails to constrain the submesoscale salinity field, bringing no improvement relative to assimilating only SST; 3) assimilating SST, SSH and SSS simultaneously

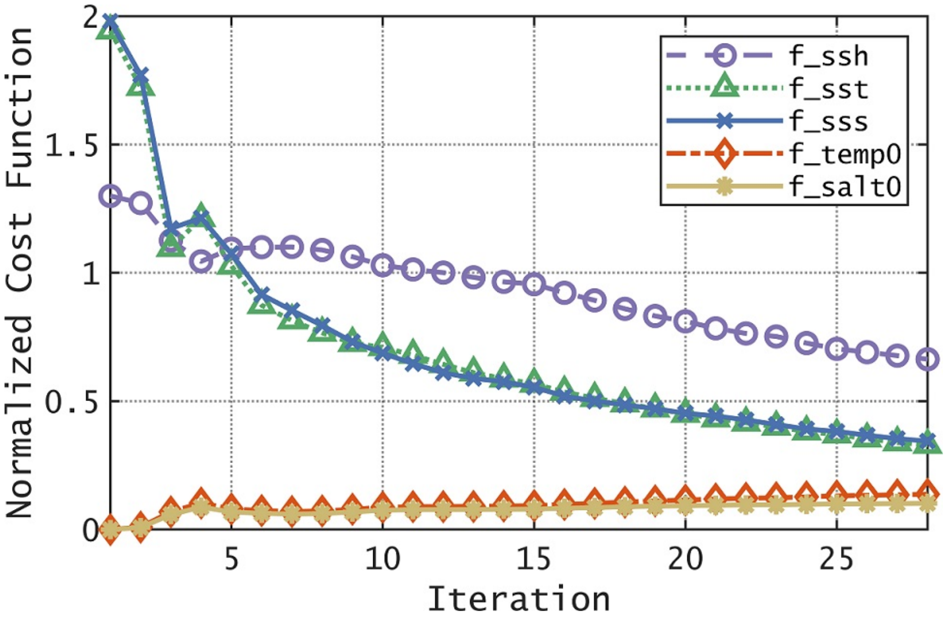

Figure 4.15: The cost function normalized by the number of observations for Ex-ADD3.

could successfully constrain both velocity and property fields at the surface. However, assimilating the three observations still failed to constrain the submesoscale fields in deeper depths, where the submesoscale signal is small.

4.4 Impact of degrading the observational spatial resolution

Next, we have spatially degraded the SSH observations to explore the assimilation sensitivity to observation resolution. The strategy to reduce the SSH observation density is primarily inspired by satellite tracks. We take all observations along the meridional direction but sub-sample them along the zonal direction (Figure 4.16). We figuratively call them ”tracks”, and the degradation increases with increasing track gap. Table 4.3 shows a series of conducted experiments (noted: Ex-DSRxx) to test the impact of SSH measurement density. Two separate sets of experiments, with five days and ten days assimilation windows, were performed.

We implemented two sets of experiments with two assimilation windows to explore the sensitivity to the resolution in the observations. The resolution decreased gradually in each set of experiments, as listed in Table 4.3. The surface ζ/f at T = 10 days for the experiments with an assimilation window of ten days is presented in Figure 4.17. It can be seen that the distribution of ζ/f is closer to the ”true” state (Figure 4.17a) when using the full resolution (Ex-DSR00, Figure 4.17b). With decreasing resolution in the observations (Ex-DSR02∼Ex-DSR12, Figure 4.17c∼Figure 4.17h) the retrieved solution approaches more to the control unconstrained experiment (Figure 4.17i). This

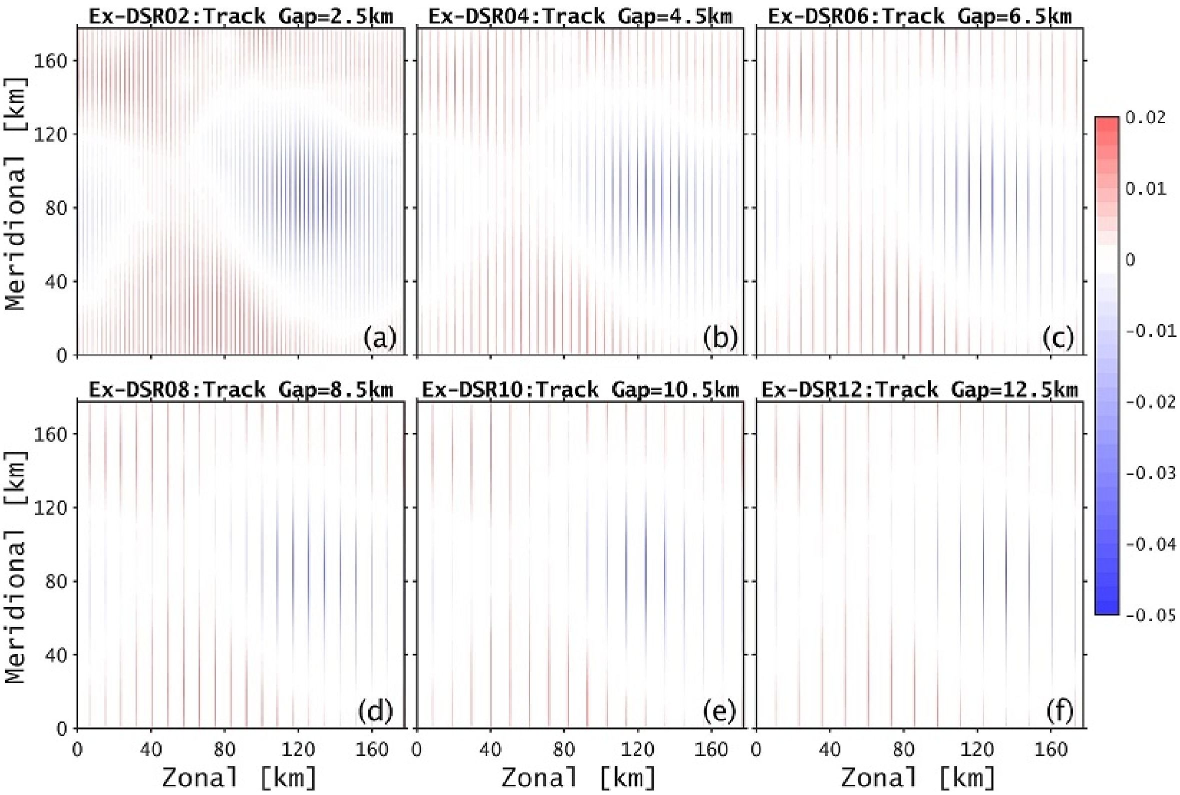

Figure 4.16: SSH observation strategy for selected Ex-DSR experiments, shown for day 1.

Ex-DSR	DA window	σ_{ssh}	Track Gap
Ex-DSR00	10/5 days	σ_n	0.5 km
Ex-DSR01	10/5 days	σ_n	1.5 km
Ex-DSR02	10/5 days	σ_n	2.5 km
Ex-DSR03	10/5 days	σ_n	3.5 km
Ex-DSR04	10/5 days	σ_n	4.5 km
Ex-DSR05	10/5 days	σ_n	5.5 km
Ex-DSR06	10/5 days	σ_n	6.5 km
Ex-DSR07	10/5 days	σ_n	7.5 km
Ex-DSR08	10/5 days	σ_n	8.5 km
Ex-DSR09	10/5 days	σ_n	9.5 km
Ex-DSR10	10/5 days	σ_n	10.5 km
Ex-DSR11	10/5 days	σ_n	11.5 km
Ex-DSR12	10/5 days	σ_n	12.5 km

Table 4.3: Experiments exploring the density in observational coverage.

implies that a larger observation resolution always leads to better recovered submesoscale flow.

Figure 4.18a∼Figure 4.18c presents the distribution of NRMSE of surface ζ/f as a

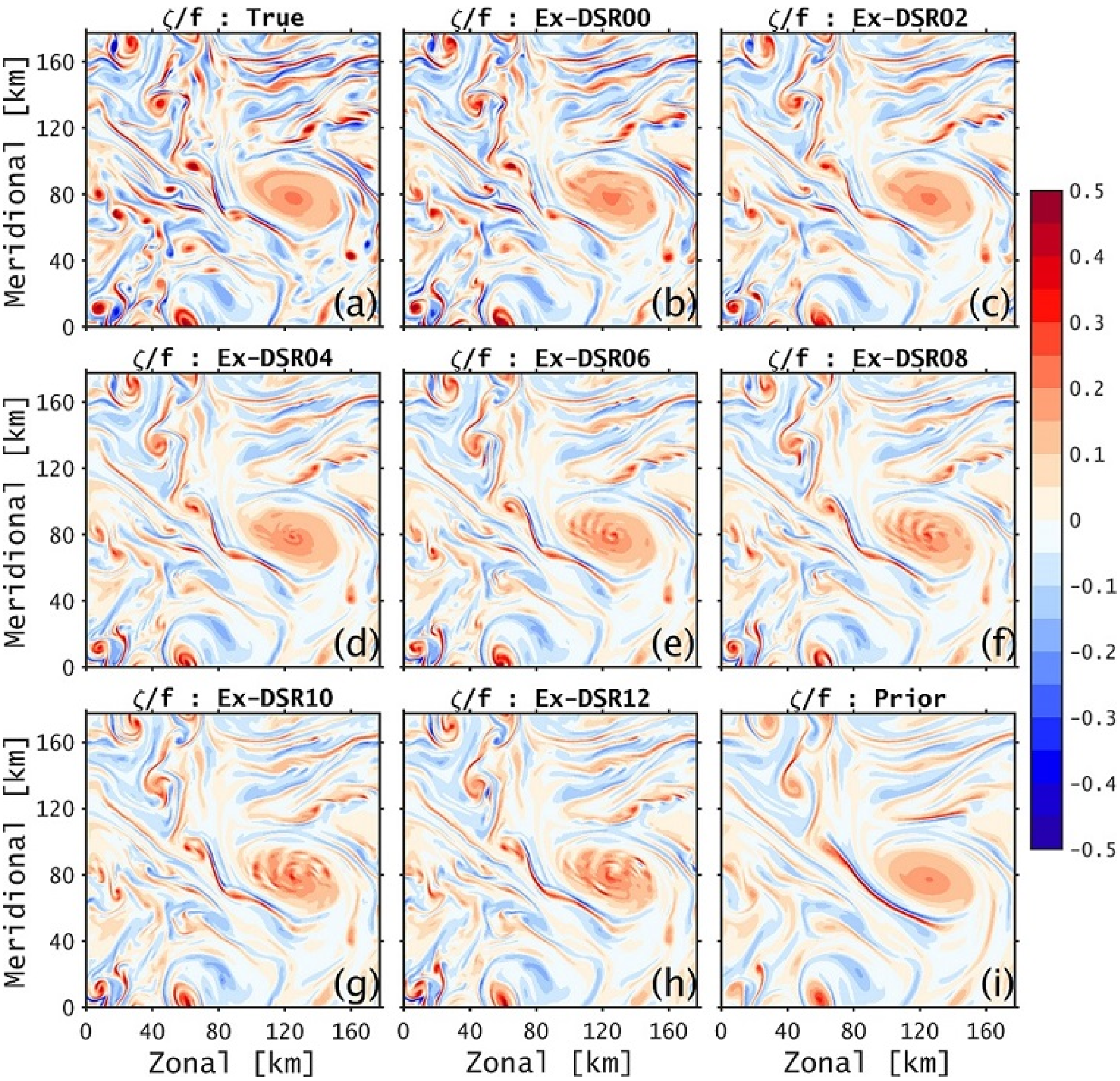

Figure 4.17: Comparison of surface ζ/f at T = 10 days for the "truth", in selected Ex-DSR (see Table 4.3) and in the "control" runs.

function of "track gap" for two sets of experiments with 10 days (Figure 4.18a) and 5 days (Figure 4.18b) assimilation windows. Several results can be deduced. First, the largest assimilation benefit is achieved on the last day of each assimilation window. Second, the impact of the assimilation decreased with increasing "track gap" (i.e., with coarser observations). Third, the impact of observational resolution has a strong sensitivity to the assimilation window. For instance, if one wants to have the NRMSE level at day 10 to be lower than 1.5 times the NRMSE of the full resolution experiment, it requires a "track gap" to be at most 6 km if using ten days of assimilation (see intersection of the dashed purple line and solid green line in Figure 4.18c). But the gap must be less than 1.5 km when the assimilation window equals five days (see solid blue and purple dashed lines in Figure 4.18c). Forth, if interested in retrieving day 5, the NRMSE is quite close between the cases of assimilating high-resolution observations ('track gap' less than 2 km), both with an assimilation window of five or ten days. The difference enlarges when degrading the observation resolution (see the diverging dashed green and blue lines in Figure 4.18c).

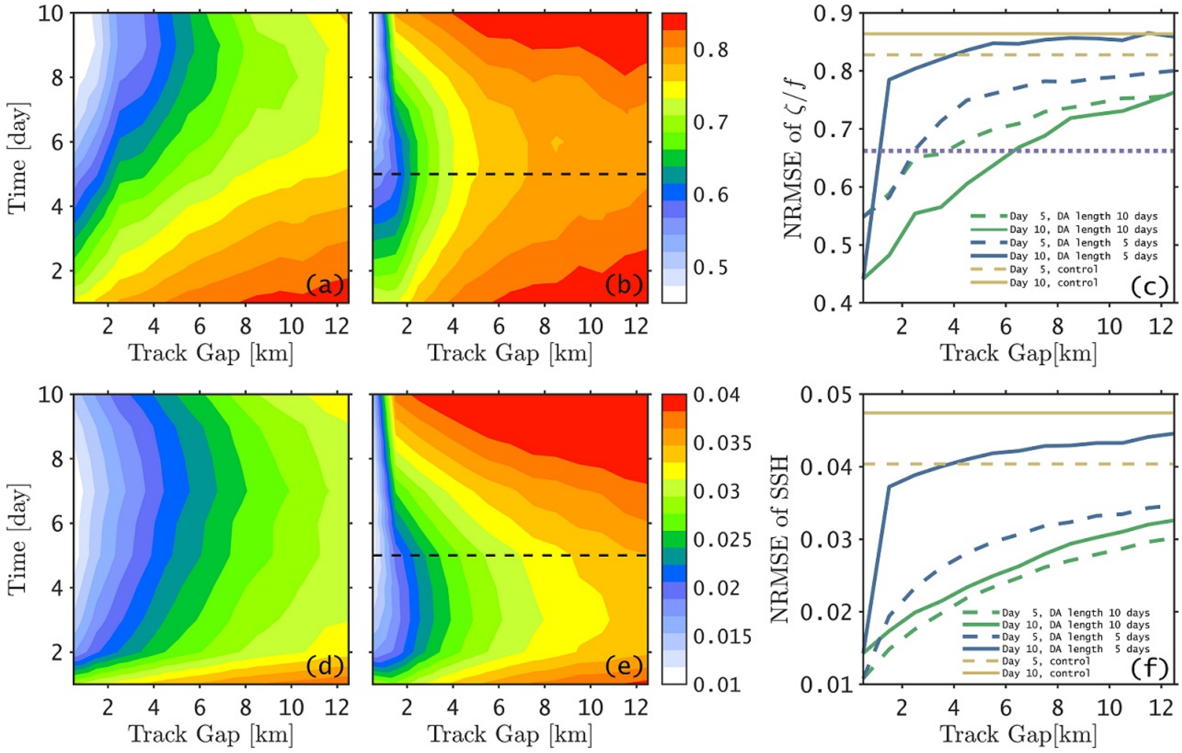

Figure 4.18: (a) Temporal evolution of NRMSE of surface ζ/f as a function of observation "track gap" distance for the experiments with (a) assimilation window of 10 days and (b) assimilation window of 5 days. The black dashed line indicates that observations were only assimilated until that time. (c) NRMSE of surface ζ/f at day 10 and day 5 for the four experiments and the control. The purple dashed line indicates a NRMSE 1.5 times larger than the minimum value with full observational resolution. (d)-(f) are the same as (a)-(c) but for SSH.

The NRMSE of SSH shows a similar behaviour as described for the surface ζ/f (Figure 4.18d∼Figure 4.18f) but interestingly, there is a difference regarding the time when the lowest NRMSE is attained. The lowest value arrives at about 2∼3 days before the end of the assimilation window. Since SSH has larger scales in general, this might mean that only after the broader scales have been constrained can the smallest scales correctly develop and be recovered. In other words, this suggests the assimilation procedure is correcting the mesoscale, which then promote the "correct" development of the submesoscale by instability processes.

By comparison with the control experiment, all the "track gap" experiments represented the submesoscale better than without assimilating observations. It is also clear that if we keep increasing the "track" separation, the assimilation results will be soon approaching the control experiment (see yellow lines in Figure 4.18c and Figure 4.18f).

4.5 Impact of degrading the observational temporal resolution

We implemented five experiments with decreased temporal resolution (as in Table 4.4). Note that each experiment ensures that the observation at day 10 was assimilated.

Ex-DTR	DA window	σ_{ssh}	Track Gap	Observation Time
Ex-DTR00	10 days	σ_n	0.5 km	every day
Ex-DTR01	10 days	σ_n	0.5 km	day 2,4,6,8,10
Ex-DTR02	10 days	σ_n	0.5 km	day 1,4,7,10
Ex-DTR03	10 days	σ_n	0.5 km	day 2,6,10
Ex-DTR04	10 days	σ_n	0.5 km	day 5,10

Table 4.4: Experiments exploring the impact of the temporal resolution in the observations.

We implemented a set of experiments using a 10-days assimilation window to study the sensitivity to the temporal resolution in the observations. The SSH was assimilated from daily to every 5 days (”temporal gap” therefore from 1 to 5 days), ensuring the observation on day ten was assimilated (see the solid purple dots in Figure 4.19a). In general, the submesoscale flow is better constrained at the end of the assimilation window if more observations are assimilated, although the difference was not that considerable (Figure 4.19b).

Interestingly, the NRMSE of surface ζ/f in the experiment with a ”temporal gap” of 2 days is larger than that in the 3 days case. This implies that the information contained on day one may be needed.

Again, SSH shows similar behaviour as surface ζ/f in what regards the impact of temporal resolution of the observations. Also shown is the above-described difference that the NRMSE minimum is reached three days before the end of the assimilation period (Figure 4.19c). On day 10, the NRMSE after assimilation is much lower than that of the control experiment (Figure 4.19d).

4.6 Impact of degrading the accuracy of observations

Next, we investigated the impact of increasing the observational error by applying random Gaussian-distributed noise. In the process, we found the maximum error allowed in our configuration to constrain the submesoscale variability still.

To generate noisy observations we set the mean (b) and the standard error (σ_e) of the noise to $b = 0$ and $\sigma_e = x\, \sigma_n$ (with $x \geq 0$) and generate the noise as $y = \sigma_e randn(N) + b$.

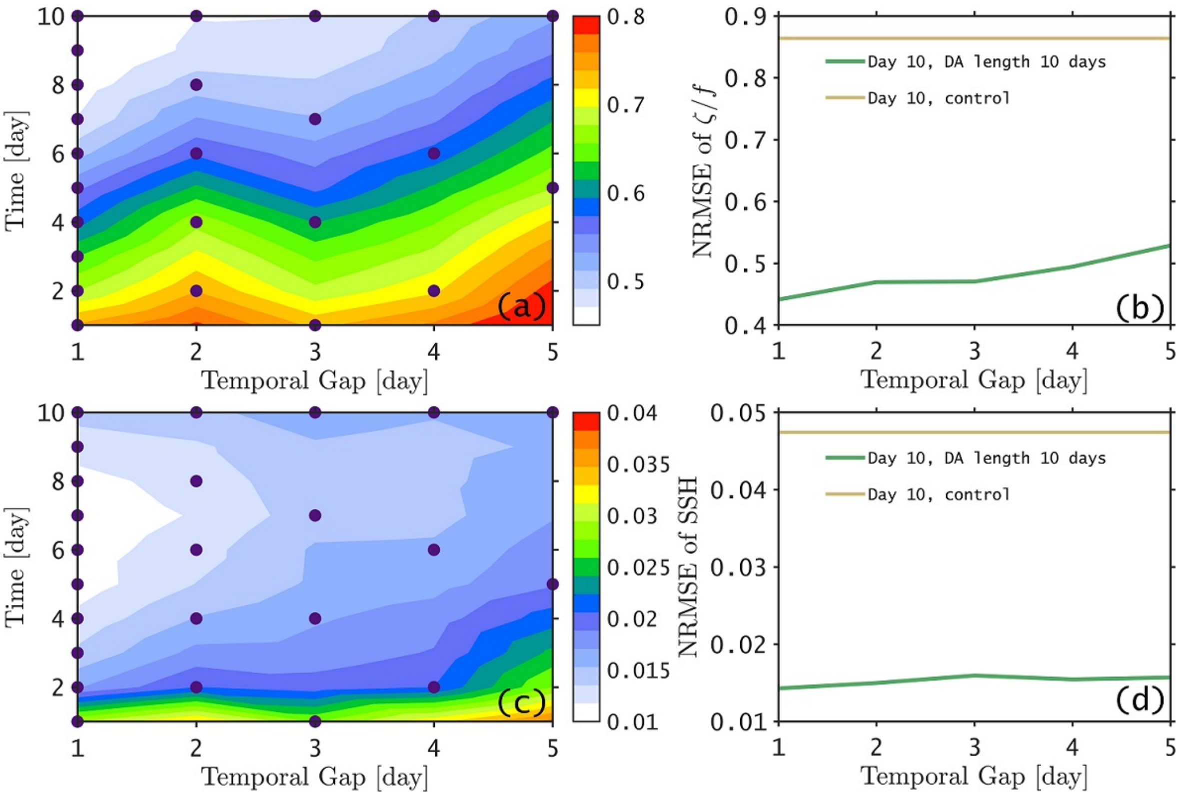

Figure 4.19: (a) Temporal evolution of NRMSE of surface ζ/f as a function of observation ”temporal gap”, for the experiment using an assimilation window of 10 days. The purple dots indicate the times of assimilated observations. (b) NRMSE of surface ζ/f at day 10 for all experiments and for the control run. (c) and (d) are the same as (a) and (b) but for SSH.

Finally we added this noise to the original observation $SSH = SSH + y$ and redefined the observation error as $\sigma_{SSH} = \sigma_n + \sigma_e$, where σ_n is the intrinsic error of the original SSH. We have implemented a set of experiments listed in Table 4.5, which increase the noise level gradually (by increasing x from 0 to 4).

Ex-DOE	DA window	σ_{ssh}	Track Gap	Observation Time
Ex-DOE00	10 days	σ_n	0.5 km	every day
Ex-DOE01	10 days	$1.5\sigma_n$	0.5 km	every day
Ex-DOE02	10 days	$2\sigma_n$	0.5 km	every day
Ex-DOE03	10 days	$2.5\sigma_n$	0.5 km	every day
Ex-DOE04	10 days	$3\sigma_n$	0.5 km	every day
Ex-DOE05	10 days	$3.5\sigma_n$	0.5 km	every day
Ex-DOE06	10 days	$4\sigma_n$	0.5 km	every day

Table 4.5: Experiments exploring the impact of random noise added to the observations.

An example of degraded SSH is presented in Figure 4.20.

The surface ζ/f at T = 10 days is presented in Figure 4.21. It is clear from the figure

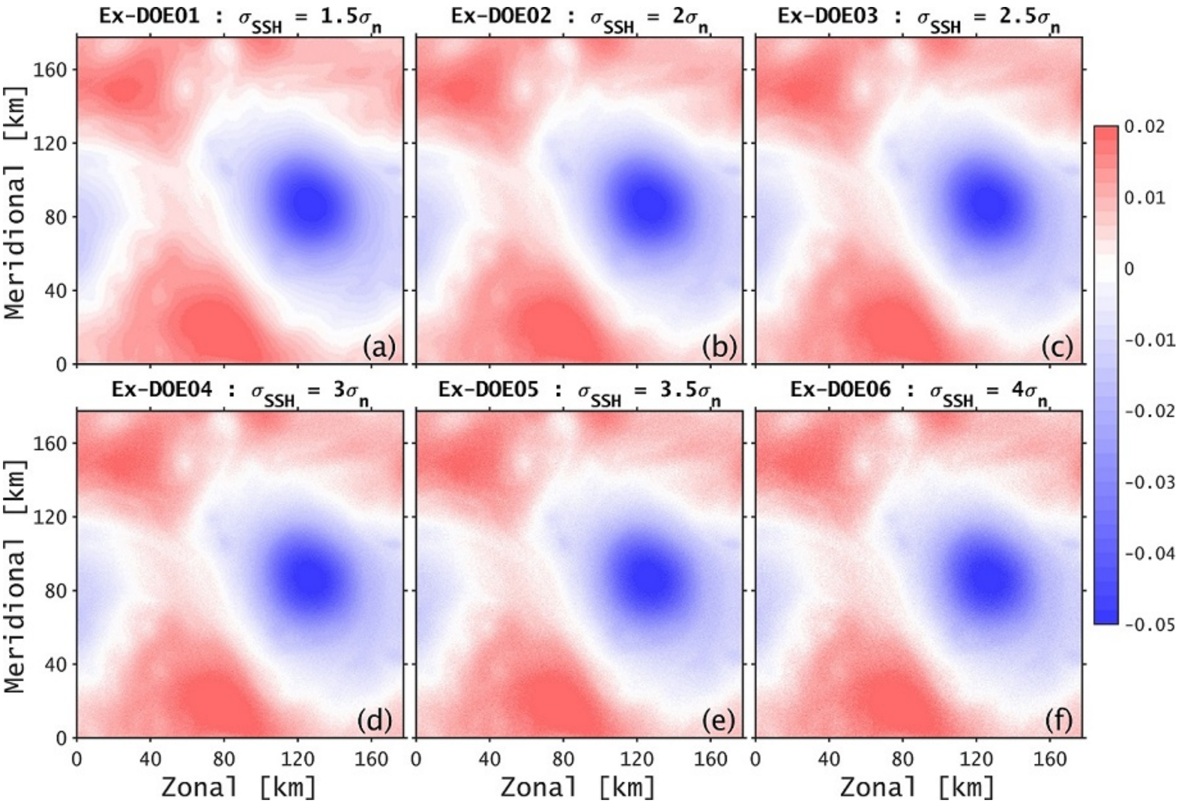

Figure 4.20: Example of SSH distribution for different noise levels of experiments Ex-DOE.

that the submesoscale patterns were well constrained in the experiments with small random errors and that the submesoscale variability faded out with increasing SSH added error.

More in detail, the NRMSE of surface ζ/f and SSH increased with increasing SSH random error (Figure 4.22), in the figure presented as a factor applied to the intrinsic noise. Note that all experiments are still below the value of NRMSE for the control experiment. Again, the SSH minimum NRMSE is achieved days before the respective minimum in ζ/f.

4.7 Impact of increased submesoscale activity

Previous experiments are all based on the no forcing case (see Chapter 2 for details on the forcing). Despite the high-resolution simulations ensuring an abundant submesoscale, it is unclear how the above sensitivity results change with increasing submesoscale activity. In this sense, we implemented a set of simulations as section 4.4 but for the wind forcing case, which shows even more complex submesoscale features.

The assimilation simulations started at about 30 days after the wind event (lasting 17 hours) was added, i.e., when the spin-down process finished and a steady, very

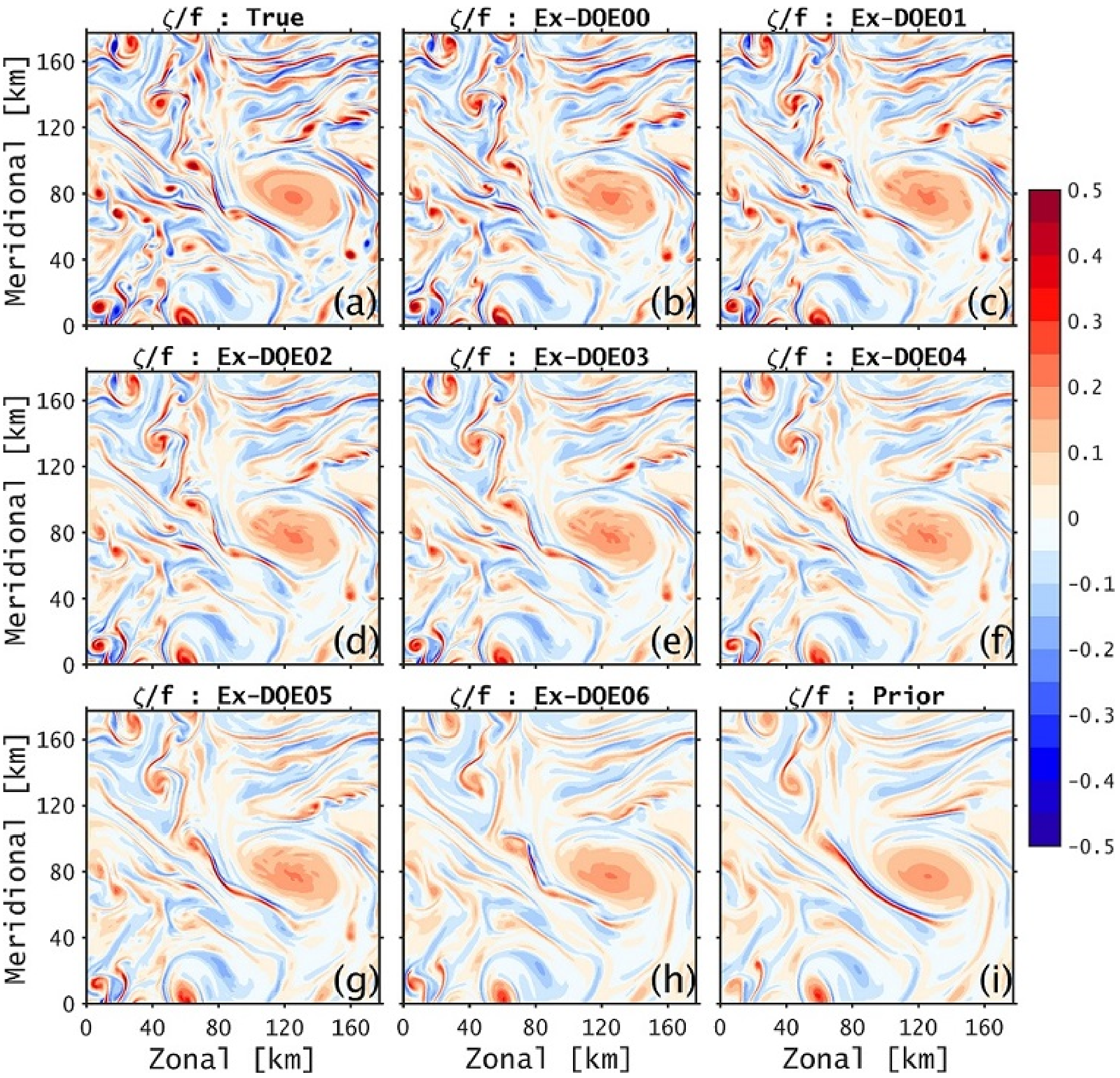

Figure 4.21: Comparison of surface ζ/f at time T = 10 days for the "truth", in selected Ex-DOE (see Table 4.5) and in the "control" runs.

rich submesoscale field was preserved. The impact of degrading spatial resolution was studied as section 4.4 but only for the ten days assimilation window (Table 4.6).

The surface ζ/f at T = 10 days for the experiments with an assimilation window of ten days is presented in Figure 4.23. The decreasing assimilation effect, as was seen in the no wind case (Figure 4.17), is reproduced. However, the decreasing effect with increasing observation track gap is faster in the wind forced case. Moreover, the temporal evolution of NRMSE shows a more robust view of this conclusion (Figure 4.24). This implies that constraining the submesoscale requires even denser observations if the submesoscale variability increases.

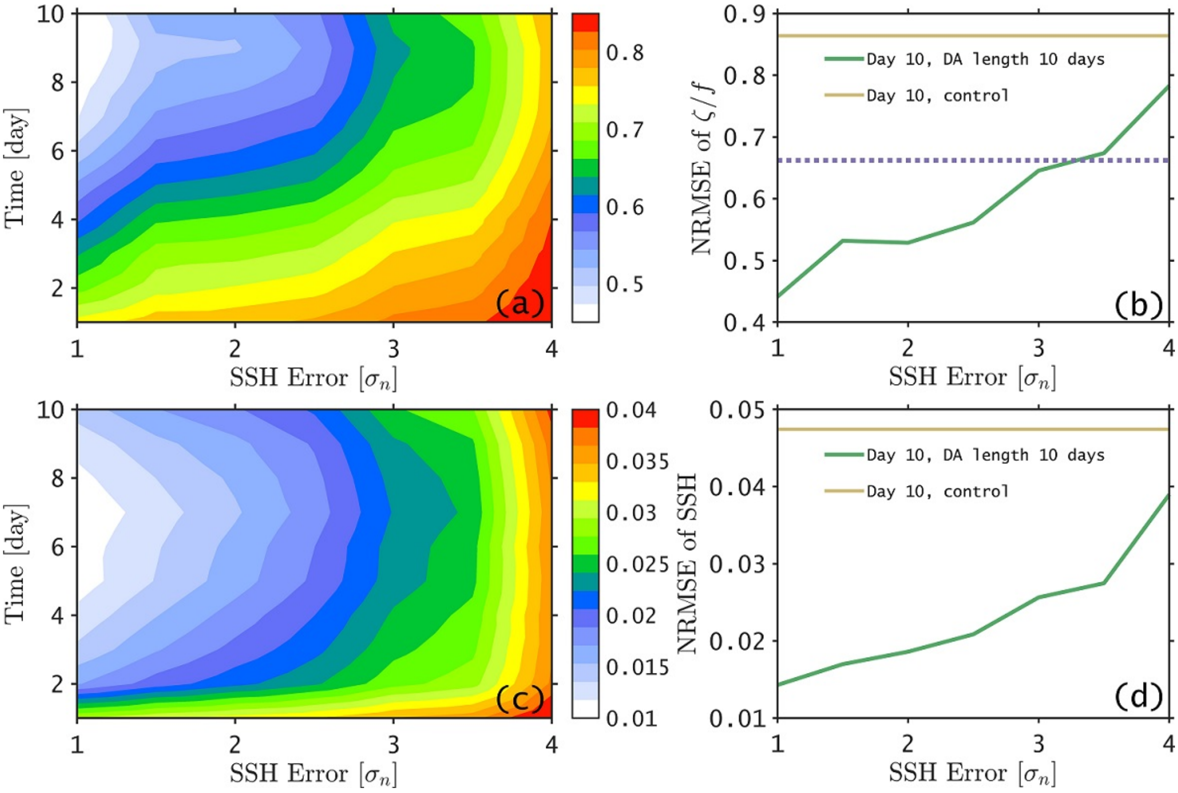

Figure 4.22: (a) Temporal evolution of the NRMSE of surface ζ/f as a function of random error added to SSH for the experiment with an assimilation window of 10 days. The NRMSE of ζ/f at day 10 for all experiments is shown in (b). The purple dashed line indicates an NRMSE 1.5 times larger than the smallest value of the green solid line. (c) and (d) are the same as (a) and (b) but for SSH.

Ex-DSR	DA window	σ_{ssh}	Track Gap
Ex-DSR00	10 days	σ_n	0.5 km
Ex-DSR01	10 days	σ_n	1.5 km
Ex-DSR02	10 days	σ_n	2.5 km
Ex-DSR03	10 days	σ_n	3.5 km
Ex-DSR04	10 days	σ_n	4.5 km
Ex-DSR05	10 days	σ_n	5.5 km
Ex-DSR06	10 days	σ_n	6.5 km
Ex-DSR07	10 days	σ_n	7.5 km
Ex-DSR08	10 days	σ_n	8.5 km
Ex-DSR09	10 days	σ_n	9.5 km

Table 4.6: Experiments exploring the density in observational coverage but for the case of wind forcing).

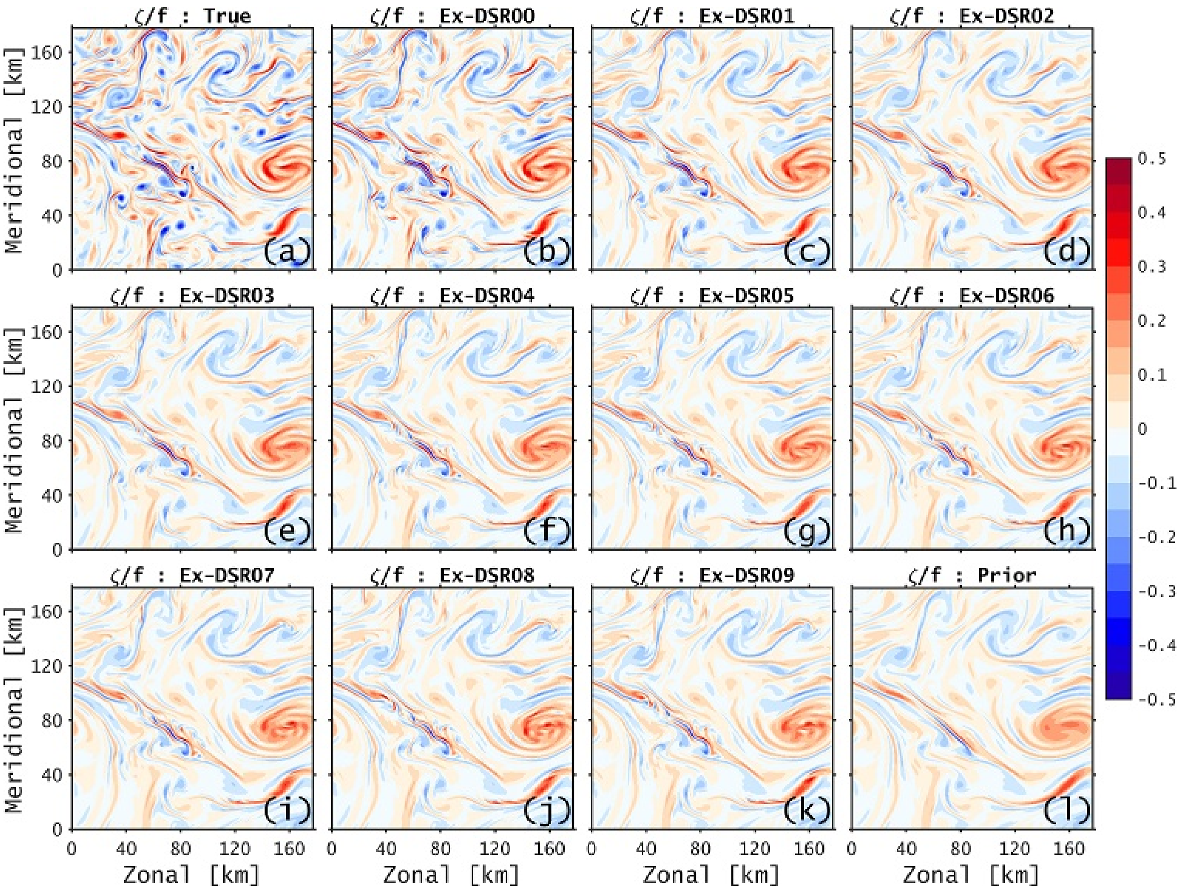

Figure 4.23: Comparison of surface ζ/f at T = 10 days for the "truth", in selected Ex-DSR (see Table 4.6) and in the "control" runs for the wind-forced case.

4.8 Summary and discussion

We used a fully eddy-resolving adjoint-based data assimilation model to explore the possibility of constraining the submesoscale variability of an idealized open-ocean surface-intensified turbulent flow by assimilating surface information only.

First, we demonstrated that velocity observations are not necessary to be assimilated, as the model could quickly derive the submesoscale currents by geostrophic adjustment from the constrained submesoscale temperature and salinity. Our experiments showed that by assimilating surface information only, it is possible to constrain the 3D structure of the submesoscale, that is, not only at the surface but also in the mixed layer, where submesoscale is active and significant. However, such constraining is not granted when introducing more surface information like SST and SSS. It might be because SST and SSS do not contain as much vertical information as SSH does.

With assimilated SSH alone, the "true" submesoscale flow, as well as the submesoscale temperature field, was retrieved. The model failed, however, to constrain the submesoscale salinity patterns. Assimilating additional SST did not improve salinity, and it was found that only after assimilating SSS did the salinity show correct submesoscale

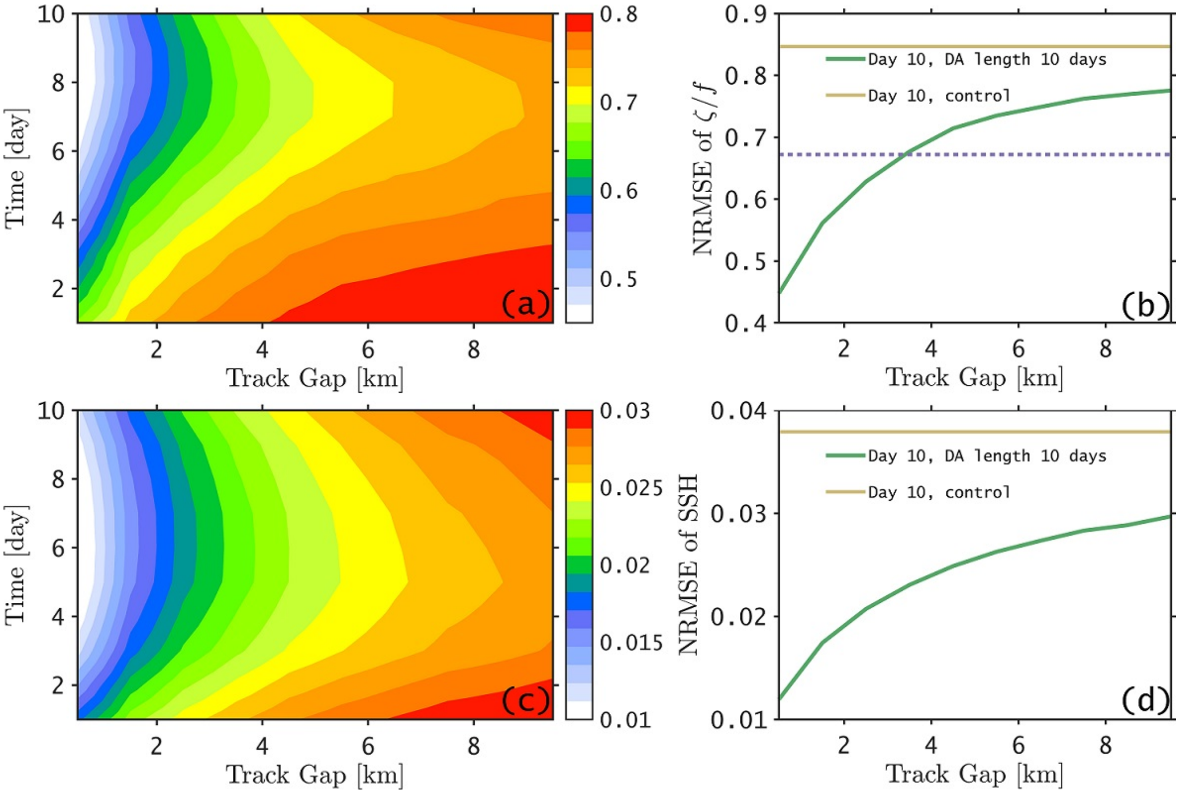

centring

Figure 4.24: (a) Temporal evolution of NRMSE of surface ζ/f as a function of observation ”track gap” distance for the experiments with assimilation window of 10 days. The NRMSE of surface ζ/f at day 10 for all experiments is shown in (b). The purple dashed line indicates a NRMSE 1.5 times larger than the minimum value with full observational resolution. (c) and (d) are the same as (a) and (b) but for SSH. These results correspond to the wind-forced case.

patterns.

A set of experiments was implemented to test the impact of the length of the assimilation window. A too-short assimilation window is insufficient to constrain the submesoscale, as it needs time to adjust and develop. But it is also not desirable to take a very long assimilation window, first due to computational reasons and second because highly nonlinear characteristics induce very limited predictability in the submesoscale. The predictability level of the submesoscale variations was found to be about 3∼4 days in our idealized experiment, which means that when there are no new observations assimilated into the model, the submesoscale could be kept constrained in the following 3∼4 days. By realizing this predictability, one may adjust and compromise the requirements from oceanic observational systems.

Next, we found that the success of constraining the submesoscale is highly reliant on the observations spatial resolutions. Higher-resolution contains more information, which is needed in the constraining process. However, large resolution in ocean measurements is still challenging for technical and economical reasons. Therefore, submesoscale observation projects have to find a compromise between the actual resolution need to study the highly dynamic process and what can be achieved with the technical solutions at hand. Our work explored the assimilation sensitivity to resolution and concluded that submesoscale-resolving observations are needed if the submesoscale activity is to be recovered.

Similar tests were then implemented to investigate the assimilation sensitivity to the observations temporal resolution. The results were more surprising than for the spatial resolution. The very high temporal resolution of observations is not necessarily positive for any specific temporal target because some information might be redundant. Indeed, in the fast-evolving submesoscale, too oft observations might interrupt the dynamic evolution of the instability processes leading to the ”correct” patterns.

We also tested the assimilation sensitivity to the observation random error. Observations with high random error failed to constrain the submesoscale, no matter how dense the observations are. The high stringent accuracy requirements for observations are dictated by the highly nonlinear nature of submesoscales.

Last, we tested the impact of increasing the submesoscale variability (i.e., taking initial conditions from the wind-forced case). More abundant submesoscales demand higher requirements regarding observations, i.e., denser spatial observations. This is not surprising since more sophisticated structures need more observations in order to reconstruct them.

Our experiments remained idealized by using a highly-turbulent flow. It should be stated that crucial to the success of constraining the submesoscale is the use of the variational approach (i.e., the adjoint method), which ensures the dynamical consistency between the data and the ocean physics. An ongoing extension of the present work will be to explore a realistic setting, where effects of bottom topography, more complex stratification and forcing variability are included.

Chapter 5

Conclusions and outlook

In this thesis, I have explored two aspects of the ocean submesoscale processes, namely 1) their impact on the kinetic energy conversion and 2) how to constrain their evolution in an eddy-resolving adjoint-based data assimilation model. The first aspect addresses the physical properties of ocean submesoscales, while the second focuses on the technical possibility to retrieve them based on ocean observations. Below I summarize the main conclusions reached in the present dissertation and outlook on possible extensions of this work.

5.1 Impact of the ocean submesoscale on kinetic energy conversion

Twin experiments, with and without wind stress forcing, were implemented and compared to determine the impact of the ocean submesoscale on the kinetic energy conversion. The forced case presents more abundant submesoscale features than the unforced case, and therefore the increased submesoscale is responsible for the time-integrated difference of kinetic energy conversion.

The layer integrated, time-averaged kinetic energy k_e was dramatically increased by nine times in the mixed layer and considerably in the pycnocline by the wind events. It shows that additional submesoscale brings increased kinetic energy. The velocity spectrum confirms that more kinetic energy is preserved in the wind forced case across the entire frequency and wavenumber bands.

The wind events changed the direction of the conversion between k_e and p_e. The total $C(P_e, K_e)$ was 5.85 MW in the no wind case, while it changed to -20.8 MW in the wind forced case. Although, in theory, the baroclinic instability was enhanced in the wind forced case (means more P_e is converted into K_e), the reverse sign ended due to the upwelling of denser water, which was induced by wind-forced submesoscale in the mixed layer.

The wind events also changed the direction of conversion between k_e and k_m. The total $C(K_m, K_e)$ was -4.76 MW in the no wind case while it increased to 3.3 MW in the wind forced case, revealing a considerable enhancement of barotropic instability. Such enhancement was mainly near the base of the mixed layer. The reversed direction was accounted by vertical velocity-related terms, i.e., term3 and term6 defined in Equation 3.10. The wind-induced submesoscales deepened the mixed layer and significantly promoted vertical mixing efficiency.

The wind events additionally excited inertial and superinertial motions in the interior. It was found that the inertial and superinertial motions dominated the transient conversion for both $C(P_e, K_e)$ and $C(K_m, K_e)$, while the sub-inertial motions dominated their time-averaged process. It is usually challenging to separate submesoscales from (super)inertial motions because of their similar spatial-temporal scales, so we should be careful in identifying the impacts of submesoscales and that of (super)inertial motions.

Cyclonic and anticyclonic eddies and filaments played different roles in kinetic energy conversion. In the no-wind case, cyclonic eddies had a stronger capacity to contain kinetic energy. They preserved about 50% more K_e than anticyclonic eddies and 1/3 more than filaments per unit volume. The cyclonic eddies were also found to be a bit more efficient to convert P_e to K_e and K_e to K_m. Interestingly, however, the wind events resulted in different behaviours. There was no significant difference regarding the capacity of containing K_e or P_e between the three components. But the clockwise-rotating winds dramatically enhanced the $C(P_e, K_e)$ and $C(K_m, K_e)$ in anticyclonic eddies.

5.2 Sensitivity of constraining the submesoscale from observations

In the second part of the present study, a series of assimilation experiments were performed to explore the possibility of constraining submesoscale features (1∼10 km) using an adjoint-based data assimilation model. The submesoscale variations (of scales less than 10 km) were first removed and then tried to be reconstructed by assimilating surface observations.

Assimilating SSH allowed reconstructing the submesoscale flow fields at the surface and in the mixed layer, where submesoscales are significant. It could also additionally reconstruct the submesoscale temperature field at the surface. It failed, however, to reconstruct the submesoscale temperature fields in deeper layers and submesoscale salinity fields at all depths. Furthermore, it was pointed out that one can assimilate SSS to reconstruct the submesoscale salinity field.

The predictability of submesoscales was found to be approximate 3∼4 days in the idealized experiments, which means that if no observations would be further involved, the submesoscale would only stay close to the ”true” state for 3∼4 days.

The assimilation effect was found to be sensitive to the spatial resolution of observations. Spatially denser observations always led to a better recovery of the submesoscale. However, the assimilation results were not so sensitive to the temporal resolution of observations, primarily due to the requiring time for the adjustment process from the initial state. The success of assimilation was highly dependent on the accuracy of observations. Stringent accuracy of observations was the key to constraining the submesoscale correctly. Finally, increasing the submesoscale activity level requires stricter requirements regarding the spatial resolution and accuracy of observations.

An important final conclusion of this study is that constraining the mesoscale to a high degree of realism is not sufficient for the submesoscale constraining process, since, with the ”correct” background, the submesoscale activity can still evolve in a different way simply based on the dynamics which are of a chaotic nature. This implies the need for observational system requirements to fully resolve the submesoscale.

5.3 Outlook

There is increasing awareness that oceanic submesoscales play a significant role in global climate change and ocean energy balance. On the one hand, the enormous developments of supercomputers and high-resolutions ocean models have made it possible to implement a few pioneer high-resolution global simulations to simulate the real oceanic submesoscales in a global sense. On the other hand, some new satellite platforms are planned to acquire ocean surface observations of ever-higher resolutions (e.g., SWOT and OSCOM), offering numerous opportunities to explore the real ocean submesoscale.

Both parts of this work are based on a highly idealized model, and many assumptions have been introduced, e.g., f-plane, double-periodic open boundary and free-slip bottom boundary conditions. Therefore a more realistic setting should be followed to see if all findings still preserve. Such a realistic setting may consider the actual topography of an ocean basin and realistic high-frequency forcing.

In addition, a more ambitious study of the impact of ocean submesoscale on the kinetic energy could be implemented, simulating the global ocean at 1 km resolution and checking realistic cases of filaments and cyclonic-anticyclonic energy partitioning.

For the assimilation part, except for a more realistic setting of the domain, the background error covariance matrix ($\mathbf{B}$) and the model error should also be considered. In this work, $\mathbf{B}$ has been highly simplified and approximated. However, the actual assimilation system is highly dependent on the specification of $\mathbf{B}$. Moreover, numerical models are imperfect; their errors are expected to be especially important in the submesoscale range, where non-linearity is high, and the impact from processes occurring at even smaller scales is felt, which in turn relies on crude idealized parameterizations.

Appendices

A.1 Formulation of the 4DVAR method

The 4DVAR method is a method for seeking an initial condition such that the forecast fits the observations best within the assimilation window. The cost function used in the 4DVAR formalism can be derived directly from the Bayes' theorem (Massart and Fisher, 2020), which states that:

Given two events ψ and ϕ:

$$P(\psi|\phi) = \frac{P(\phi|\psi)P(\psi)}{P(\phi)} = \frac{P(\psi|\phi)P(\psi)}{\int P(\phi|\psi)P(\psi)\mathrm{d}\psi} \tag{A.1}$$

where

$P(\psi)$ = The probability of ψ occurring
$P(\phi)$ = The probability of ϕ occurring
$P(\psi|\phi)$ = The probability of ψ given ϕ
$P(\phi|\psi)$ = The probability of ϕ given ψ

Similarly, for three random variables ψ, ϕ and χ, for a given event χ, the joint probability for ψ and χ is noted as $P(\psi, \phi; \chi)$. The conditional probability of $P(\psi|\phi; \chi)$ could be written as

$$P(\psi|\phi; \chi) = \frac{P(\phi|\psi; \chi)P(\psi|\chi)}{\int P(\phi|\psi; \chi)P(\psi|\chi)\mathrm{d}\psi} \tag{A.2}$$

In the 4DVAR formulation, the initial state is $\mathbf{x_0}$, the observations are $\mathbf{y}$ and the background state is $\mathbf{x_b}$. To obtain $P(\mathbf{x_0}|\mathbf{y}; \mathbf{x_b})$:

$$P(\mathbf{x_0}|\mathbf{y}; \mathbf{x_b}) = C\ P(\mathbf{y}|\mathbf{x_0}; \mathbf{x_b})P(\mathbf{x_0}|\mathbf{x_b}), \tag{A.3}$$

where C is a normalization factor independent of $\mathbf{x_0}$ and $\mathbf{x_b}$.

The observation $\mathbf{y}$ include $K+1$ members from time t_0 to time t_k:

$$\mathbf{y} : \mathbf{y_0}, \mathbf{y_1}, ...\mathbf{y_K}.$$

Assuming $\mathbf{y_k}, \mathbf{k} = 0, 1, ..., K$ are independent of each other and only correlate to $\mathbf{x_k}$, which is the prediction at time t_k by the model with the initial condition $\mathbf{x_0}$:

$$\begin{aligned} \mathbf{x_k} &= \mathcal{M}_{t_0 \to t_k}(\mathbf{x_0}) \\ &= \mathcal{M}_{t_{k-1} \to t_k}(\mathbf{x_{k-1}}), \end{aligned} \tag{A.4}$$

where $\mathcal{M}_{t_0 \to t_k}(\mathbf{x_0})$ represents an integration of the forecast model from time t_0 to time $t_\mathbf{k}$ and $\mathcal{M}_{t_{k-1} \to t_k}(\mathbf{x_{k-1}})$ from time $t_\mathbf{k-1}$ to time $t_\mathbf{k}$.

Then $P(\mathbf{y}|\mathbf{x_0}; \mathbf{x_b})$ could be written as:

$$P(\mathbf{y}|\mathbf{x_0}; \mathbf{x_b}) = \prod_{k=0}^{k=K} P(\mathbf{y_k}|\mathbf{x_k}). \tag{A.5}$$

Hence

$$P(\mathbf{x_0}|\mathbf{y}; \mathbf{x_b}) \propto P(\mathbf{x_0}|\mathbf{x_b}) \prod_{k=0}^{k=K} P(\mathbf{y_k}|\mathbf{x_k}) \tag{A.6}$$

Assuming all above probability distributions are subject to a Gaussian distribution, then:

$$P(\mathbf{x_0}|\mathbf{y}; \mathbf{x_b}) \propto \exp(-\mathcal{J}(\mathbf{x_0})), \tag{A.7}$$

where

$$\mathcal{J}(\mathbf{x_0}) = \frac{1}{2}(\mathbf{x_0} - \mathbf{x_b})^{\mathrm{T}} \mathbf{B}^{-1} (\mathbf{x_0} - \mathbf{x_b}) + \frac{1}{2} \sum_{\mathbf{k}=1}^{K} [\mathbf{y_k} - \mathcal{G}_\mathbf{k}(\mathbf{x_0})]^{\mathrm{T}} \mathbf{R}_\mathbf{k}^{-1} [\mathbf{y_k} - \mathcal{G}_\mathbf{k}(\mathbf{x_0})]. \tag{A.8}$$

The problem now is switched to minimizing the cost function $\mathcal{J}(\mathbf{x_0})$. Here, $\mathcal{G}_\mathbf{k}$ is a generalized observation operator that combines the forward model $\mathcal{M}_{t_0 \to t_\mathbf{k}}(\mathbf{x_0})$ and the traditional observation operator $\mathcal{H}_\mathbf{k}$, transforming model variables to observed quantities and interpolating them spatially to observation locations. $\mathbf{B}$ is the background error covariance matrix and $\mathbf{R}$ is the observation error matrix (assume $\mathbf{R_k}$ are uncorrelated in time and therefore $\mathbf{R}$ is block diagonal).

Next, we minimize $\mathcal{J}(\mathbf{x_0})$ by taking the gradient:

$$\nabla\mathcal{J}(\mathbf{x_0}) = \mathbf{B}^{-1}(\mathbf{x_0} - \mathbf{x_b}) - \sum_{\mathbf{k}=1}^{K} \mathbf{G}_{\mathbf{k}}^{\mathrm{T}}\mathbf{R}_{\mathbf{k}}^{-1}[\mathbf{y_k} - \mathcal{G}_{\mathbf{k}}(\mathbf{x_0})], \tag{A.9}$$

where $\mathbf{G}_{\mathbf{k}}^{\mathrm{T}}$ is the Jacobian of $\mathcal{G}_{\mathbf{k}}$. Under the linear approximation of the observation operator $\mathcal{H}$ and linear approximation of $\mathcal{M}$, $\mathbf{G_k}$ is then written as:

$$\mathbf{G_k} = \mathbf{H_k}\mathbf{M}_{t_{\mathbf{k}-1}\rightarrow t_{\mathbf{k}}}\mathbf{M}_{t_{\mathbf{k}-2}\rightarrow t_{\mathbf{k}-1}}\cdots\mathbf{M}_{t_0\rightarrow t_1} \tag{A.10}$$

where $\mathbf{M}$ is the tangent linear model of $\mathcal{M}$, $\mathbf{H}$ is the linear observation operator of $\mathcal{H}$.

Hence,

$$\mathbf{G}_{\mathbf{k}}^{\mathrm{T}} = \mathbf{M}_{t_0\rightarrow t_1}^{\mathrm{T}}\mathbf{M}_{t_1\rightarrow t_2}^{\mathrm{T}}\cdots\mathbf{M}_{t_{\mathbf{k}-1}\rightarrow t_{\mathbf{k}}}^{\mathrm{T}}\mathbf{H}_{\mathbf{k}}^{\mathrm{T}} \tag{A.11}$$

where $\mathbf{M}^{\mathrm{T}}$ is called the adjoint model of $\mathcal{M}$.

A.2 Formulation of the adjoint model

The adjoint model is derived from the nonlinear numerical model $\mathcal{M}$ (Adcroft et al., 2019):

$$\mathbf{x_k} = \mathcal{M}(\mathbf{x}; t_0, t_{\mathbf{k}}) \tag{A.12}$$

The perturbation of $\mathbf{x_k}$ under the linear approximation of the model $\mathcal{M}$ is

$$\delta\mathbf{x_k} = \mathbf{M}(\mathbf{x}; t_0, t_{\mathbf{k}})\delta\mathbf{x}_0 \tag{A.13}$$

The cost function $\mathcal{J}$ can be expressed as

$$\mathcal{J} = \mathcal{J}(\mathbf{x_0}) = \sum_{\mathbf{k}=1}^{K} r_{\mathbf{k}}(\mathbf{x_k}) \tag{A.14}$$

where $\mathbf{x_k}$ is the model forecast at $t_{\mathbf{k}}$ obtained with $\mathcal{M}$ and $r_{\mathbf{k}}(\mathbf{x_k})$ is a scalar response function of $\mathbf{x_k}$.

The gradient of $\mathcal{J}$ is defined as:

$$\mathcal{J}(\mathbf{x_0} + \delta\mathbf{x_0}) = \underbrace{\langle\nabla_{\mathbf{x_0}}\mathcal{J}, \delta\mathbf{x_0}\rangle}_{\delta\mathcal{J}} + \mathcal{O}(\|\delta\mathbf{x_0}\|^2) \tag{A.15}$$

where $\langle\ ,\rangle$ represents the inner product and $\|\cdot\|$ is the $l1 - norm$.

Combining (A.14) and (A.15) gives:

$$\nabla_{\mathbf{x_0}}\mathcal{J} = \sum_{\mathbf{k}=1}^{K} \nabla_{\mathbf{x_0}} r_{\mathbf{k}}(\mathbf{x_k}) \tag{A.16}$$

The first order perturbation of $r_{\mathbf{k}}(\mathbf{x_k})$ is

$$\delta r_{\mathbf{k}} = \langle \frac{\partial r_{\mathbf{k}}}{\partial \mathbf{x_k}}, \delta \mathbf{x_k} \rangle \tag{A.17}$$

Taking (A.13) into (A.17):

$$\delta r_{\mathbf{k}} = \langle \frac{\partial r_{\mathbf{k}}}{\partial \mathbf{x_k}}, \mathbf{M}(\mathbf{x}; t_0, t_{\mathbf{k}}) \delta \mathbf{x}_0 \rangle = \langle \mathbf{M}^{\mathrm{T}}(\mathbf{x}; t_{\mathbf{k}}, t_0) \frac{\partial r_{\mathbf{k}}}{\partial \mathbf{x_k}}, \delta \mathbf{x}_0 \rangle \tag{A.18}$$

Note that the following relationship in the above derivation process $\langle \mathbf{x}, \mathbf{Ay} \rangle = \langle \mathbf{A}^{\mathrm{T}}\mathbf{x}, \mathbf{y} \rangle$ has been used, where $\mathbf{A}^{\mathrm{T}}$ is the transpose of $\mathbf{A}$.

According to the definition of the gradient (A.15):

$$\delta r_{\mathbf{k}} = \langle \nabla_{\mathbf{x_0}} r_{\mathbf{k}}, \delta \mathbf{x_0} \rangle \tag{A.19}$$

For the arbitrary $\delta \mathbf{x_0}$, comparing (A.18) and (A.19):

$$\nabla_{\mathbf{x_0}} r_{\mathbf{k}} = \mathbf{M}^{\mathrm{T}}(t_{\mathbf{k}}, t_0) \frac{\partial r_{\mathbf{k}}}{\partial \mathbf{x_k}} \tag{A.20}$$

and combining it with (A.16):

$$\nabla_{\mathbf{x_0}}\mathcal{J} = \sum_{\mathbf{k}=1}^{K} \mathbf{M}^{\mathrm{T}}(t_{\mathbf{k}}, t_0) \frac{\partial r_{\mathbf{k}}}{\partial \mathbf{x_k}} \tag{A.21}$$

where $\mathbf{M}^{\mathrm{T}}$ is the adjoint model.

A.3 Derivation of the kinetic energy balance equation

In order to derive the balance equation for the eddy kinetic energy (K_e), we start from the momentum primitive equations:

$$\frac{\mathrm{d}\mathbf{u}_h}{\mathrm{d}t} + f\mathbf{k} \times \mathbf{u}_h = -\frac{1}{\rho_o}\nabla_h p + \frac{\partial \tau}{\partial z}, \tag{A.22}$$

where $\frac{\mathrm{d}}{\mathrm{d}t} = \frac{\partial}{\partial t} + \mathbf{u}_h \cdot \nabla_h + w\frac{\partial}{\partial z}$, $\mathbf{u}_h = (u, v)$ is horizontal velocity vector, w is vertical velocity, $\nabla_h = (\partial/\partial x, \partial/\partial y)$, f is the Coriolis parameter, $\mathbf{k}$ is unit vertical vector, ρ_0 is reference density, p is pressure and $\tau = (\tau_x, \tau_y)$ is the vertical flux of horizontal momentum vector.

To obtain the balance equation of eddy kinetic energy k_e, we multiply the zonal and meridional components of (A.22) with u' and v', respectively:

$$
\begin{aligned}
u'\frac{\partial u}{\partial t} + u'u\frac{\partial u}{\partial x} + u'v\frac{\partial u}{\partial y} + u'w\frac{\partial u}{\partial z} - fvu' &= -\frac{u'}{\rho_o}\frac{\partial p}{\partial x} + u'\frac{\partial \tau_x}{\partial z}, && \text{(A.23)}\\
v'\frac{\partial v}{\partial t} + v'u\frac{\partial v}{\partial x} + v'v\frac{\partial v}{\partial y} + v'w\frac{\partial v}{\partial z} + fuv' &= -\frac{v'}{\rho_o}\frac{\partial p}{\partial y} + v'\frac{\partial \tau_y}{\partial z}. && \text{(A.24)}
\end{aligned}
$$

Denoting $\mathbf{u} = (\mathbf{u}_h, w)$, $\mathbf{u}^{'} = (\mathbf{u}_h', w')$, $\nabla = (\nabla_h, \partial/\partial z)$ and then taking an average of (A.23) and (A.24) gives:

$$
\begin{aligned}
\overline{u'\frac{\partial u'}{\partial t}} + \overline{u'\mathbf{u}} \cdot \nabla\overline{u} + \overline{\mathbf{u}} \cdot \nabla(\frac{1}{2}\overline{u'^2}) + \nabla \cdot (\frac{u'^2}{2}\mathbf{u}') - f\overline{v'u'} &= -\overline{\frac{u'}{\rho_0}\frac{\partial p'}{\partial x}} + \overline{u'\frac{\partial \tau_x'}{\partial z}}, && \text{(A.25)}\\
\overline{v'\frac{\partial v'}{\partial t}} + \overline{v'\mathbf{u}} \cdot \nabla\overline{v} + \overline{\mathbf{u}} \cdot \nabla(\frac{1}{2}\overline{v'^2}) + \nabla \cdot (\frac{v'^2}{2}\mathbf{u}') + f\overline{u'v'} &= -\overline{\frac{v'}{\rho_0}\frac{\partial p'}{\partial y}} + \overline{v'\frac{\partial \tau_y'}{\partial z}}. && \text{(A.26)}
\end{aligned}
$$

In the averaging process, the Reynolds condition: $\overline{ab} = \overline{a}\overline{b} + \overline{a'b'}$, for $a = \overline{a} + a', b = \overline{b} + b'$, has been used. Multiplying (A.25) and (A.26) with ρ_0 and summing them up and after combining with the hydrostatic equation:

$$
\frac{\partial p}{\partial z} = -g\rho, \tag{A.27}
$$

we obtain:

$$
\begin{aligned}
&\frac{\partial k_e}{\partial t} + \nabla \cdot (k_e\overline{\mathbf{u}}) + \nabla \cdot [\frac{\rho_0}{2}\mathbf{u}'(u'^2 + v'^2)] + \nabla \cdot \overline{p'\mathbf{u}'}\\
&= -\rho_0\overline{u'\mathbf{u}} \cdot \nabla\overline{u} - \rho_0\overline{v'\mathbf{u}} \cdot \nabla\overline{v} - g\overline{\rho'w'} + \frac{\partial}{\partial z}[\rho_0(\overline{\tau_x'u'} + \overline{\tau_y'v'})] - \epsilon(k_e),
\end{aligned}
\tag{A.28}
$$

where $k_e = \frac{1}{2}\rho_0(\overline{u'^2 + v'^2})$ and $\epsilon(k_e) = \rho_0(\overline{\tau_x'\frac{\partial u'}{\partial z}} + \overline{\tau_y'\frac{\partial v'}{\partial z}})$. Note that the continuity condition $(\nabla \cdot \mathbf{u} = 0)$ in the above derivation has been applied.

Integrating (A.28) over the entire ocean, the volume integral of the nabla-terms on the lhs vanish, giving:

$$\frac{\mathrm{d}K_e}{\mathrm{d}t} = C(K_m, K_e) + C(P_e, K_e) + G(K_e) - D(K_e), \tag{A.29}$$

$$C(K_m, K_e) = -\int_V (\rho_0 \overline{u'\mathbf{u}} \cdot \nabla \overline{u} + \rho_0 \overline{v'\mathbf{u}} \cdot \nabla \overline{v}) \mathrm{d}V, \tag{A.30}$$

$$C(P_e, K_e) = -\int_V g \overline{\rho' w'} \mathrm{d}V, \tag{A.31}$$

$$G(K_e) = \int_S \rho_0 (\overline{\tau'_{x,S} u'} + \overline{\tau'_{y,S} v'}) \mathrm{d}S, \tag{A.32}$$

$$D(K_e) = \int_V \epsilon(k_e) \mathrm{d}V, \tag{A.33}$$

where $\tau_{x,S}$ and $\tau_{y,S}$ denote the stress on the ocean surface by the interaction with the atmosphere.

References

Adcroft, A., Campin, J.-M., Doddridge, E., Dutkiewicz, S., Evangelinos, C., Ferreira, D., Follows, M., Forget, G., Fox-Kemper, B., Heimbach, P., Chris Hill, E. H., Hill, H., Jahn, O., Klymak, J., Losch, M., Marshall, J., Maze, G., Mazloff, M., Menemenlis, D., Molod, A., and Scott, J. (2019). *MITgcm Document.*

Argo (2020). *Argo float data and metadata from Global Data Assembly Centre (Argo GDAC).* SEANOE.

Ashkenazy, Y. and Tziperman, E. (2016). Variability, instabilities, and eddies in a snowball ocean. *Journal of Climate*, 29(2):869–888.

Bachman, S. D., Taylor, J. R., Adams, K. A., and Hosegood, P. J. (2017). Mesoscale and submesoscale effects on mixed layer depth in the southern ocean. *Journal of Physical Oceanography*, 47(9):2173–2188.

Barkan, R., Winters, K. B., and Smith, S. G. L. (2015). Energy cascades and loss of balance in a reentrant channel forced by wind stress and buoyancy fluxes. *Journal of Physical Oceanography*, 45(1):272–293.

Barker, D. M., Huang, W., Guo, Y. R., Bourgeois, A. J., and Xiao, Q. N. (2004). A three-dimensional variational data assimilation system for mm5: Implementation and initial results. *Monthly Weather Review*, 132(4):897–914.

Bleck, R. (1985). On the conversion between mean and eddy components of potential and kinetic-energy in isentropic and isopycnic coordinates. *Dynamics of Atmospheres and Oceans*, 9(1):17–37.

Boas, A. B. V., Cornuelle, B. D., Mazloff, M. R., Gille, S. T., and Ardhuin, F. (2020). Wave-current interactions at meso- and submesoscales: Insights from idealized numerical simulations. *Journal of Physical Oceanography*, 50(12):3483–3500.

Boutin, J., Martin, N., Reverdin, G., Yin, X., and Gaillard, F. (2013). Sea surface freshening inferred from smos and argo salinity: impact of rain. *Ocean Science*, 9(1):183–192.

Bouttier, F. and Courtier, P. (1999). *Data assimilation concepts and methods.* Meteorological Training Course Lecture Series. ECMWF.

Bracco, A., Liu, G. P., and Sun, D. X. (2019). Mesoscale-submesoscale interactions in the gulf of mexico: From oil dispersion to climate. *Chaos Solitons & Fractals*, 119:63–72.

Buckingham, C. E., Garabato, A. C. N., Thompson, A. F., Brannigan, L., Lazar, A., Marshall, D. P., Nurser, A. J. G., Damerell, G., Heywood, K. J., and Belcher, S. E. (2016). Seasonality of submesoscale flows in the ocean surface boundary layer. *Geophysical Research Letters*, 43(5):2118–2126.

Bucy, R. S. and Joseph, P. D. (1968). *Filtering for stochastic processes with applications to guidance.* Interscience tracts in pure and applied mathematics, no. 23. New York, Interscience Publishers.

Callies, J. and Ferrari, R. (2013). Interpreting energy and tracer spectra of upper-ocean turbulence in the submesoscale range (1-200 km). *Journal of Physical Oceanography*, 43(11):2456–2474.

Callies, J., Flierl, G., Ferrari, R., and Fox-Kemper, B. (2016). The role of mixed-layer instabilities in submesoscale turbulence. *Journal of Fluid Mechanics*, 788:5–41.

Capet, X., McWilliams, J. C., Molemaker, M. J., and Shchepetkin, A. F. (2008a). Mesoscale to submesoscale transition in the california current system. part i: Flow structure, eddy flux, and observational tests. *Journal of Physical Oceanography*, 38(1):29–43.

Capet, X., McWilliams, J. C., Molemaker, M. J., and Shchepetkin, A. F. (2008b). Mesoscale to submesoscale transition in the california current system. part iii: Energy balance and flux. *Journal of Physical Oceanography*, 38(10):2256–2269.

Carpenter, J. R., Rodrigues, A., Schultze, L. K. P., Merckelbach, L. M., Suzuki, N., Baschek, B., and Umlauf, L. (2020). Shear instability and turbulence within a submesoscale front following a storm. *Geophysical Research Letters*, 47(23).

Carton, J. A., Chepurin, G., Cao, X. H., and Giese, B. (2000). A simple ocean data assimilation analysis of the global upper ocean 1950-95. part i: Methodology. *Journal of Physical Oceanography*, 30(2):294–309.

Carton, J. A. and Giese, B. S. (2008). A reanalysis of ocean climate using simple ocean data assimilation (soda). *Monthly Weather Review*, 136(8):2999–3017.

Chavanne, C. P. and Klein, P. (2010). Can oceanic submesoscale processes be observed with satellite altimetry? *Geophysical Research Letters*, 37(22):n/a–n/a.

Chelton, D. B., Schlax, M. G., and Samelson, R. M. (2011). Global observations of nonlinear mesoscale eddies. *Progress in Oceanography*, 91(2):167–216.

Chen, R., Thompson, A. F., and Flierl, G. R. (2016). Time-dependent eddy-mean energy diagrams and their application to the ocean. *Journal of Physical Oceanography*, 46(9):2827–2850.

Chrysagi, E., Umlauf, L., Holtermann, P., Klingbeil, K., and Burchard, H. (2021). High-resolution simulations of submesoscale processes in the baltic sea: The role of storm events. *Journal of Geophysical Research-Oceans*, 126(3).

Courtier, P., Andersson, E., Heckley, W., Pailleux, J., Vasiljevic, D., Hamrud, M., Hollingsworth, A., Rabier, E., and Fisher, M. (1998). The ecmwf implementation of three-dimensional variational assimilation (3d-var). i: Formulation. *Quarterly Journal of the Royal Meteorological Society*, 124(550):1783–1807.

Couvelard, X., Dumas, F., Garnier, V., Ponte, A. L., Talandier, C., and Treguier, A. M. (2015). Mixed layer formation and restratification in presence of mesoscale and submesoscale turbulence. *Ocean Modelling*, 96:243–253.

Cressman, G. P. (1959). An operational objective analysis system. *Monthly Weather Review*, 87(10):367–374.

Cummings, J. A. (2005). Operational multivariate ocean data assimilation. *Quarterly Journal of the Royal Meteorological Society*, 131(613):3583–3604.

Cummings, J. A. and Smedstad, O. M. (2013). *Variational Data Assimilation for the Global Ocean*, pages 303–343. Springer Berlin Heidelberg, Berlin, Heidelberg.

Dauhajre, D. P., McWilliams, J. C., and Uchiyama, Y. (2017). Submesoscale coherent structures on the continental shelf. *Journal of Physical Oceanography*, 47(12):2949–2976.

Derber, J. and Bouttier, F. (1999). A reformulation of the background error covariance in the ecmwf global data assimilation system. *Tellus Series a-Dynamic Meteorology and Oceanography*, 51(2):195–221.

Drucker, R. and Riser, S. C. (2014). Validation of aquarius sea surface salinity with argo: Analysis of error due to depth of measurement and vertical salinity stratification. *Journal of Geophysical Research: Oceans*, 119(7):4626–4637.

Du, Y., Dong, X., Jiang, X., Zhang, Y., Zhu, D., Sun, Q., Wang, Z., Niu, X., Chen, W., Zhu, C., Jing, Z., Tang, S., Li, Y., Chen, J., Chu, X., Xu, C., Wang, T., He, Y., Han, B., Zhang, Y., Wang, M., Wu, W., Xia, Y., Chen, K., Qian, Y.-K., Shi, P., Zhan, H., and Peng, S. (2021). Ocean surface current multiscale observation mission (oscom): Simultaneous measurement of ocean surface current, vector wind, and temperature. *Progress in Oceanography*, 193.

Evensen, G. (1994). Sequential data assimilation with a nonlinear quasi-geostrophic model using monte carlo methods to forecast error statistics. *Journal of Geophysical Research*, 99(C5).

Ferrari, R. and Wunsch, C. (2010). The distribution of eddy kinetic and potential energies in the global ocean. *Tellus A*, 62(2):92–108.

Fu, L.-L. and Ferrari, R. (2008). Observing oceanic submesoscale processes from space. *Eos, Transactions American Geophysical Union*, 89(48):488–488.

Galperin, B., Sukoriansky, S., and Qiu, B. (2021). Seasonal oceanic variability on meso- and submesoscales: a turbulence perspective. *Ocean Dynamics*, 71(4):475–489.

Gandin, L. S. (1965). Objective analysis of meteorological fields. *Translated from the Russian. Jerusalem (Israel Program for Scientific Translations)*, page 242.

Ghil, M. and Malanotte-Rizzoli, P. (1991). *Data Assimilation in Meteorology and Oceanography*, pages 141–266. Advances in Geophysics.

Giering, R. and Kaminski, T. (1998). Recipes for adjoint code construction. *Acm Transactions on Mathematical Software*, 24(4):437–474.

Gilbert, J. C. and Lemaréchal, C. (1989). Some numerical experiments with variable-storage quasi-newton algorithms. *Mathematical Programming*, 45:407–435.

Gilchrist, B. and Cressman, G. P. (1954). An experiment in objective analysis. *Tellus*, 6(4):309–318.

Gula, J., Molemaker, M. J., and McWilliams, J. C. (2016). Topographic generation of submesoscale centrifugal instability and energy dissipation. *Nat Commun*, 7:12811.

Hughes, C. W. and Wilson, C. (2008). Wind work on the geostrophic ocean circulation: An observational study of the effect of small scales in the wind stress. *Journal of Geophysical Research-Oceans*, 113(C2).

Isern-Fontanet, J., Chapron, B., Lapeyre, G., and Klein, P. (2006). Potential use of microwave sea surface temperatures for the estimation of ocean currents. *Geophysical Research Letters*, 33(24).

Jensen, T. G., Shulman, I., Wijesekera, H. W., Anderson, S., and Ladner, S. (2018). Submesoscale features and their interaction with fronts and internal tides in a high-resolution coupled atmosphere-ocean-wave model of the bay of bengal. *Ocean Dynamics*, 68(3):391–410.

Jüling, A., Viebahn, J. P., Drijfhout, S. S., and Dijkstra, H. A. (2018). Energetics of the southern ocean mode. *Journal of Geophysical Research-Oceans*, 123(12):9283–9304.

Kalman, R. E. (1960). A new approach to linear filtering and prediction problems. *Journal of Basic Engineering*, 82(1):35–45.

Kao, J., Flicker, D., Henninger, R., Frey, S., Ghil, M., and Ide, K. (2004). Data assimilation with an extended kalman filter for impact-produced shock-wave dynamics. *Journal of Computational Physics*, 196(2):705–723.

Korotaev, G., Huot, E., Ledimet, F., Herlin, I., Stanichny, S., Solovyev, D., and Wu, L. (2008). Retrieving ocean surface current by 4-d variational assimilation of sea surface temperature images. *Remote Sensing of Environment*, 112(4):1464–1475.

Kozlov, I. E., Plotnikov, E. V., and Manucharyan, G. E. (2020). Brief communication: Mesoscale and submesoscale dynamics in the marginal ice zone from sequential synthetic aperture radar observations. *Cryosphere*, 14(9):2941–2947.

Köhl, A. (2020). Evaluating the gecco3 1948–2018 ocean synthesis − a configuration for initializing the mpi-esm climate model. *Quarterly Journal of the Royal Meteorological Society*, 146(730):2250–2273.

LaCasce, J. H. and Mahadevan, A. (2006). Estimating subsurface horizontal and vertical velocities from sea-surface temperature. *Journal of Marine Research*, 64(5):695–721.

Lapeyre, G. and Klein, P. (2006). Dynamics of the upper oceanic layers in terms of surface quasigeostrophy theory. *Journal of Physical Oceanography*, 36(2):165–176.

Lapeyre, G., Klein, P., and Hua, B. L. (2006). Oceanic restratification forced by surface frontogenesis. *Journal of Physical Oceanography*, 36(8):1577–1590.

Large, W. G., Mcwilliams, J. C., and Doney, S. C. (1994). Oceanic vertical mixing - a review and a model with a nonlocal boundary-layer parameterization. *Reviews of Geophysics*, 32(4):363–403.

Le Vine, D. M., Dinnat, E. P., Meissner, T., Yueh, S. H., Wentz, F. J., Torrusio, S. E., and Lagerloef, G. (2015). Status of aquarius/sac-d and aquarius salinity retrievals. *IEEE Journal of Selected Topics in Applied Earth Observations and Remote Sensing*, 8(12):5401–5415.

Le Vine, D. M., Lagerloef, G. S. E., and Torrusio, S. E. (2010). Aquarius and remote sensing of sea surface salinity from space. *Proceedings of the IEEE*, 98(5):688–703.

Lindskog, M., Salonen, K., Jarvinen, H., and Michelson, D. B. (2004). Doppler radar wind data assimilation with hirlam 3dvar. *Monthly Weather Review*, 132(5):1081–1092.

Lorenz, E. N. (1955). Available potential energy and the maintenance of the general circulation. *Tellus*, 7(2):157–167.

Lyu, G. (2017). *Calibrating an earth system model using the adjoint method.* PhD thesis, Universität Hamburg, Hamburg.

Marshall, J., Hill, C., Perelman, L., and Adcroft, A. (1997). Hydrostatic, quasi-hydrostatic, and nonhydrostatic ocean modeling. *Journal of Geophysical Research-Oceans*, 102(C3):5733–5752.

Massart, S. and Fisher, M. (2020). Assimilation algorithms lecture 3: 4D-Var. Retrieved from https://events.ecmwf.int/event/153/contributions/904/.

McAvaney, B. J. and Holland, G. J. (1995). *Dynamics of future climates*, pages 281–314. World Survey of Climatology.

McDougall, T. J. (1987). Neutral surfaces. *Journal of Physical Oceanography*, 17(11):1950–1964.

McWilliams, J. C. (2008). Fluid dynamics at the margin of rotational control. *Environmental Fluid Mechanics*, 8(5-6):441–449.

McWilliams, J. C. (2016). Submesoscale currents in the ocean. *Proc Math Phys Eng Sci*, 472(2189):20160117.

McWilliams, J. C. (2019). A survey of submesoscale currents. *Geoscience Letters*, 6(1).

McWilliams, J. C. and Molemaker, M. J. (2011). Baroclinic frontal arrest: A sequel to unstable frontogenesis. *Journal of Physical Oceanography*, 41(3):601–619.

Mensa, J. A., Garraffo, Z., Griffa, A., Ozgokmen, T. M., Haza, A., and Veneziani, M. (2013). Seasonality of the submesoscale dynamics in the gulf stream region. *Ocean Dynamics*, 63(8):923–941.

Meroni, A. N., Miller, M. D., Tziperman, E., and Pasquero, C. (2017). Nonlinear energy transfer among ocean internal waves in the wake of a moving cyclone. *Journal of Physical Oceanography*, 47(8):1961–1980.

Molemaker, M. J., McWilliams, J. C., and Capet, X. (2010). Balanced and unbalanced routes to dissipation in an equilibrated eady flow. *Journal of Fluid Mechanics*, 654:35–63.

Molemaker, M. J., McWilliams, J. C., and Dewar, W. K. (2015). Submesoscale instability and generation of mesoscale anticyclones near a separation of the california undercurrent. *Journal of Physical Oceanography*, 45(3):613–629.

Mukherjee, S., Ramachandran, S., Tandon, A., and Mahadevan, A. (2016). Production and destruction of eddy kinetic energy in forced submesoscale eddy-resolving simulations. *Ocean Modelling*, 105:44–59.

Niwa, Y. and Hibiya, T. (1997). Nonlinear processes of energy transfer from traveling hurricanes to the deep ocean internal wave field. *Journal of Geophysical Research-Oceans*, 102(C6):12469–12477.

Olbers, D., Willebrand, J., and Eden, C. (2012). *Ocean Dynamics*. Springer-Verlag Berlin Heidelberg.

O'Carroll, A. G., Armstrong, E. M., Beggs, H. M., Bouali, M., Casey, K. S., Corlett, G. K., Dash, P., Donlon, C. J., Gentemann, C. L., Høyer, J. L., Ignatov, A., Kabobah, K., Kachi, M., Kurihara, Y., Karagali, I., Maturi, E., Merchant, C. J., Marullo, S., Minnett, P. J., Pennybacker, M., Ramakrishnan, B., Ramsankaran, R., Santoleri, R., Sunder, S., Saux Picart, S., Vázquez-Cuervo, J., and Wimmer, W. (2019). Observational needs of sea surface temperature. *Frontiers in Marine Science*, 6.

Panofsky, H. A. (1949). Objective weather-map analysis. *Journal of Meteorology*, 6(6):386–392.

Pedlosky, J. (1987). *Geophysical Fluid Dynamics*. Springer, New York, NY, 2nd edition.

Poje, A. C., Ozgokmen, T. M., Lipphardt, B. L., J., Haus, B. K., Ryan, E. H., Haza, A. C., Jacobs, G. A., Reniers, A. J., Olascoaga, M. J., Novelli, G., Griffa, A., Beron-Vera, F. J., Chen, S. S., Coelho, E., Hogan, P. J., Kirwan, A. D., J., Huntley, H. S., and Mariano, A. J. (2014). Submesoscale dispersion in the vicinity of the deepwater horizon spill. *Proc Natl Acad Sci U S A*, 111(35):12693–8.

Qiu, B., Chen, S. M., Klein, P., Wang, J. B., Torres, H., Fu, L. L., and Menemenlis, D. (2018). Seasonality in transition scale from balanced to unbalanced motions in the world ocean. *Journal of Physical Oceanography*, 48(3):591–605.

Reul, N., Fournier, S., Boutin, J., Hernandez, O., Maes, C., Chapron, B., Alory, G., Quilfen, Y., Tenerelli, J., Morisset, S., Kerr, Y., Mecklenburg, S., and Delwart, S. (2013). Sea surface salinity observations from space with the smos satellite: A new means to monitor the marine branch of the water cycle. *Surveys in Geophysics*, 35(3):681–722.

Richardson, L. F. (1922). *Weather prediction by numerical process*. Cambridge (University Press).

Rocha, C. B., Chereskin, T. K., Gille, S. T., and Menemenlis, D. (2016a). Mesoscale to submesoscale wavenumber spectra in drake passage. *Journal of Physical Oceanography*, 46(2):601–620.

Rocha, C. B., Gille, S. T., Chereskin, T. K., and Menemenlis, D. (2016b). Seasonality of submesoscale dynamics in the kuroshio extension. *Geophysical Research Letters*, 43(21):11304–11311.

Roullet, G., McWilliams, J. C., Capet, X., and Molemaker, M. J. (2012). Properties of steady geostrophic turbulence with isopycnal outcropping. *Journal of Physical Oceanography*, 42(1):18–38.

Sasaki, Y. (1958). An objective analysis based on the variational method. *Journal of the Meteorological Society of Japan. Ser. II*, 36(3):77–88.

Schubert, R., Schwarzkopf, F. U., Baschek, B., and Biastoch, A. (2019). Submesoscale impacts on mesoscale agulhas dynamics. *Journal of Advances in Modeling Earth Systems*, 11(8):2745–2767.

Shcherbina, A. Y., D'Asaro, E. A., Lee, C. M., Klymak, J. M., Molemaker, M. J., and McWilliams, J. C. (2013). Statistics of vertical vorticity, divergence, and strain in a developed submesoscale turbulence field. *Geophysical Research Letters*, 40(17):4706–4711.

Shcherbina, A. Y., Sundermeyer, M. A., Kunze, E., D'Asaro, E., Badin, G., Birch, D., Brunner-Suzuki, A. M. E. G., Callies, J., Cervantes, B. T. K., Claret, M., Concannon, B., Early, J., Ferrari, R., Goodman, L., Harcourt, R. R., Klymak, J. M., Lee, C. M., Lelong, M. P., Levine, M. D., Lien, R. C., Mahadevan, A., McWilliams, J. C., Molemaker, M. J., Mukherjee, S., Nash, J. D., Ozgokmen, T., Pierce, S. D., Ramachandran, S., Samelson, R. M., Sanford, T. B., Shearman, R. K., Skyllingstad, E. D., Smith, K. S., Tandon, A., Taylor, J. R., Terray, E. A., Thomas, L. N., and Ledwell, J. R. (2015). The latmix summer campaign: Submesoscale stirring in the upper ocean. *Bulletin of the American Meteorological Society*, 96(8).

Siegelman, L. (2020). Energetic submesoscale dynamics in the ocean interior. *Journal of Physical Oceanography*, 50(3):727–749.

Siegelman, L., O'Toole, M., Flexas, M., Riviere, P., and Klein, P. (2019). Submesoscale ocean fronts act as biological hotspot for southern elephant seal. *Scientific Reports*, 9.

Srinivasan, K., Mcwilliams, J. C., Molemaker, M. J., and Barkan, R. (2019). Submesoscale vortical wakes in the lee of topography. *Journal of Physical Oceanography*, 49(7):1949–1971.

Stammer, D., Wunsch, C., Giering, R., Eckert, C., Heimbach, P., Marotzke, J., Adcroft, A., Hill, C. N., and Marshall, J. (2002). Global ocean circulation during 1992-1997, estimated from ocean observations and a general circulation model. *Journal of Geophysical Research-Oceans*, 107(C9).

Su, Z., Torres, H., Klein, P., Thompson, A. F., Siegelman, L., Wang, J. B., Menemenlis, D., and Hill, C. (2020). High-frequency submesoscale motions enhance the upward vertical heat transport in the global ocean. *Journal of Geophysical Research-Oceans*, 125(9).

Su, Z., Wang, J., Klein, P., Thompson, A. F., and Menemenlis, D. (2018). Ocean submesoscales as a key component of the global heat budget. *Nat Commun*, 9(1):775.

Tang, Y., Kleeman, R., and Moore, A. M. (2004). Sst assimilation experiments in a tropical pacific ocean model. *Journal of Physical Oceanography*, 34(3):623–642.

Taylor, J. R., Smith, K. M., and Vreugdenhil, C. A. (2020). The influence of submesoscales and vertical mixing on the export of sinking tracers in large-eddy simulations. *Journal of Physical Oceanography*, 50(5):1319–1339.

Vallis, G. K. (2017). *Atmospheric and Oceanic Fluid Dynamics: Fundamentals and Large-Scale Circulation*. Cambridge University Press, Cambridge, 2nd edition.

Van Leeuwen, P. J., Cheng, Y., and Reich, S. (2015). *Nonlinear Data Assimilation*. Frontiers in Applied Dynamical Systems: Reviews and Tutorials.

von Storch, J. S., Eden, C., Fast, I., Haak, H., Hernandez-Deckers, D., Maier-Reimer, E., Marotzke, J., and Stammer, D. (2012). An estimate of the lorenz energy cycle for the world ocean based on the 1/10 degrees storm/ncep simulation. *Journal of Physical Oceanography*, 42(12):2185–2205.

Wang, D. P. and Jordi, A. (2011). Surface frontogenesis and thermohaline intrusion in a shelfbreak front. *Ocean Modelling*, 38(1-2):161–170.

Wang, P., Zhu, M., Chen, Y., and Zhang, W. (2020). Implicit equal-weights variational particle smoother. *Atmosphere*, 11(4).

Wang, Z. F., Li, Q. Y., Sun, L., Li, S., Yang, Y. J., and Liu, S. S. (2015). The most typical shape of oceanic mesoscale eddies from global satellite sea level observations. *Frontiers of Earth Science*, 9(2):202–208.

Whitt, D. B., Levy, M., and Taylor, J. R. (2019). Submesoscales enhance storm-driven vertical mixing of nutrients: Insights from a biogeochemical large eddy simulation. *Journal of Geophysical Research-Oceans*, 124(11):8140–8165.

Whitt, D. B., Thomas, L. N., Klymak, J. M., Lee, C. M., and D'Asaro, E. A. (2018). Interaction of superinertial waves with submesoscale cyclonic filaments in the north wall of the gulf stream. *Journal of Physical Oceanography*, 48(1):81–99.

Wu, Y., Wang, Z., and Liu, C. (2017). On the response of the lorenz energy cycle for the southern ocean to intensified westerlies. *Journal of Geophysical Research: Oceans*, 122(3):2465–2493.

Zatsepin, A., Kubryakov, A., Aleskerova, A., Elkin, D., and Kukleva, O. (2019). Physical mechanisms of submesoscale eddies generation: evidences from laboratory modeling and satellite data in the black sea. *Ocean Dynamics*, 69(2):253–266.

Zemskova, V. E., White, B. L., and Scotti, A. (2015). Available potential energy and the general circulation: Partitioning wind, buoyancy forcing, and diapycnal mixing. *Journal of Physical Oceanography*, 45(6):1510–1531.

Zhang, Z. and Qiu, B. (2018). Evolution of submesoscale ageostrophic motions through the life cycle of oceanic mesoscale eddies. *Geophysical Research Letters*, 45(21):11847–11855.

Zhang, Z., Wang, W., and Qiu, B. (2014). Oceanic mass transport by mesoscale eddies. *Science*, 345(6194):322–4.

Zhang, Z. W., Zhang, X. C., Qiu, B., Zhao, W., Zhou, C., Huang, X. D., and Tian, J. W. (2021). Submesoscale currents in the subtropical upper ocean observed by long-term high-resolution mooring arrays. *Journal of Physical Oceanography*, 51(1):187–206.

Zhang, Z. W., Zhang, Y. C., Qiu, B., Sasaki, H., Sun, Z. B., Zhang, X. C., Zhao, W., and Tian, J. W. (2020). Spatiotemporal characteristics and generation mechanisms of submesoscale currents in the northeastern south china sea revealed by numerical simulations. *Journal of Geophysical Research-Oceans*, 125(2).

Zhu, M., van Leeuwen, P. J., and Amezcua, J. (2016). Implicit equal-weights particle filter. *Quarterly Journal of the Royal Meteorological Society*, 142(698):1904–1919.

Acronyms

ACC	Antarctic Circumpolar Current
AVISO	Archiving Validation and Interpretation of Satellite Oceanographic data
CEOS SST-VC	CEOS SST Virtual Constellation
CTD	Conductivity Temperature Depth
EnKF	Ensemble Kalman Filter
EKF	Extended Kalman Filter
ESA	European Space Agency
GHRSST	Group for High Resolution Sea Surface Temperature
HYCOM	Hybrid Coordinate Ocean Model
K_e	Eddy Kinetic Energy
KF	Kalman Filter
K_m	Mean Kinetic Energy
KPP	K-profile parameterization
LEC	Lorenz Enery Cycle
MITgcm	Massachusetts Institute of Technology general circulation model
NASA	National Aeronautics and Space Administration
NCAR	National Center for Atmospheric Research
NCODA	Navy Coupled Ocean Data Assimilation
NRMSE	Normalized Root Mean Square Error
OA	Objective Analysis
OI	Optimal Interpolation
OSCOM	Ocean Surface Current Multiscale Observation Mission
P_e	Eddy Potential Energy
PF	Particle Filter
P_m	Mean Potential Energy
SMOS	Soil Moisture and Ocean Salinity
SODA	Simple Ocean Data Assimilation
SQG	Surface Quasigeostrophic
SSH	Sea Surface Height
SSS	Sea Surface Salinity
SST	Sea Surface Temperature
SWOT	Surface Water and Ocean Topography
TAF	Transformation of Algorithms in Fortran
XBT	Expendable Bathythermography
3D	three-dimensional
3DVAR	three-dimensional variational
4DVAR	four-dimensional variational

List of Figures

1.1 Space-time scales of important oceanic processes 1

1.2 Global patterns of submesoscale vertical heat transport 2

1.3 Schematic diagram of the important dynamical regimes by scale 2

1.4 Example of 4DVAR intermittent assimilation in a numerical forecasting system 11

2.1 Initial Temperature and salinity and corresponding potential density and buoyancy frequency profiles in the model spin-up run 17

2.2 Schematic view of the numerical ocean box 17

2.3 Distribution of potential density at the surface after spin-up 18

2.4 Snapshots of normalized relative vorticity, ζ/f, at T = 20 days at the surface 19

2.5 Schematic diagram of the optimization process 21

3.1 Snapshots of lateral strain rate α at T = 20 days at the surface 25

3.2 Frequency and wavenumber spectrum of zonal velocity at the surface 26

3.3 Lorenz Energy Cycle (LEC) for two runs 28

3.4 Variations of layer-integrated k_e 29

3.5 Variations of layer integrated $c(p_e, k_e)$ 30

3.6 The frequency spectrum of $c(p_e, k_e)$ 31

3.7 Snapshots of $c(p_e, k_e)$ within four frequency ranges 32

3.8 The depth-time dependence of the layer-integrated $c(p_e, k_e)$ over four frequency ranges 33

3.9 Layer-integrated profile of $c(p_e, k_e)$ 34

3.10 w' and ρ' within subinertial frequency band 35

3.11 The wavenumber spectrum of $c(p_e, k_e)$ 35

3.12 Variations of layer integrated $c(k_m, k_e)$ 36

3.13 The frequency spectrum of $c(k_m, k_e)$ 37

3.14 The depth-time dependence of the layer-integrated $c(k_m, k_e)$ over four frequency ranges 37

3.15 Layer-integrated profile of $c(k_m, k_e)$ 38

3.16 Layer integrated terms of $c(k_m, k_e)$ indicated in Equation 3.10 among the subinertial frequency range A0 39

3.17 The wavenumber spectrum of $c(k_m, k_e)$ 39

3.18 Snapshots of ζ/f for three components 41

3.19 Average $c(p_e, k_e)$ over cyclonic and anticyclonic eddies (no forcing run) 42

3.20 Average $c(k_m, k_e)$ over cyclonic and anticyclonic eddies (no forcing run) . . . 42

3.21 Average $c(p_e, k_e)$ over cyclonic and anticyclonic eddies (forced run) 43

3.22 Average $c(k_m, k_e)$ over cyclonic and anticyclonic eddies (forced run) 44

4.1 Schematic view of the adjoint model domain 48

4.2 Comparison of the surface initial condition before and after smoothing 49

4.3 Wavenumber spectra of surface zonal velocity with and without smoothing from the initial conditions 50

4.4 Results from a forward run with smoothed velocity and original temperature and salinity as initial conditions 51

4.5 Comparison between prior, posterior and true state of surface ζ/f at time T = 5 days (from Ex-W1) 53

4.6 Comparison between prior, posterior and true state of surface ζ/f at time T = 10 days (from Ex-W2) 54

4.7 Comparison between prior, posterior and true state of surface ζ/f at time T = 15 days (from Ex-W3) 55

4.8 Comparison between prior, posterior and true state of ζ/f at 25 m and at time T = 10 days (from Ex-W2) 56

4.9 The comparison of NRMSE between the prior and posterior states in experiments Ex-W. 56

4.10 Evolution of the normalized cost function as function of iteration number. . . 57

4.11 Comparison between prior, posterior and true state of surface temperature at time T = 10 days (from Ex-W2) 57

4.12 Comparison between prior, posterior and true state of surface salinity at time T = 10 days (from Ex-W2) 58

4.13 A typical distribution of $\Delta\rho$, $term1$ and $term2$ (Equation 4.3) at the surface in our simulation 59

4.14 Differences between posterior and true surface state for all Ex-ADD experiments at T = 5 days 60

4.15 The cost function normalized by the number of observations for Ex-ADD3 . . 61
4.16 SSH observation strategy for selected Ex-DSR experiments 62
4.17 Comparison of surface ζ/f at time T = 10 days in experiments Ex-DSR (no wind) 63
4.18 NRMSE distribution of experiments Ex-DSR (no wind) 64
4.19 NRMSE distribution of experiments Ex-DTR 66
4.20 Example of SSH distribution for different noise levels of experiments Ex-DOE 67
4.21 Comparison of surface ζ/f at time T = 10 days in experiments Ex-DOE . . . 68
4.22 NRMSE distribution of experiments Ex-DOE 69
4.23 Comparison of surface ζ/f at time T = 10 days in experiments Ex-DSR (wind case) 70
4.24 NRMSE distribution of experiments Ex-DSR (wind case) 71

List of Tables

2.1 List of key model parameters 16

3.1 All possibilities regarding different signs of $c(p_e, k_e)$ 30

3.2 Average percentage of occupation and average quantities contained in three components over the upper 50 m (no forcing run) 41

3.3 Average percentage of occupation and average quantities contained in three components over the upper 100 m (forced run) 43

4.1 Experiments exploring the length of the assimilation window 52

4.2 Experiment exploring the impact of multiple assimilated variables 58

4.3 Experiments exploring the density in observational coverage 62

4.4 Experiments exploring the impact of the temporal resolution in the observations 65

4.5 Experiments exploring the impact of random noise added to the observations 66

4.6 Experiments exploring the density in observational coverage (wind case) . . . 69

Acknowledgements

I would like to express my gratitude to my supervisor Prof. Dr. Detlef Stammer, for offering me the opportunity to pursue my PhD degree in oceanography. His continuous support and encouragement motived me to the right way towards the end. I especially thank my co-supervisor, Dr. Nuno Serra, for his professional guidance throughout the PhD process. His kind patience and encouragement are the key to the success of this thesis.

I am extending my thanks to Prof. Dr. Eva-Maria Pfeiffer for being my panel chair and expressing great concern during my difficult time.

The world has fallen into an unprecedented panic and chaos since the beginning of 2020, which suddenly disturbed my PhD plan and caused a pretty tough period for me. Fortunately, Prof. Chuanyu Liu kindly provided me with the workplace in Qingdao as well many helpful discussion during my stuck in China. My staying in Qingdao was also supported by Prof. Weimin Zhang. I am grateful for their warm and self-giving help.

It is a great honour and pleasure for me to join the Remote Sensing and Assimilation Group. I have learned a lot from those outstanding and helpful colleagues. I especially thank my peers, Anju, Aurpita and Franzi. Their company makes my PhD daily life not dull anymore.

I would also thank SICSS graduate school for providing endless courses that contain lots of helpful knowledge and soft skills and plenty of fun. They are necessary parts of my colourful PhD. A special thanks to Dr. Ingo Harms and Dr. Berit Hachfeld, who offers impressive help throughout my PhD.

During the writing of this thesis, I obtained plenty of help from Guokun. We have many instructive discussions, and I am grateful for him. I also thank Franzi for her correctness with the German abstract. I especially thank Nuno for his revision of this thesis, which significantly improved this thesis.

I would like to acknowledges the financial support by China Scholarship Council (CSC). I could not have had this opportunity to study abroad without their support.

Finally, I would like to express my gratitude to my parents, Zhongqiu and Lingxia, to my sister Yao and my brother-in-law Xiahui, and to my dear friends. They have always been the backing force that inspires me to be a better man.

Aus dieser Dissertation hervorgegangene Vorveröffentlichungen

List of Publications

S. Li, N. Serra and D. Stammer (2021): Kinetic energy conversion in a wind-forced submesoscale flow. *To be submitted.*

S. Li, N. Serra, C. Liu, A. Köln, G. Lyu, W. Zhang and D. Stammer (2021): Constraining the submesoscale flow in an eddy-resolving adjoint-based data assimilation model. *To be submitted.*

Eidesstattliche Versicherung
Declaration on Oath

Hiermit erkläre ich an Eides statt, dass ich die vorliegende Dissertationsschrift selbst verfasst und keine anderen als die angegebenen Quellen und Hilfsmittel benutzt habe.

I hereby declare upon oath that I have written the present dissertation independently and have not used further resources and aids than those stated.

Changsha, den 10. August 2021

Song Li